



**UNIVERSITÀ
DEGLI STUDI
DI TRIESTE**

UNIVERSITÀ DEGLI STUDI DI TRieste

XXXIV CICLO DEL DOTTORATO DI RICERCA IN
INGEGNERIA INDUSTRIALE E DELL'INFORMAZIONE

Optimization of the structure-borne noise analysis methods with the
help of virtual sensing with numerical and experimental results
integration

Settore scientifico-disciplinare: ING-IND/13 MECCANICA APPLICATA ALLE
MACCHINE

DOTTORANDO

Ing. Andrea RICCI

COORDINATORE

Prof. Ing. Alberto TESSAROLO

SUPERVISORE DI TESI

Prof. Ing. Luigi BREGANT

CO-SUPERVISORE DI TESI

Dr. Ing. Frank ALBERTZ

ANNO ACCADEMICO 2020/2021

Contents

1	Introduction	1
1.1	Thesis Structure	1
1.2	Motivation and Objectives	3
2	Technical Background	7
2.1	Low Frequency noise	7
2.2	Booming Noise	10
2.3	Rubber Mounts	12
2.3.1	Experimental Characterization	15
2.3.2	Elastic Center	16
2.4	Noise Transfer Functions and TPA	18
2.4.1	Noise Trasfer Functions (NTFs)	19
2.4.2	Transfer Path Analysis	20
2.4.3	Transfer functions variability	24
3	Powertrain Mounts Characterization	26
3.1	Experimental Setup	26
3.2	Powertrain kinematic analysis	32
3.2.1	Derivation of the body acceleration equation	32
3.2.2	Powertrain accelerations	34
3.2.3	Geometric Consistency	35
3.2.4	Virtual Point	37
3.3	Dynamic Force Transfer Procedure	39
3.4	Powertrain Mounts Characterization	41
3.5	Parametric response model generation	46
3.6	SPL synthesis and methodology validation	55
3.6.1	SPL Synthesis	55
3.6.2	Evaluation of the RS methodology	57
3.7	NTF Estimation Errors	60
3.7.1	Vehicle Modal Analysis	62
3.8	Optimization	64
3.8.1	Design of experiments - all vehicles	65
3.8.2	Optimization strategy	66
4	Electric refrigerant compressor for air conditioning system	72
4.1	Rotor unbalance	75
4.1.1	Scroll operational Excitation	75
4.2	Experimental estimation	76
4.3	Derivation of the system's matrices	78
4.3.1	Derivation of the mass matrix	78
4.3.2	Derivation of the stiffness matrix	79

Contents

4.3.3	Apparent Mass matrix	79
4.4	Experimental Derivation of the Apparent Mass	81
4.4.1	Experimental Results	93
4.5	SPL Synthesis	96
4.5.1	Dynamic stiffness - Compressor's mounts	97
4.5.2	Noise Transfer Functions	98
5	Conclusions	102

Nomenclature

Notation

$\{x\}$ Vector

\vec{x} Position vector (3 dimensional vector)

$[M]$ Matrix

$[\]^T; \{ \}^T$ Transposed matrix or vector

$[\]^*; \{ \}^*; ()^*$ Conjugates complexes of a matrix or vector or single element

$[\]^H; \{ \}^H$ Conjugate complex transpose of a matrix or vector (Hermitian transpose)

$[\]^{-1}$ Inverse of a matrix

$[\ \diagdown M \diagup]$ Diagonal matrix

$[\tilde{x}]$ Skew symmetric matrix (tilde matrix) the vector \vec{x}

\ddot{x} second derivative of x with respect to time

\underline{x} Complex number

$\Re(\underline{x})$ Real Component of \underline{x}

$\Im(\underline{x})$ Imaginary component of \underline{x}

\dot{x} First derivative of x with respect to time

$[\ \diagdown M \diagup]$ Diagonal matrix

ω Angular frequency

Other symbols

ICE Internal Combustion Engine

BEV Battery Electrical Vehicle

SPL Sound Pressure Level

A/C Air Conditioning

HVAC Heating, Ventilation and Air Conditioning

FEM Finite Element Model

EnM Engine Mount

GnM Gearbox Mount

TSM Torque Strut Mount

CTSM Central Torque Strut Mount

AC/DC Alternate Current/Direct Current

TMD Tuned Mass Damper

SVQ Sound and Vibration Quality

TPA Transfer Path Analysis

CTPA Component Based Transfer Path Analysis

TMB Trimmed Mass Body

VP Virtual Point

BMW Bayerische Motoren Werke

CAD Computer Aided Design

EC Elastic Center

DEC Dynamic Elastic Center

RS Response Surface

DOE Design of Experiment

WOT Wide Open Throttle

PMS Powertrain Mounting System

List of Tables

1	Noise Ratings characteristics	9
2	Sound Quality Metrics characteristics.	9
3	B38A15M1 powertrain main properties.	27
4	Accelerometers properties.	30
5	Load cell technical data according to [1] .	32
6	R^2 Values for stiffnesses and dynamic forces - EnM	54
7	R^2 Values for stiffnesses and dynamic forces - GeM	55
8	R^2 Values for stiffnesses and dynamic forces - TSM	55
9	FRFs definitions	80
10	Initial values	87
11	Optimized Values	88

Abstract - English

Vibro-acoustic comfort has become an increasingly integral part of vehicle development over the past 20 years. The perception inside the cabin has a high impact on customer satisfaction and expresses the quality of premium vehicles. The phenomenon of interior noise has always been very complex to study. The problem is complicated by the fact that there is a well-known variability in products. This is due both to variability in the assembly line and in the properties of individual components. The goal is for as many vehicles as possible to meet the design requirements.

Among the various categories of noise, low-frequency noise has deserved special attention from development engineers over the years. It is, in fact, particularly annoying, and can also cause loss of attention and drowsiness while driving. In the category of low-frequency noise, booming is one of those phenomena that one surely wants to avoid while developing a vehicle. This phenomenon is used in this work as a target for the analysis.

Almost all components, which directly, or via isolating elements, are mounted to the vehicle chassis, can generate booming under certain circumstances. This is the case, for example, of the powertrain. In conventional vehicles powered by an internal combustion engine, the powertrain is bound to the chassis with a system of elastomeric mounts. The forces generated by the engine, during operation, are transferred through the mounts to the body, and here generate structural noise, which is perceived with discomfort by passengers.

Using isolating elements to decouple components is a very common practice. Yet the dynamic properties of the mounts are hardly known with sufficient accuracy. Therefore there is always the need to make measurements and to check if the used mounts meet the requirements. It is also well known that the characteristics of these components depend on various parameters. The most important of these are static preload, frequency and amplitude of excitation. Hardly all three dependencies are measured and simulated simultaneously. Mounts present, moreover, a marked variability of their characteristics, from which it follows a variability of vehicle's acoustic quality.

In the first part of this thesis, a methodology is presented for the characterization of powertrain mounts, under real operating conditions, which allows to experimentally measure and model the three dependencies described above. Starting from measurements on a dedicated test bench, using response surfaces, and a virtual point transformation methodology, parametric models of the dynamic stiffnesses of the mounts are generated. With these, considering a representative pool of vehicles, a robust optimization of the powertrain mounts is proposed, aiming at reducing the booming noise in a population of vehicles.

However, not only conventional vehicles are affected by this phenomenon. In electric vehicles, the endothermic engine is replaced by a quieter electric motor. In doing so, other components, whose noise was previously masked by the powertrain, become paramount. One such component is the air-conditioning compressor, which has acquired a new function in electric vehicles, that of cooling the battery module during charging. When in full load operation, it can generate low frequency booming noise. In the second part of this thesis, this effect is analyzed, using inverse methodologies, coupled with virtual point transformation techniques. The analysis includes, in this case, the identification of the characteristics of the component, identifying its internal forces and moments acting during operation. An analytical modeling of the component mounted in the vehicle is proposed and validated through experimental measurements. The dynamic stiffnesses of the mounts are modeled through parametric functions, whose parameters are optimized through "in-situ" experimental measurements.

Abstract - Italian

Il comfort vibro-acustico è diventato, nel corso degli ultimi 20 anni, sempre più parte integrante dello sviluppo di veicoli. La percezione all'interno dell'abitacolo, incide altamente sulla soddisfazione dei clienti, ed esprime la qualità dei veicoli premium. Il fenomeno del rumore in abitacolo, è sempre stato molto complesso da studiare. Esso è infatti il risultato di diversi contributi, aventi meccanismi di generazione diversi, che alla fine vengono percepiti tutti assieme. Il problema è complicato dal fatto che esiste una ben nota variabilità nei prodotti. Questa è dovuta sia alla variabilità nella catena di montaggio, che nella proprietà dei singoli componenti. L'obiettivo, è che il maggior numero di veicoli possibile rispetti I requisiti di progetto.

Fra le varie categorie di rumore, quello a bassa frequenza, si è meritato negli anni particolare attenzione da parte degli ingegneri di sviluppo. Questo è, infatti, particolarmente tedioso, e può anche generare cali di attenzioni e sonnolenza durante la guida. Nella categoria dei rumori a bassa frequenza, poi, il booming è uno di quei fenomeni che sicuramente si vogliono evitare mentre si sviluppa un veicolo. Questo fenomeno viene usato in questo lavoro come obiettivo di analisi. Quasi tutti i componenti, che direttamente, o tramite elementi isolanti, sono montati al telaio del veicolo, possono generare, in determinate circostanze, booming. È questo il caso, per esempio, del powertrain. Nei veicoli tradizionali, motorizzati con motore a combustione interna, il powertrain è vincolato al telaio con un sistema di mounts di materiale elastomerico. Le forze generate dal motore, durante il funzionamento, vengono trasferite attraverso i mount alla carrozzeria, e qui generano rumore strutturale, che viene percepito, con fastidio dai passeggeri.

Utilizzare elementi isolanti, per disaccoppiare componenti, è una pratica molto comune. Eppure le proprietà dinamiche dei mount sono difficilmente note con sufficiente accuratezza. Esiste quindi, sempre, l'esigenza di effettuare misure, e di verificare se i mount utilizzati rispecchiano i requisiti prescritti. È cosa ben nota, inoltre, che le caratteristiche di questi componenti presentino dipendenze da diversi parametri. Fra questi le più importanti sono il precarico statico, la frequenza e l'ampiezza dell'eccitazione. Difficilmente tutte e tre le dipendenze vengono misurate e simulate contemporaneamente. Questi elementi, presentano inoltre, una marcata variabilità delle loro caratteristiche, dalla quale consegue una variabilità di qualità acustica nei veicoli.

Nella prima parte di questa tesi, viene presentata una metodologia per la caratterizzazione dei mount del powertrain, in condizioni di reale funzionamento, che permette di misurare sperimentalmente e modellare le tre dipendenze sopra descritte. A partire da misure su un test bench dedicato, utilizzando risposte di superficie, e una metodologia di trasformazione di punto virtuale, vengono generati modelli parametrici delle rigidità dinamiche dei mount. Con questi, considerando un pool

di veicoli rappresentativo, viene proposta una ottimizzazione robusta dei mount del powertrain, che ha come l'obiettivo di ridurre il rumore di booming in una popolazione di veicoli.

Non solo i veicoli tradizionali sono, però, affetti da questo fenomeno. Nei veicoli elettrici, il motore endotermico viene sostituito da un più silenzioso motore elettrico. Così facendo, altre componenti, il cui rumore veniva prima mascherato dal powertrain, diventano di primaria importanza. Una di queste è il compressore del liquido refrigerante del climatizzatore, che ha acquisito, nei veicoli elettrici, una nuova funzione, quella di raffreddare il modulo delle batterie durante la ricarica. Quando è in funzionamento a pieno carico, può generare rumore di booming a bassa frequenza. Nella seconda parte di questa tesi si analizza questo effetto, utilizzando metodologie inverse, accoppiate a tecniche di trasformazione di punto virtuale. L'analisi include, in questo caso, l'identificazione delle caratteristiche del componente, identificandone le forze e momenti interni agenti durante il funzionamento. Viene proposta una modellazione analitica del componente montato nel veicolo, che viene validata attraverso misure sperimentali. Le rigidità dinamiche dei mount sono modellate attraverso funzioni parametriche, i cui parametri vengono ottimizzati attraverso rilevazioni sperimentali in-situ.

1 Introduction

1.1 Thesis Structure

In this thesis we focus on the structure noise perceived inside the passenger compartment in motor vehicles. In particular, we focus on a phenomenon called low frequency booming. For the study of this phenomenon we focus on two specific applications. In the first half of the thesis, booming from the internal combustion engine is studied and analyzed. In the second half, we turn to the booming generated by the air conditioning compressor, used in electric vehicles. The thesis is then structured to initially provide a description of the motives and goals of this work, which can be found in the chapter [Introduction](#).

This is followed by a description of the low frequency acoustic phenomena, and a definition of the methodologies used. In the chapter [Technical Background](#) we start with a general description of the classification of vibro-acoustic phenomena, [Low Frequency noise](#), and then in more detail of the booming phenomenon, found in [Booming Noise](#). This section describes the main players in the phenomenon, which are then described in more detail. We begin by discussing the insulating (mount) components, which are used to mount, both the motor and the compressor. Their properties are described in [Rubber Mounts](#). Since in this thesis, in the proposed methodologies, the transformation of measured quantities into virtual points is used, we go on to describe in [Elastic Center](#), the characteristics of the elastic center of a system. This definition will be useful in subsequent chapters when identifying the properties of the insulating components. We then proceed to describe the techniques used, and move from the insulating components to the noise transfer functions, and the structural noise synthesis techniques. In [Noise Transfer Functions and TPA](#) the noise transfer functions acquisition system is described. We then proceed with a description of Transfer Path Analysis (TPA). In [Transfer Path Analysis](#) the different techniques present in the literature are discussed and we focus on classical TPA and component based TPA, which will be used in the next chapter. In addition, literature-based considerations regarding the variability of noise transfer functions in vehicles are presented.

We then proceed with the description of the methodologies used to study and optimize the low frequency booming arising from the powertrain. In the [Powertrain Mounts Characterization](#) we begin with a description of the problem in more detail. We first proceed with a description of the instrumentation used, and the type of measurements made. In [Powertrain kinematic analysis](#) the kinematic analysis of the powertrain is then described. In this section, the kinematic analysis transformation into virtual points (*virtual point transformation*), discussed in [Virtual Point](#), is also performed, presenting a control criterion for the quality of the measurements. We continue with a description of a methodology for determining internally developed dynamic forces in individual mounts, the transformation procedure is described in

[Dynamic Force Transfer Procedure](#). In [Powertrain Mounts Characterization](#) the powertrain mounts are finally characterized. Here, the methodology used, which involves the use of surface responses, is described to and discussed. A validation of the generated numerical models, based on actual measured data, is also directly provided. The validation then continues with a comparison of simulated and measured SPL, in [SPL synthesis and methodology validation](#). Before moving on to the optimization of the phenomenon, a more detailed analysis, which includes, the study of the contributions of the individual analyzed paths to the SPL is provided. To further identify SPL peaks, a modal analysis of a vehicular is presented in [Vehicle Modal Analysis](#).

Using the methods developed so far, it is possible to optimize the insulating components to reduce SPL in a population of vehicles. This, which is the ultimate goal of the first part, is presented in [Optimization](#). Here the parametric mount models, generated in [Powertrain Mounts Characterization](#), are used to optimize the booming SPL resulting from the powertrain, in a population of vehicles. The optimization results are reported at the end of [Optimization strategy](#). This also concludes the first part of the thesis.

We then move on to the world of electric vehicles, which marks the beginning of the second part of the thesis. Here the coolant compressor of the air conditioning system is considered. It is started by [Electric refrigerant compressor for air conditioning system](#), where the considered system is described. The objectives of this second part differ from the first one. Now the goal is not to characterize the mounts, but to identify the rotational unbalance characteristics of the compressor. In [Rotor unbalance](#), the quantities that want to be obtained are described analytically. To proceed then, in [Experimental Derivation of the Apparent Mass](#), with the experimental determination of the desired characteristics. In this part in fact, different methodologies are used than what has been done so far. Since a component test bench is not available to identify the system, inversion techniques are used. The results of these are presented in [Experimental Derivation of the Apparent Mass](#). The results of the experimental determination of the compressor's rotor imbalance characteristics are collected in [Experimental Results](#). The last part of the compressor analysis aims to analyze the booming resulting from the compressor in operation. This study is reported in [SPL Synthesis](#).

The thesis concludes with a summary of what has been developed, and considerations of possible research directions for future work.

1.2 Motivation and Objectives

Over the past 20 years, customer expectations for vehicle vibroacoustic quality have increased significantly, making it a de facto design parameter to be considered early in the development of a new vehicle, especially in the premium segment [2]. As expectations for ever more comfortable vehicles increased, the automotive world experienced new challenges and saw the introduction of new technologies. Of all of these, the issue of emissions has become increasingly central over the last decade, introducing major technological advances. Reducing the evolution of the automotive world in a few steps, from a mere acoustic comfort point of view. At first, the displacement of internal combustion engines was reduced, but at the same time turbocharging was introduced in order to avoid a drop in performance. Reducing the mass of the propulsion units, but increasing their performance. At the same time, emission countermeasures were introduced such as cylinder shutdown and start/stop (to name but two). Subsequently, hybrid vehicles were introduced, where electric motors and internal combustion engines coexist within the same vehicle in different ratios, depending on the configuration selected. The vehicle can in fact be a plug in, the battery can be recharged to the internal combustion engine or even the gear-box can be electrified providing a boost function to support the traditional engine (petrol or diesel). Finally, we have seen the arrival of all-electric battery-powered vehicles, which, as this thesis is being written, are beginning to be massively produced. Predictions say that in 10 years they will be the dominant technology, but until then they will have to coexist with more established technologies. It is therefore understandable that in this complex framework of rapid change, achieving the desired acoustic quality for all vehicles in a portfolio becomes a challenge. In fact, it is necessary to find solutions that guarantee a level of vibro-acoustic comfort for as many vehicles as possible, otherwise the risk is that of incurring customer dissatisfaction and therefore damage to the company's image.

The acoustic performance of a vehicle depends on several interacting sub-components, as depicted in the figure 1. When a vibro-acoustic problem occurs, it is therefore essential to first identify the mechanisms that cause it and then find the role that the individual subsystems play, taking into account the synergies between the different functionalities of the individual components. Each of these has multiple functions to perform and in some situations these may even be at odds with each other. In addition, at certain points in a vehicle's development some sub-components are no longer modifiable, making it necessary to optimize those that still are in order to achieve the desired quality.

Another aspect of vibro-acoustic problems is the difficulty of predicting (or simulating) them before they occur. In fact, due to the complexity of the systems considered, typical problems are encountered only when the first prototype components or pre-series vehicles are available to perform measurements. As reported by [4] [5] è it is difficult to simulate a problem before it occurs. It is therefore

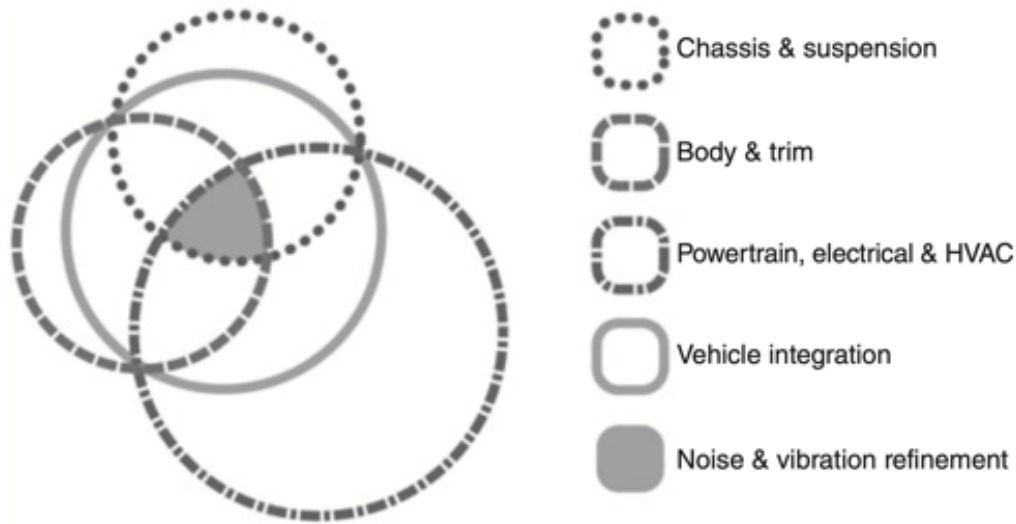


Figure 1: Interaction model of noise and vibration refinement in vehicle integration [copyright RMIT University, 2008, Wang, X. [3]]

predictable to have models (for each level of complexity) that are used for initial dimensioning, and later resort to hybrid models for the refinement phase of individual modules. If a V diagram is taking into consideration, (typical representation of the automotive plans), as the one visible in [2], it is seen like the level of detail of the single component becomes more and more accurate the beginning of the production is approached. From the verification phase of the sub-components only, it is finally possible to carry out the measurements, and verify if the numerical models, previously used to define the project quantities, are good. At this development-level it is possible to make loops to improve performance. Using then hybrid models, where mathematical models are calibrated (or built) with experimental values, it is possible to predict real conditions. The challenge is then to find solutions applicable at this level of development that do not interfere with the requirements defined by the other subsystems. In fact, as described above, each component can have multiple functionalities. At the base of the simulation, there must be a complete understanding of the mechanism that generates or causes the phenomenon under study.

As far as phenomena affecting vehicle acoustics are concerned, low-frequency ones certainly deserve to be included among the most annoying ones. Especially in conventional and hybrid powered vehicles, the powertrain is one of the dominant noise generating components. In this thesis the noise generated by the powertrain itself will be considered in a first step, in a front-wheel drive vehicles with transverse engine arrangement. The main engines could be gasoline, diesel and mild hybrid.

The second part of the thesis focuses instead on fully electric vehicles, namely

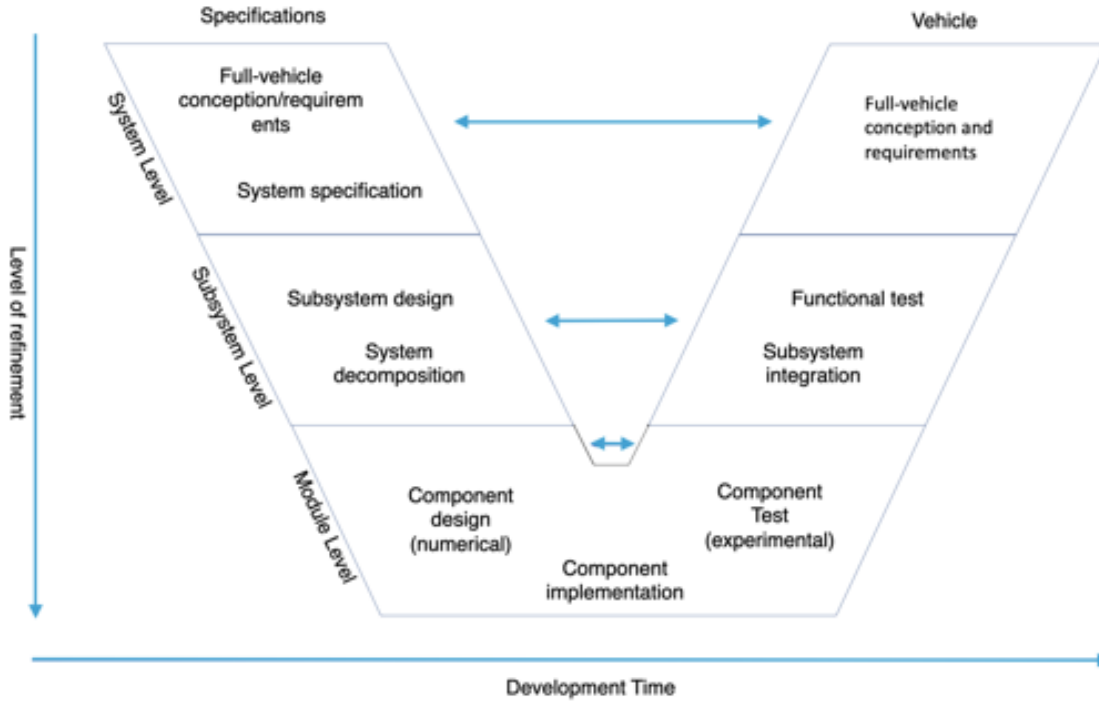


Figure 2: V Model vehicle life cycle - typical approach for the vehicle development

BEVs (Battery Electrical Vehicles). Here, the noise generated by electromechanical components is not masked by the combustion engine. The latter, in fact, while being the major source of noise and vibration in conventional vehicles, had the merit of dominating the overall noise. For this reason, in years past, electromechanical components, even properly designed, were usually not critical to acoustic comfort. Especially the air conditioning system, in BEVs, has increased in importance. [6], [7] Of all the components, the refrigerant compressor is the one that generates the most vibration and noise. This is, in fact, in operation not only when the air conditioning system is running, but also when the car is connected to a fast charging system. The battery module must be cooled for efficiency reasons. The structure and air noise generated by the A/C system during a fast charge is of great discomfort inside the passenger compartment.

The two applications studied above both present structural booming issues. The generation mechanisms are different, and the behavior of the vehicle chassis also has a different influence in the two presented phenomena. For this reason a complete discussion and analysis of the noise generation chain are presented. However, a similarity exists. The powertrain, as well as the compressor of the air conditioning unit, are connected to the chassis through isolating elements. The properties of these elements are particularly difficult to obtain and model.

In this thesis, starting from the two examples, two different methodologies for characterizing the dynamic properties of resilient elements are presented. In the first case, resilient mounts characteristics are directly measured on a dedicated test bench. These represent the main paths contributing to the booming issue. In the second case, missing the dedicated test bench for this characterization, the mounts properties need to be determined in other ways. These involving analytical models and inverse techniques. The research highlighted the strong influence of flexible piping on booming noise generation, which were never considered before.

2 Technical Background

This section first gives an overview of acoustic comfort in the vehicle cabin. The different types of phenomena that can occur are indicated, and a review is provided on the values that are typically used for acoustic analysis of vehicle performance. This is followed by a more in-depth description of booming, as the practical applications of this thesis focus on this phenomenon. Possible mechanisms of generation, and a literature search are presented. In the second part of the chapter, the mathematics that is used for the analysis of the considered systems is discussed.

2.1 Low Frequency noise

Acoustic comfort in a vehicle is complex to assess. Not only are there multiple causes of noise in a vehicle, but also different frequencies of interest. Three are usually identified: low, medium and high frequency. The phenomena that dominate these three areas are different, as is the level of human reception of these phenomena. The aforementioned three bands can be separated as follows:

- low frequency: $15 \div 100$ Hz
- medium frequency: $100 \div 500$ Hz
- high frequency: > 500 Hz

Below 15 Hz we speak only of vibrational phenomena, because the human ear is not capable of perceiving acoustic stimuli at lower frequencies. Above this threshold, we can begin to identify different acoustic phenomena. The category defined as low frequency exhibits a particular characteristic. In this frequency range, in fact, the transaction between the tactile and audible sensation of phenomena occurs, as represented in [3]. This peculiarity makes the study and evaluation of low frequency phenomena particularly insidious. Unlike what happens in other frequency ranges, for the study of the overall vibro-acoustic comfort, both components must be taken into account. A recent study by Festa et al. [8] demonstrated that, fortunately, tactile and audible vehicle vibrations under transient excitations have no significant interactive effects. This means that the two issues can be studied separately. In the course of this work, only the audible component is considered.

The vibro-acoustic phenomena contained within 15 and 100 Hz are therefore of particular interest, especially regarding the customer experience. This range has become even more important as, for reducing pollutant emissions, the engine applications are trying to make the engine operate in this exact range of frequencies. This is described more specifically in the subsection **Booming Noise**.

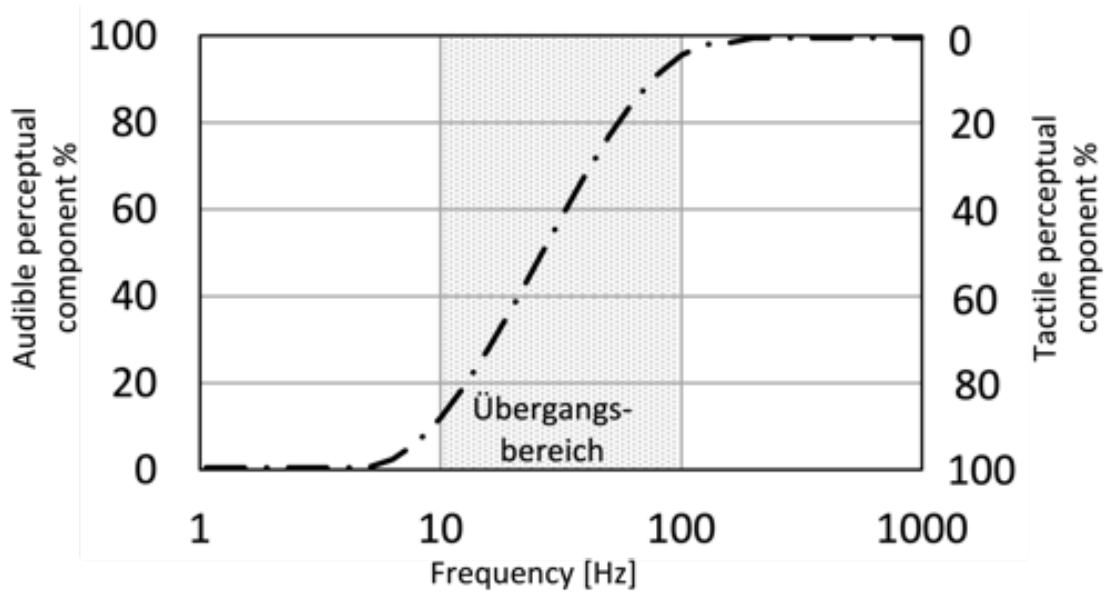


Figure 3: Perception of noise and vibration as function of frequency (figure taken from [9] - description translated into English)

Noise and vibration phenomena are although hardly evaluable in an objective way, it occurs that different subjects reacts differently to the same stimulus. In the work of [10] it is described how the noise discomfort in a vehicle results from not meeting the expectation. Especially when driving at low speed or low engine speed, the sound pressure level within the cabin exceeds what expected from the vehicle passengers. Cerrato [11] defines the complete sound and vibration quality (SVQ) as a matter of customer expectations. Furthermore the acoustic and vibration perceptions cannot be completely isolated from the other perceptions inside a vehicle. Air temperature, light intensity, smells, are all factors which combine together in the final perception when driving.

Always according to Cerrato [11], when dealing with vehicle acoustic, it is fundamental to distinguish between Noise Rating and Sound Quality Metrics. The first ones have been commonly used in the past to define and tackle acoustic problems. As reported in [1] these values are useful to characterize the source of the noise generation, with frequency based analysis. They present although limitation concerning the human perception of different phenomena.

On the other hand many different metrics have been developed and successfully applied to characterize the receiver perception of noises. The sound quality metrics allow for the simulation of the ear perception of noise disturbance, they cannot be although utilized for the characterization of the noise source.

Noise Ratings	
Types	Characteristics
A-Weighted SPL Sound Power Sound Intensity	Characterize the source Frequency based Averaged in time and space Do not account for annoyance caused by tonal components Lack of capabilities for accounting for time variations

Table 1: Noise Ratings characteristics

Sound Quality Metrics	
Type	Characteristics
Loudness Roughness Tonality Fluctuation strength and others	Characterize the Receiver Time and frequency based Simulate how human ear, measures noise All metrics can be computed as functions versus time, accounting for time variances

Table 2: Sound Quality Metrics characteristics.

In this thesis, as value for the study of the noise quality within the cabin the A-Weighted SPL is taken as reference value. The scope of this work is in fact not to evaluate the real human perception but to have a criterion to evaluate the acoustic performance of a subcomponent. Moreover, as previously written even Sound Quality Metrics do not represent the whole picture, but they have to be integrated with jury testing, and customers interviews.

The A-Weight has been used for years. Among the many different acoustic available filters, this one has proven to be the one that mostly reproduce SPL curves which are compatible with what the human ear perceive. For most applications the A-weighting curve gives satisfactory results and the corresponding SPL readings are given in dBA. Other filters, namely B- and C-weightings are sometimes used for high sound levels. D-weighting is primarily used in aircraft noise measurements. The A-Weight $A(f)$, is defined by the following expression as function of the frequency (f):

$$A(f) = \frac{12194^2 \cdot f^4}{(f^2 + 20.59^2)\sqrt{f^2 + 107.6^2}\sqrt{f^2 + 737.8^2}(f^2 + 12194^2)}$$

2.2 Booming Noise

The booming generation mechanisms, in general, is schematically represented as in figure 4. Here the basic interdependency of booming noise are shown. In mounted components there might be moving components. These are for instance pistons, shaft and gears in a powertrain, or a scroll compressor in a refrigerant compressor. These elements generate internal forces and moments which results in components movements. In the low frequency range it is possible to describe the component movements with a rigid body motion. The rubber mounts work then as transferring elements, as through their dynamic stiffness they convey dynamic forces to the chassis or mounting structure. The latter finds their way to the cabin through different different paths, which must be firstly identified.

As previously described many low frequency noise can be found in a vehicle, each with its own generating mechanism. Among all those, a specific one is known by many drivers, called booming, or humming.

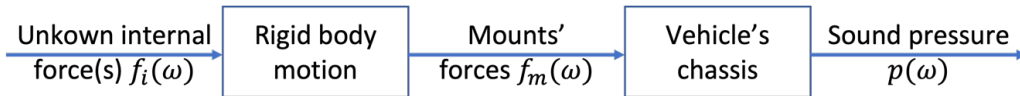


Figure 4: Systematic correlation between internal forces, chassis sensitivity function and sound pressure level within the vehicle

A vehicle can, in practice, be idealized as a closed air volume. The walls of this structure are mainly thin, and coupled to the main block (the cabin) utilizing different joint, rubber elements and or mechanical component. When the windows are not opened the air enclosed, does not have the possibility to escape the geometrical boundaries, except through small openings, usually located in the back of the vehicle to ensure sufficient ventilation. It is therefore possible to talk about a coupled mechanic-acoustical system, the low frequency booming noise falls in this category.

According to Cerrato [12] it is referred to booming when there is a broadband peak in the acoustic characteristic (such as SPL) of a vehicle of the order of 6-7 dB. The author describes also several circumstances under which this phenomenon occurs, typically: idle and acceleration (both stationary and moving). As different studies report, Cerrato [12], S.H. Shin et al. [13], Rengarajan et al. [14], and V.A.J Britto et al. [15], the phenomena have different generating mechanisms. The excitations that generate booming can also be different: from the tires, the intake system, the engine, the body itself, or even installed electromechanical components.

Regardless of the origin of the acting dynamic forces, booming appears when those have a frequency close to a cavity mode of the fluid confined by the cabin. The mechanism of coupling between these excitation and the car's frame can be found in the work of Lee et al. [4].

To solve this low frequency problem, there are essentially three different approaches: modify the source of the dynamic forces by changing its excitation frequency, modify the receiving structure (the body) or somehow reduce the forces' transmission between source and receiver.

To reduce the magnitude or change the excitation force frequency, several solutions can be considered. One can, for example, improve the construction quality of a component by improving its geometrical tolerances. Although the effects of this approach would certainly be appreciable, it is clear how it increases the costs of the final products. Alternatively, one can consider changing the operating regime of the component. A combustion engine, or any other rotating element can be made to run at a different rpm. However, this solution, which would certainly produce positive results, very often collides with other constraints. Combustion engines, in order to reduce CO_2 emissions are often run below $2000[rpm]$, preferably running in the highest available gear. Even under acceleration conditions, the ECU, often prefers not to switch gears, and let the engine gain rpm slowly. This condition of low engine rpm and long accelerations with constant gear is the typical situation where booming noise is generated. The same principle also applies to other electromechanical components, such as hydraulic pumps or compressors. The operating speed is defined so that the component operates at its maximum efficiency. Changing, therefore, the forces at the source is in fact impractical due to cost or efficiency issues, and is therefore rarely pursued. Modifying the source forces is actually impractical due to costs or efficiency issues.

If the modification of the body is preferred, there are basically two options. The first one is of structurally modify the components the second is to add a tuned mass damper (TMD). An example of the first approach is in Britto et al [15], where to reduce a high frequency booming the thickness of a subframe is modified. For the second approach the work of Duan et al. [16], describes this kind of emergency solutions adopted when no other more systematic approach could be implemented. Both approaches show great potential and are regularly applied in vehicle development. However, it must be kept in mind that making structural changes late in the vehicle development process can pose major risks on the timing and cost of the final product. Unfortunately, as described by Lee et al. [4] very often acoustic phenomena are found only when the first vehicles are available for testing. This typically occurs with prototype or pre-series vehicles. Although TMDs can be added later, there are issues related to their placement, which must be in an area sensitive to

booming. Defining such a location in the early design phase is not usually possible since the numerical model used in those moments are not refined enough. Another way to modify the receiver side is to locally modify the body by adding mass in strategic places. Since vehicle frames are typically very stiff, a lot of mass should be added to modify their dynamic behavior. Increasing mass is absolutely contrary to attempts to reduce CO_2 and should therefore not be considered as an optimal method for achieving vibro-acoustic standards. In general, therefore, modifying the receiver component may be a solution, but it is not always applicable with acceptable costs and timing.

The third way is to reduce the transmission of dynamic forces between source and receiver. In many different applications this is achieved by inserting elastomeric (rubber) mounts between the sources and the receiver. This is a widely used practice, not only to decouple the motor from the chassis, but in general all those components that develop excitations during operation, which can be transmitted to the chassis. This is the case with service pumps and electromechanical components (many components of the A/C system are so mounted).

Isolation supports are defined, like all other components, early in the development of a vehicle. Typically, however, the parameters that describe the dynamic behavior (dynamic stiffness and damping) are modeled using initial values, which cannot be verified. These are usually given by the supplier, estimated or based on reference values. However, the initial values are used to perform simulations, through which the positioning and orientation of the insulating elements are defined and fixed. A modification of the mounting design of the individual components is therefore to be avoided. It would fall into the situation described above, i.e. the structural modification of a component, which would most likely affect other functions. The most attractive idea is therefore to optimize the dynamic characteristics of the insulating elements. Unlike other components, even in advanced stages of development, it is possible to modify stiffness and damping of each isolating element, in each of its directions in a range of $\pm 20\%$.

2.3 Rubber Mounts

Although rubber mounts are frequently used to isolate components, not only in the automotive industry, their dynamic modeling remains a challenge today. While static properties can be derived through experimental measurements, the same cannot be said for dynamic ones. The latter are often derived from the first ones by using a dynamic stiffening factor, otherwise supplier-defined data are used or alternatively in-house measurements are performed to characterize the mounts, as reported for example in the works of Yang et al. [17] and Madjlesi et al. [18].

Dynamic properties refer specifically to dynamic stiffness, expressed as real and imaginary components. Other possible representations are amplitude and phase, or defining amplitude and loss factor. All the three representations are valid, and it is possible to pass from one to the other if desired. The more used ones are sure the last two, also for simplicity of understanding. In this text, following internal development standards, the real and imaginary representation is preferred.

Unfortunately, a fundamental aspect of insulating components is their dependence on multiple parameters. In fact, they exhibit, to different and unrelated degrees, dependence on temperature, displacement amplitude, frequency and static preload. More in detail:

- **Temperature Dependency** The variability due to temperature has to do with the variability of the mechanical properties of rubber, which exhibits a marked dependence on temperature. As described in the work of Sjöberg [19] elastomeric materials possess three distinct regions of behavior: glassy, transition and rubber. When the material is in the glassy state then the shear modulus is higher, while the damping is small. When entering the rubber region, the shear modulus decreases in magnitude, while the loss factor increases. Staying in the rubber region, both values show a moderate dependence on temperature.
- **Amplitude dependency** The variation of the vibration amplitude in an insulating element modifies its dynamic behavior. In general, rubber used for mounts presents a dynamic stiffening behavior when the excitation amplitude is small. Vice versa, it presents a softening behavior when the excitation amplitude is large. This behavior has its origin in the way the molecular chains of the elastomer reorganize when stretched. When the displacements are small the structure remains more organized and compact, while for large displacements the structure becomes more flexible. For studies of these nonlinear behaviors we refer to the studies of Harris and Harris and Stevenson [20], [21].
- **Frequency dependency** Elastomeric mounts exhibit a marked frequency dependence. It is generally true that for low excitation frequency the dynamic stiffness is lower, as well as the damping. Increasing the excitation frequency, dynamic stiffness and dynamic damping increase. This behavior, as reported by Sjöberg [19] can be appreciated in all three regions (glassy, transition and rubber), with different characteristics. The phenomenon is clearly made more complex by the concomitant dependence on temperature. However, when this is kept constant (room temperature for example) it is then possible to isolate the frequency dependence, and evaluate it accurately.
- **Static preload dependency** Static preload dependence is probably the most difficult to measure and about which there is also less literature. Usually,

measurement systems only allow preloading of a mount in the direction of excitation. A multiaxial preload is more difficult to achieve. In Kari's study [22], the dependence of an insulating element is investigated up to 500 Hz. The results show that with increasing frequency the dependence becomes more important. An approach to investigate the multi-axial preload dependence is found in the work of Lectez et al. [23].

These dependencies manifest in stiffness and damping (or loss factor) in different ways. In the work of Sjöberg and Kari [24] an increase in the loss angle is shown with increasing frequency. However, the loss angle can also remain constant with respect to the frequency increase. In the work of Alonso et al. [25], it is shown, for example, that the loss angle peaks at an intermediate amplitude, especially for when the higher hardness values of a rubber constraint are tested.

These features are not usually incorporated into the initial models used for initial sizing, examples are given in the work of Horiuchi et al. [26] or in Bruns and Dryer's study [27] in which a hydraulic support is modeled in detail. Only in recent work have attempts been made to use values derived from measurements as representative as possible of the actual operating conditions of the supports in numerical models, for example in Ueda et al. [28] where the modeling of a wishbone support is presented. This allows the application of multi-axial excitations and near vehicle conditions. In the work of Si Li et al. [29] data from the vehicle are used to train a mount model, further tested on a component test bench.

Where data are not experimental, the use of standard elements is employed. The most common method is to use a Kelvin-Voigt element, or a series of combinations of such elements coupled together in series or parallel. These approaches are also used in other industries, such as railroads, where mounts must be characterized at lower frequencies. In the rubber model described in this paper, it is seen that only the element described by Berg [30] [31] exhibits realistic dynamic stiffness and loss factor behavior simultaneously.

For a more detailed review of the limitations of different modeling approaches, refer to the work of Feng et al. [32] where a review of mount modeling approaches such as multi-body or FEM (distributed or concentrated mass) is given.

Apart from the considerations on the acoustic insulation provided by the mounts, and on their properties in the vibro-acoustic field, it is necessary to make a further clarification. These mounts in fact have multiple functions, among which ensure safety in accident conditions but also last enough during different driving conditions. A full report about the functionalities rubber mounts must withstand can be found in the works of Shangguan [33] and Yu et al. [34]. For these reasons, the dynamic stiffness values and their dimensions cannot be changed at will, due to material, design and space limitations.

2.3.1 Experimental Characterization

The dynamic stiffness and damping characteristics of rubber mounts are most often determined from experimental measurements. These data are then used in numerical models to simulate the dynamic behavior of the individual sub-components in the complete vehicle. In order to generate the most accurate results possible, the characterization of the mounts must be reliable.

Several methodologies for the dynamic characterization of mounts have been developed over the years. The most traditional, involves the use of tensile testing machines modified to be able to apply a dynamic force. Examples can be found in [35], [36]. The limitation of this approach, is that a static preload can be applied only in the direction of excitation. Additionally, there are problems due to potential resonances of the complete system when the dynamic properties are to be obtained at higher frequencies (e.g. above 500 Hz). The entire test bench must be free of resonances for the complete range of interest. In any case, these test benches allow the dynamic stiffness to be measured directly from the test bench. These are in fact, with few exceptions, instrumented with load cells that measure blocked forces.

Other methodologies have been developed more recently and can be found in the work of Wagner et al. [37] and Häussler et al. [38]. Here, the developed methodology, as opposed to classical methodologies, allows the dynamic stiffness of the mounts to be obtained through free-free measurements. Through the use of "cross" shaped elements placed at the two sides of the rubber mount, it is possible to excite all degrees of freedom (6 DoF). The results shown in the two papers are extremely promising when combined with CTPA. However, the limitation of measuring free-free components is that no static preload can be applied. A further limitation in the work of [38] is given by the measurement through hammer excitations. In this way it is not even possible to control the level of the excitation amplitude. This limitation is however overcome in the work of [37], where the use of inertial shakers is provided. Wagner again [37] describes the procedure for obtaining the dynamic stiffness. The measured frequency response function matrix must be inverted and twice integrated to obtain the dynamic stiffnesses from the inertance. Matrix inversion has well-known problems, where one often has to work with ill-conditioned matrices and noise in the measurements.

Another problem with mounts is their variability. It is clear that, like any mechanical component, mounts exhibit certain tolerances. Both from a geometrical and a performance point of view. Leaving aside the mechanical tolerances, which could have an importance on the local behavior of fixing to the chassis, we focus more on those of the elastomeric element. In the work of Peng et al. [39] and Kinchen et al. [40] this is described in a $\pm 15\%$ deviation from the nominal value. This can clearly have a huge impact on the acoustic quality of different vehicles.

2.3.2 Elastic Center

As mentioned in the previous paragraph [2.3.1](#), in the inversion of matrices, one often runs into ill-conditioning problems. To solve these, the solution can be sought in diagonalisation. Focusing only on the stiffness matrix of a system, the question arises, therefore, whether there is a condition or transformation for which this matrix of a component or system becomes diagonal. The answer to this question, finds an answer in static mechanics, where a point called the elastic center can be defined. The definition of this point has been of interest in robotics studies a few years ago. A first indication is found in the work of Whitney et al. where it is referred to *Center of Conformities* [\[41\]](#). In another robotics study, by Joo et al. [\[42\]](#) a similar definition is given, and a *Center of Compliance* as a remote point is defined. This concept is widely used in micromechanics, especially in component mating operations, which can sometimes prove to be very costly. Performing them at the so-called *Center of Conformity* point the system, can correct any misalignments more easily. When a linear misalignment occurs then a reaction force is sufficient to correct the positioning of components. When angular misalignment occurs, a moment of contact is sufficient to realign the system.

In the work of Ciblak et al. [\[43\]](#) the definition of "elastic center" is finally proposed. In fact, an analogy is made between elastic center derived from beam theory, and the center of compliance.

Resuming his discussion, and starting with beam theory, as depicted in figure [5](#)

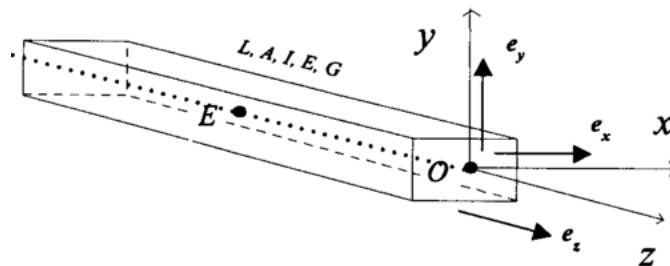


Figure 5: Representation of a generic beam with its coordinate system. Point E identifies the elastic center from [\[43\]](#).

The stiffness matrix of a 3D beam in space is usually defined using a 12x12 matrix, which can however be reduced to 6x6 if either end of the beam is rigidly constrained. Considering for simplicity a linear case, with small displacements, the stiffness matrix can be derived simply by Hook's theorem. A generic load vector can be applied at point O, such that $\{F_o\} = \{f \ m_o\}^T$, where f is a force vector and m_o is a vector of applied moments, and $\{\delta_o\} = \{x_{o,s} \ \theta_{o,s}\}^T$ is a small linear displacement, where $x_{o,s}$ is a small linear displacement and $\theta_{o,s}$ is a small rotation. The force displacement relation can simply be defined as:

$$\{F_O\} = [K_O]\{\delta_O\} \quad (1)$$

Where the stiffness matrix can be written as:

$$[K_O] = \begin{bmatrix} k_{xx} & k_{x\theta} \\ k_{\theta x}^T & k_{\theta\theta} \end{bmatrix} \quad (2)$$

In the matrix $[K_O]$ the quantities are dependent on the origin. The terms are derivable in this specific case from the beam theory. Here then, using rigid body transformation, a point can be found, at which the stiffness matrix becomes diagonal. By naming this point E , as in the figure [5](#) there exists a geometric transformation, which allows this operation.

Therefore, an operation can be defined:

$$\chi_{OE} = \begin{bmatrix} 1 & \overrightarrow{OE}_X \\ 0 & 1 \end{bmatrix} \quad (3)$$

which allows to write the force-displacement relation for the point E as:

$$\{F_E\} = [K_E]\{\delta_E\} \quad (4)$$

con:

$$\begin{aligned} \{\delta_E\} &= [\chi_{OE}]^{-1}\{\delta_O\}, \quad \{F_E\} = [\chi_{OE}]\{F_O\} \\ [K_E] &= [\chi_{OE}]^{-1}[K_O][\chi_{OE}]\{\delta_O\} \end{aligned} \quad (5)$$

The stiffness matrix is thus completely diagonalized. In the three papers above, it is shown how such a center exists for beam systems (in this case) elements composed of elastomeric material rings and metal disks. Finally, as shown by Ciblak et al. [\[43\]](#), the considered beam, in the elastic center, reacts with a translation when subjected to a force, and with a rotation when subjected to a moment.

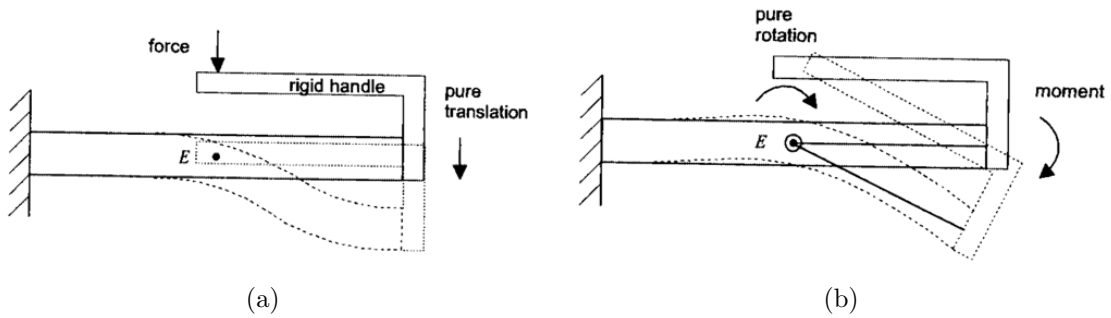


Figure 6: Loads applied in the elastic center E [43]:

- a - An applied linear force produces a pure displacement.
- b - an applied moment produces a pure rotation.

What just described can be extended directly to dynamic systems, provided that the displacements and rotations remain small over frequency. In fact, one can define an elastic center of a resilient component, and also of a component mounted using resilient mounts. The main advantage is that the dynamic stiffness matrix of supports, or of a system mounted with n supports, can be considered diagonal in this point.

As with the stiffness matrix, this circumstance occurs at a specific point in the elastomeric component, called Dynamic Elastic Center DEC.

2.4 Noise Transfer Functions and TPA

As previously mentioned, for the simulation/synthesis of cabin noise, it is necessary to know the behavior of the passive component, in this case how the vehicle behaves from the individual attachment points of each component to the driver's ear. In fact the locally generated noise, crosses several paths before reaching the receiver, as shown schematically in figure 7. These paths are called transmission or transfer paths.

The analysis that allows to identify, and put in order of importance these paths is called Transfer Path Analysis TPA. This technique aims to reveal and quantitatively describe the flow of vibro-acoustic energy from one, or more, sources to the receiver.

The transfer function can be defined through what are commonly called *mechano-acoustic transfer functions* or simply *Noise Transfer Functions*. Through these it is possible to define the correlation between applied excitation and system response, without necessarily having to know the dynamic behavior of the system in detail. Transfer functions can be obtained either experimentally or through FEM models. Although the latter are increasingly being used, and strides are being made, there still remains a non-negligible uncertainty in the models. In particular, doors, trunk doors, and other components that exhibit backlash or contact are difficult to

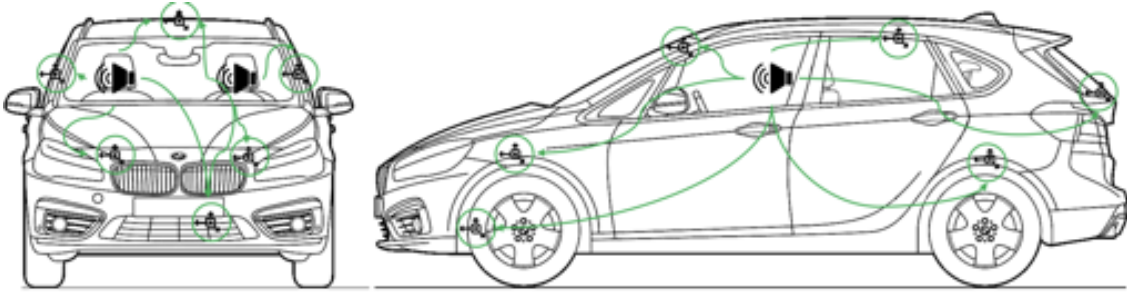


Figure 7: Schematic representation of the structure borne noise paths - Reciprocity measurements

simulate and continue to be a challenge for numerical simulation. In this thesis, mechano-acoustic transfer functions derived from experimental measurements are used.

2.4.1 Noise Transfer Functions (NTFs)

To obtain the transfer functions, several excitation signals, each with different characteristics, can be used in general:

- Sinusoidal signal with fixed frequency ω
- Broadband noise
- Dirac impulse $\delta(t)$
- Step function $\sigma(t)$
- Operating signals

In the automotive field, Dirac impulses (hammer impact), or broadband noise (typically white noise), are usually used. Also for this work, the data used were obtained as follows. For linear and time invariant systems, the ratio of excitations $x(\omega)$ to responses $y(\omega)$ can be written, in the frequency domain, as:

$$Y_{ij}(\omega) = \frac{y_j(\omega)}{x_i(\omega)} \quad (6)$$

The matrix Y_{ij} is referred as FRF matrix, and collects all the frequency response functions, between excitations and responses. In addition to the direct methods for characterizing mechanical acoustic transfer functions, the so-called reciprocal method can also be used. In the direct method, excitations are applied to the

body and the internal sound pressure in the passenger compartment is measured by microphones placed on the head rest of each seat. With the reciprocal method instead, the complete structure is excited by a loud-speaker positioned on the seat. Typically, the two front seats (driver and passenger) are used as excitation positions. This methodology has the following advantages, as described by Wolde [?]:

- It is easier to place a receiver than a source at many points on the chassis.
- It is usually difficult to excite a point in all desired directions, while it is easier to measure the desired degrees of freedom
- Mechanical or acoustical quantities can, sometimes, be replaced by the measurement of electrical quantities, which is more accurate.

2.4.2 Transfer Path Analysis

When dealing with vibro-acoustic issues, a methodology widely used in the industrial world with great success, is used. The TPA methodology is a well know tool, and many examples of practical applications can be found in literature [44], [45], [46], [13], [47].

Under the name of TPA, several methodologies can be identified. These, while having the same basic principle, differ in applicability.

For a very comprehensive report on this topic, refer to the work of Van der Seijs et al [48]. This work is taken up in the next few lines, albeit in less detail, to provide the reader with an insight into the tools used to synthesize the SPL.

The general problem of TPA can be expressed graphically as visible in figure 8.

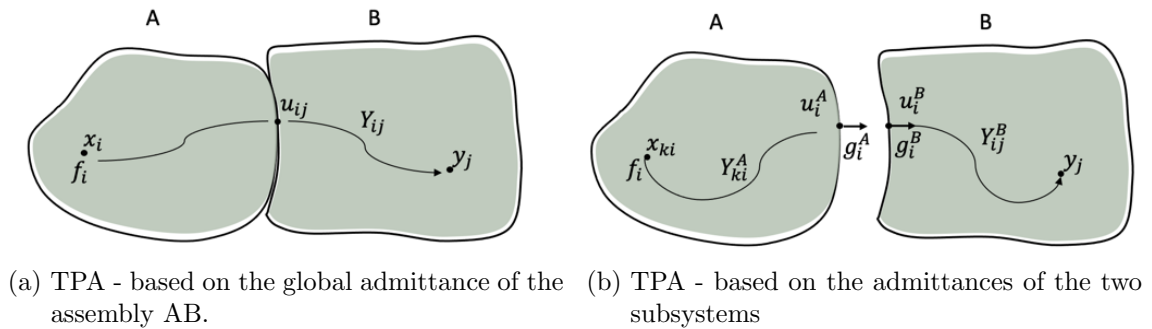


Figure 8: Generalization of the TPA approach

It can in general be written:

$$y_j(\omega) = \sum_i Y_{ij}(\omega) \cdot f_i \quad (7)$$

where:

- y_i represents the DoF at the receiver side, otherwise called receiver. This could be an acceleration, velocity or an acoustic pressure.
- Y_{ij} represents the complete transfer function from source and receiver, going through the connection u_{ij} connection point placed on the interface between the two component.
- f_i represents the internal force generated at the x_i the DoF in the source. This is causing an excitation that cannot be in practice measured.

In his paper, van der Seijs [48], shows how the equivalence between the two systems represented in figure 8, which is expressed by:

$$y_j(\omega) = Y_{ij}(\omega) \cdot f_i = Y_{ij}^B(\omega) \cdot g_i^B \quad (8)$$

For the determination of the transfer functions what was previously written in 2.4.1 applies, for determining the term g_i^B of the equation 8 instead there are several possibilities. A distinction between the different types of TPA can be found in the literature. These are classifiable, also according to [48], into the following categories:

- Classic - TPA
- Component Based - TPA (CTPA)
- Transmissibility based TPA

In terms of the applications of this work we focus on the first two.

Classic-TPA is usually used to identify the contribution of individual paths in an existing product. For this reason it has found its success especially in the troubleshooting phase, i.e. when vibro-acoustic problems arise unexpectedly at a late stage of product development.

The concept behind this methodology is the identification of the dynamic forces that are transferred between active and passive components. There are several approaches to obtain these quantities. For example, one could consider introducing load cells to directly measure the forces g_i^B between source and receiver components. However, this practice affects the dynamic stiffness of the receiver side, thus affecting the result. Another method is to have insulating mounts sandwiched between the source and receiver side, but it is necessary to know in advance the dynamic properties of the mounts used, which as explained in the section 2.3 are usually not known accurately. The last approach, and perhaps the most commonly used, involves measuring the accelerations on the source and receiver sides of the structure.

Thus using the isolation provided by each mount. The dynamic acting forces are then obtained from an inversion of the matrix given by the difference of the two measured accelerations. There are also often issues due to ill-conditioning of the matrix that must be inverted, as explained in the work of Zhang et al. [49].

Indifferently from the methodology used to determine the dynamical forces transferred, the Classical-TPA has a limitation. The source component is identified in the situation in which it is measured. Therefore, it is not possible to transfer the identification to other receivers. This obviously does not pose a problem when working on a single component, however, it can become problematic when trying to optimize multiple vehicles.

Component based - TPA - then comes into play. This has the virtue of characterizing the source so that it can be combined with other receivers. Also in this there are different approaches to determine the forces. For example, one can define "in situ" blocked forces, as proposed by Lennström et al. [50], or in the research activity carried by Moorhouse et al. [51], [52], or in the research of Sturm et al. [53].

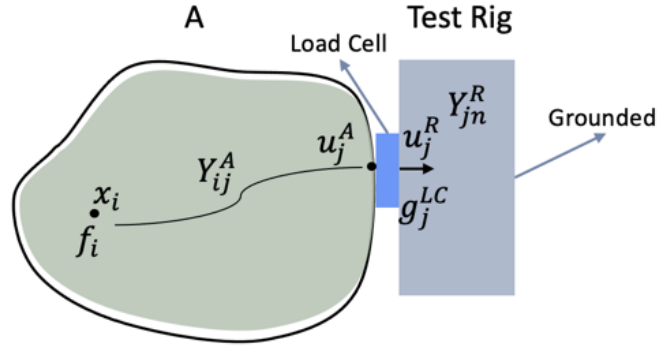


Figure 9: TPA scheme for measuring the Blocked forces on a purpose test bench

Of particular interest is the case where the blocked forces are measured using a dedicated test bench. In case this test bench is rigid enough, the dynamic forces of the active component can be directly measured, using load cells placed between the source component and the test bench.

$$\begin{bmatrix} x_1^A \\ u_j^A \\ u_j^R \end{bmatrix} = \begin{bmatrix} Y_{ii}^A & Y_{ij}^A & 0 \\ Y_{ji}^A & Y_{jj}^A & 0 \\ 0 & 0 & Y_{jn}^R \end{bmatrix} \cdot \begin{bmatrix} f_i \\ g_j^A \\ g_j^{LC} \end{bmatrix} \quad (9)$$

With:

$$\begin{cases} u_j^A = u_j^R \\ g_j^A = -g_j^{LC} \end{cases} \quad (10)$$

Inserting these two in the equation [11](#) the solution for the equivalent force, which describes the active component is given:

$$f_j^{eq} = g_j^{LC} + (Y_{jj}^A)^{-1} \cdot u_j \quad (11)$$

This solution is valid when the utilized test rig is stiff enough. This condition is usually not hard to reach when dealing with low frequency phenomena. An example of a newly developed methodology for the characterization of coolant refrigerant compressor can be found in the work of Gras et al. [54](#). In this work the complete description of the blocked-force test bench is given.

In case the test bench is flexible, the possibility exists to correct the contribution from the test bench itself. An extensive discussion on this topic can be found in the work of de Klerk et al. [55](#).

The transfer path methodology as described can be used to synthesis the SPL within the vehicle, as contribution of the different structure and air borne paths. The SPL synthesis can be performed as it follows:

$$SPL_d(\omega) = \sum_j Y_{dj}(\omega) \cdot f_j + \sum_k Y_{dk}(\omega) \cdot q_k \quad (12)$$

where:

- SPL_d is the resulting sound pressure level at the driver's ear
- Y_{dj} represents the generic impedance matrix of structure borne transfer functions between a j^{th} position at the subframe and the driver's ear
- f_j are the forces transmitted from the active component to the passive component along the j^{th} path
- Y_{dk} represent the generic matrix of air borne transfer functions between the active component at k^{th} position and the driver's ear
- q_k are the acoustic loads transmitted from the active component to the receiver.

As already described in [2.4.1](#), low frequency interior cabin noise is largely dominated by structure-borne noise. Cloix, H. Siwiak et al. [56](#) show in their work that

contribution represents in fact 90 – 95% of the total. With this simplification, the air-borne term can be neglected without loss of generality and equation [12](#) can be reduced to:

$$SPL_d(\omega) = \sum_j Y_{dj}(\omega) \cdot f_j \quad (13)$$

2.4.3 Transfer functions variability

As previously mentioned, the determination of transfer functions is usually carried out by means of measurements. The main reason for this is that the numerical models adopted (FEM) are not able to reproduce the complex system of mechanical clearances, contacts and frictions that exist between the different components of a vehicle. For this reason it is not possible to reproduce any variability due to assembly.

Noise transfer functions are therefore usually obtained through measurement campaigns, as previously mentioned. Also in this case there is a variability. When noise transfer functions are acquired, several strategies can be adopted. For example, one can decide to use a complete vehicle, what is called Trimmed-mass-body TMB. The latter is a vehicle from which the complete driveline is completely removed. This practice is the one that is usually used. The question is then whether the variability in question is already visible in the TMB or whether it manifests itself differently when the complete vehicle is considered. Cloix et al. [56](#) show that variations in the measurements are already present in TMB, and that in complete vehicles it remains essentially unchanged. They also estimate the variability in a value between 10 and 20 dB SPL, in the frequency range between 20 and 80 Hz.

During this work, data from several vehicles, which are nominally identical, are used. The results from Cloix [56](#) results are confirmed by the collected data. As can be seen in the figure, the SPL of 5 nominally identical vehicles shows deviations of 10-15 dB. Another study by Shaver et al. [57](#), studies the variability of SPL during an WOT in 5 different vehicles, identifying the 6dB variability, but considering the frequency spectrum between 2500 and 5600 [rpm], thus higher frequency. The variability of the individual contributions are also identified in this study.

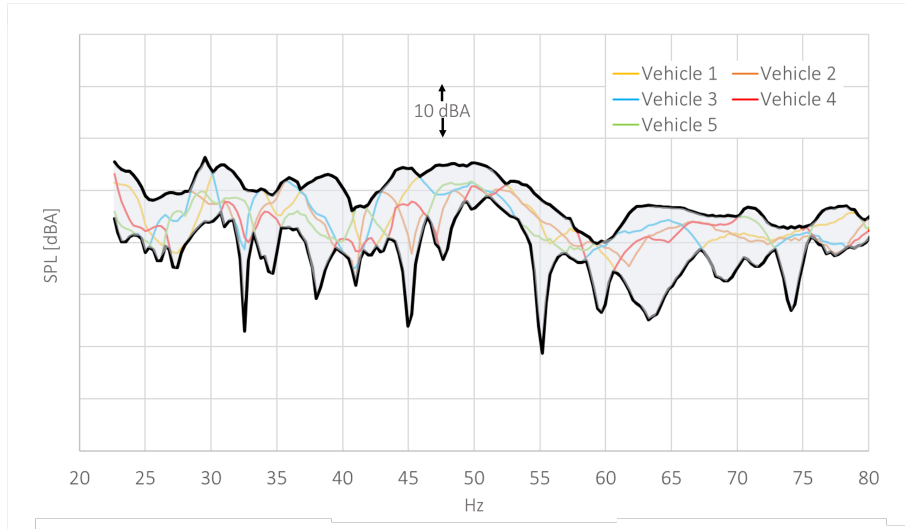


Figure 10: Vehicle SPL variability within a group of 5 nominally identical vehicles

Another key issue when considering the variability of the SPL is to identify its type. Lionnet et al. [58] addresses this issue. In his work, a clear distinction between inter- and intra-variability is proposed. The two, combined define what is called global variability in a population of vehicles. Intra-variability is that which depends on the conditions of use. These are understood as environmental conditions, such as temperature or road wear. Inter-variability, on the other hand, refers to variability due to manufacturing processes, this is in fact defined for vehicles tested under identical conditions. Inter-variability is referred to in this thesis because the vehicles are all tested under the same operating conditions. The temperature dependence is also not modeled, neither for the mounts, nor for the body.

3 Powertrain Mounts Characterization

In this chapter, a methodology developed for the characterization of powertrain mounts is described. This new approach makes it possible to determine the dynamic characteristics of the mounts under operating conditions, while observing their dependence on frequency, amplitude and static preload. At the beginning of the chapter the test bench used to perform the measurements is described. Thanks to its design, it is possible to use the component-TPA, as previously described, for the synthesis of the SPL. Load cells for the acquisition of dynamic forces, transmitted between the active component and the test bench, are in fact strategically placed. For the derivation of the dynamic properties, the virtual point theory VP is used, which is explained later in the paragraph [3.2.4](#). In fact, the goal is the determination of the dynamic properties in the dynamic elastic center (DEC) of each isolating element, which coincides, when existing, with an internal point of each mount. Since it is not possible to experimentally measure any quantity internally in a mount, dynamic stiffnesses must be synthesized in these virtual points through geometric transformations. For this purpose, the calculation of the displacements and dynamic forces in the acVP is performed.

Using the values of the obtained dynamic stiffnesses, parametric numerical models of them are generated. These are based on surface responses, and are validated with further measurements on the test bench. The developed numerical models allow the characterization of each mount to be used independently. It is then shown, how starting from measurements on the test bench, the generated source/mounts models can be combined with other receivers using the Component-TPA for the SPL synthesis.

A schematic representation of the process developed in this section is shown in [Figure 11](#). Here it is also shown how, in a second step, the numerical models developed, will be used for the reduction of SPL in a population of vehicles.

3.1 Experimental Setup

As previously mentioned, the rig was designed to have no flexible modes in the frequency range of interest. For this purpose lateral stiffeners have been added in the past years. This modification resulted in the first flexible mode occurring at $248Hz$, thus being at a frequency about 2.5 times higher than the maximum frequency of interest. This ensures that the dynamic behavior of the mount does not alter the dynamic forces measured at the interfaces between powertrain and test bench.

The structure allows the housing of engines which are used in the compact class of vehicles produced by BMW. These are transversely mounted engines that power

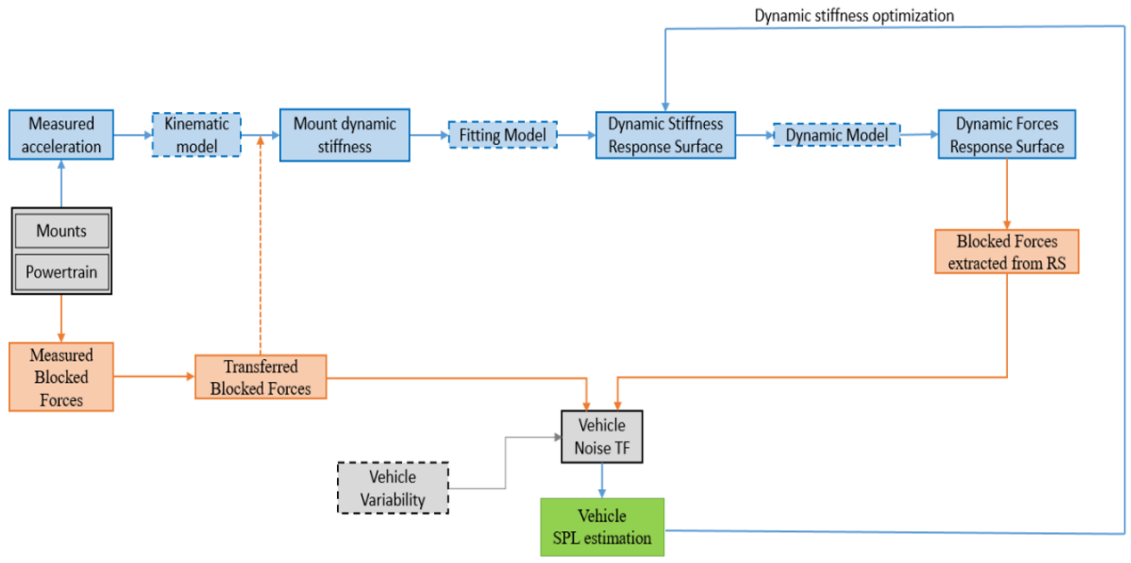


Figure 11: Graphical representation of the procedure followed for the characterization of the powertrain mounts and optimization of the SPL

front-wheel drive (or when desired, four-wheel drive) vehicles. Typical engines are gasoline and diesel, 3- and 4-cylinder, but lately also mild-hybrid engines. The latter feature an electrified transmission, which provides a boost function under certain driving conditions. All engines in this category share the same mount geometry. This fact represents a great advantage of the test bench used. The powertrain is, in fact, housed with its own elastic mounts. In the course of this thesis, mainly one engine was used for the experimental measurements. The engine in question is the B38A15M1, which main characteristics are collected in table 3.

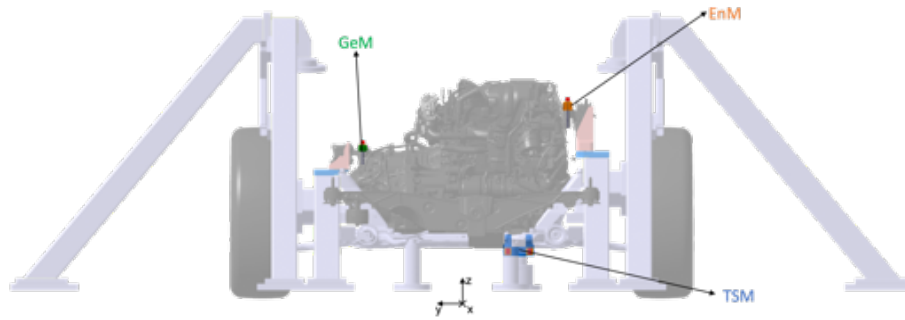
BMW B38A15M1	
Displacement	1499 cc
Cylinder	3-Inline
Valves	12,4 P/Cylinder
Aspiration	Turbo
Fuel	Petrol
Power	140 Ps
Torque	220 Nm
Mass	193.5 kg

Table 3: B38A15M1 powertrain main properties.

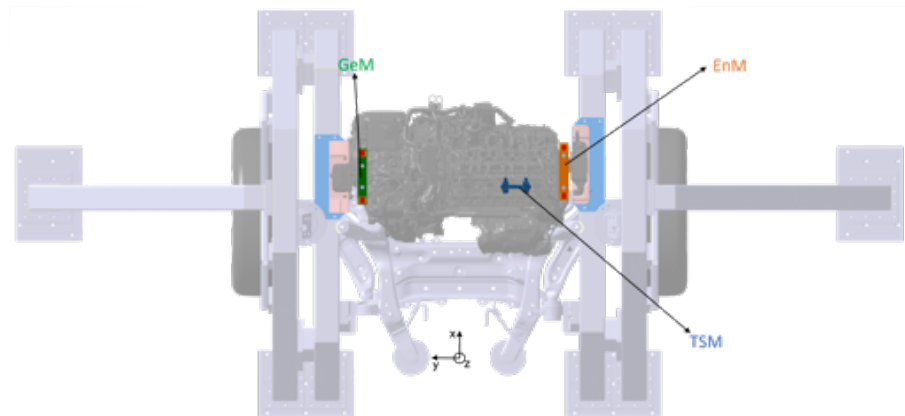
It should be noted that the methods described in this section can only be used for the architecture specified above. However, through limited modifications, it is possible to transfer this type of analysis also to longitudinally mounted engines.

The following three figures show a representation of the used test bench [\[12\]](#). In this assembly the engine is also visible, as well as the complete transmission system. In fact, the test bench uses rolls to operate the drive wheels at the start of measurement. The operation of the complete engine with its drive train, allows therefore to replicate the forces really developed by the reaction of the powertrain. The three figures show the accelerometers positioned on the active component. These are positioned using specific supports. For the identification of the powertrain dynamics three positions are used: Engine Mount (EnM), Gearbox Mount (GeM) and Torque Strut Mount (TSM), all named according to their positioning. The mounts allow three-dimensional accelerometers to be placed in close proximity to each of the three powertrain mounts.

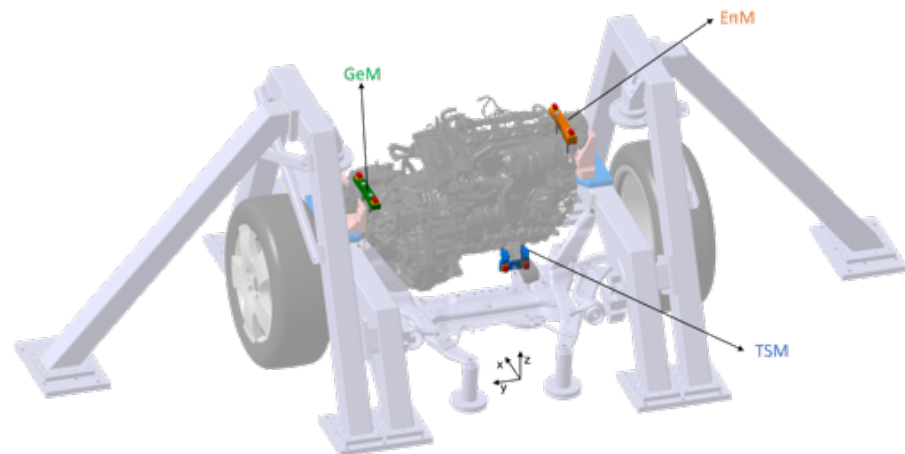
3 POWERTRAIN MOUNTS CHARACTERIZATION



(a) Test bench - Front view.



(b) Test bench - Upper view



(c) Test bench - ISO view.

Figure 12: Test bench representation. The engine is shown as mounted with the front axle carrier. The accelerometers for the identification of the powertrain displacements are placed using specific holders. These last ones are highlighted in different colors: EnM (Engine Mount) - GeM (Gearbox Mount) - TSM (Torque Strut Mount).

Each measurement campaign carried out, consists in the acquisition of data in different engine operating conditions. Two types of measurements are performed for mount characterization. The first called Wide-Open-Throttle (WOT) consists of a ramp from turn-to-empty condition of the motor, up to 3330 rpm. The duration of the ramp is 90 sec. during which the engine delivers the entire available torque spectrum, from 0 to maximum torque. This is done for all available gears. Additional load conditions are then entered, in which the motor torque is limited to fractions of the maximum torque available.

Another type of measurement is called *Load-Slices*. In these measurements the delivered torque is kept constant while the motor operation is made to vary between idle speed and 3300 rpm. In this way, an attempt is made to limit the dependence of the mounts on preload while identifying their dependence on frequency and amplitude.

Data acquisition is performed using an MKII system from Müller-BBM, and the data are also here preprocessed. Since in fact we are only interested in excitations related to the first order of combustion, an order analysis is performed, utilizing internal company standards. This is done for all measured quantities, i.e. accelerations and forces. Using a thaco signal as reference for the analysis, the data are sampled at $16384Hz$, and processed with a resolution of $0.125Hz$.

Also wishbone mounts are identified, which are also used for SPL synthesis, but only in the x-direction. The justification for this practice, lies in the mechanism of force transmission from the wishbone mounts to the chassis. This is treated extensively in Tian's master thesis [59], for further clarification please refer to this work.

The accelerometers used for acceleration acquisition are manufactured by *Brüel&Kjaers*, their main characteristics are reported in table 4.

	Type-4321	Typr-4326
Axis	3	3
Mass [g]	55	13
Frequency range [Hz]	0.1 - 12000	0.1 - 12000
Maximal sensitivity [%]	X:1.0	<5
	Y:1.2	
	Z:0.4	
Sensitivity [$\frac{pC}{g}$]	$9.81 \pm 2\%$	$3 \pm 15\%$

Table 4: Accelerometers properties.

The receiver side of the test bench, is instrumented with triaxial load cells positioned as visible in [13], for the acquisition of the blocked forces. The peculiarity of

this mounting scheme is that two different positions can be measured TSM. There are in fact two versions. In one, the TSM is positioned laterally, closer to the EnM. In a second version, which has been adopted for the new models, it is positioned more centrally. This solution is called CTSM. For the three transmission mounts, multiple load cells are used in the same position. This is done to control and correct any rotational effects of the individual supports. For the other positions, i.e., the wishbone supports, single load cells are used.

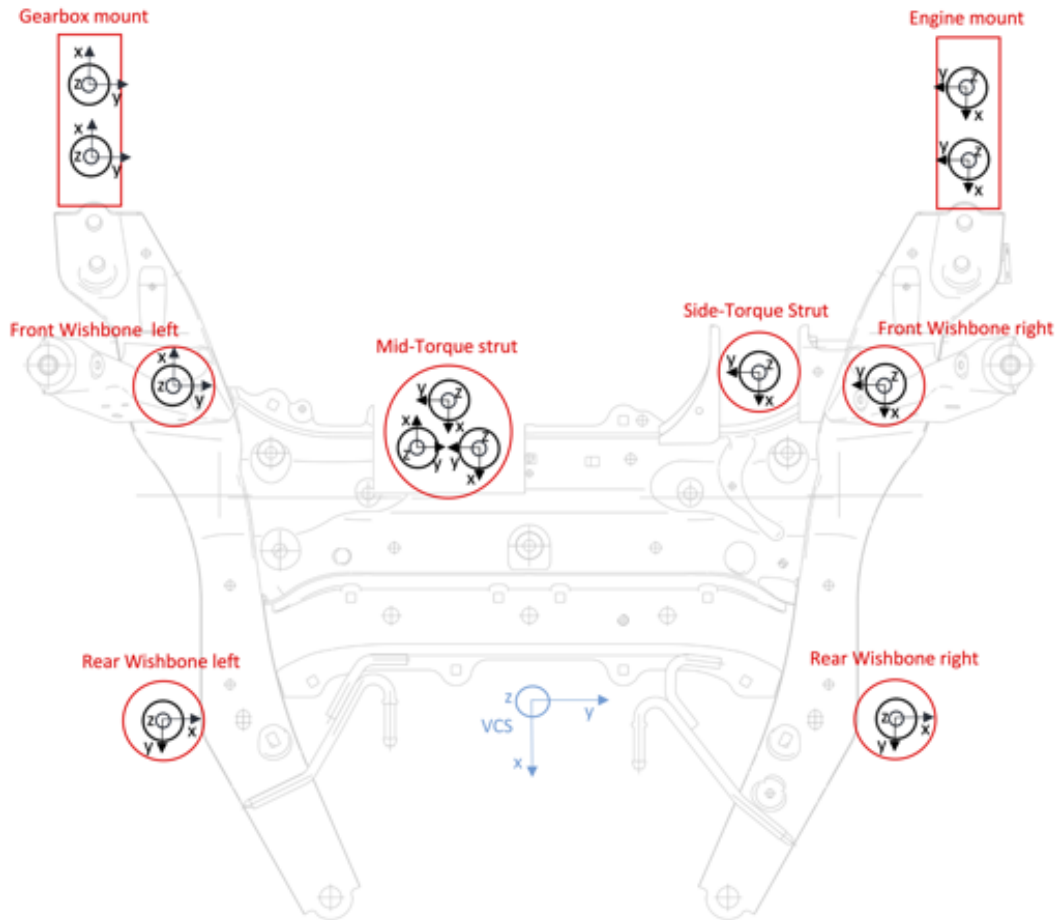


Figure 13: Load cells mounting scheme - In the picture the naming and the locations of the different load cells utilized is represented. For each sensor an orientation is also defined.

The sensors used are all triaxial. The most relevant properties, as available from the table, given by the supplier, Kistler, are reported in [5](#)

Each load cell is mounted utilizing a precise positioning, this is guaranteed through screws. The preload necessary for the correct functioning of the load cells is statically measured during the installation. The selected sensors are intended for measuring

Kistler - Type 9077C			
	Range [kN]	Threshold [N]	Sensitivity [$\frac{mV}{N}$]
F_x, F_y	-75...75	< 0.01	≈ -4.2
F_z	-150...150	< 0.01	≈ -2

Table 5: Load cell technical data according to [1].

dynamic and static forces.

In many diagrams the axis of abscissas is used as the engine RPM. This type of representation allows to highlight the correlation between the studied phenomenon and the engine operation. The conversion to frequency is immediate and can be calculated using the simple formula:

$$Frequency[Hz] = \frac{Order\ n^\circ \times rpm}{60}$$

where for the engine used, being this a 3 cylinder, the order number is 1.5.

3.2 Powertrain kinematic analysis

In this section a quick recall on the mathematical equations for the calculation of a rigid body mounted using soft rubber mounts is given.

If the mounts in question are soft "enough" in the frequency range of the analysis, the system can be considered linear and the mounts are isolating enough the chassis from the structure then is true what follows.

3.2.1 Derivation of the body acceleration equation

In order to calculate the body acceleration \vec{a}_B , an equation consisting of known quantities must be derived. The position and measured values of the sensors (translational and rotational accelerations) are known. Therefore, the equation of the relative acceleration of 2 points in a rigid body can be used as a starting point.

$$\vec{a}_i = \vec{a}_B + \vec{\omega}_B \times \vec{r}_i \tag{14}$$

In this case \vec{a}_B is the acceleration of a reference point or body acceleration, $\vec{\omega}_B$ is the angular acceleration of the reference point or body angular acceleration, \vec{a}_i is the acceleration of the sensor (here 6 sensors in total) and \vec{r}_i is the position vector of the sensors with respect to the virtual reference point. To facilitate the further steps, equation 1 is simplified so that the cross product disappears. This is done with the properties of the skew symmetric matrices $\vec{x} \times \vec{b} = [\tilde{x}]_{3 \times 3} \cdot \vec{b}$ and $[\tilde{x}]^T = -[\tilde{x}]$.

$$\vec{a}_i = \vec{a}_B + \vec{\omega}_B \times \vec{r}_i \quad (15)$$

$$= \vec{a}_B - \vec{r}_i \times \vec{\omega}_B \quad (16)$$

$$= \vec{a}_B - [\tilde{r}_i] \vec{\omega}_B \quad (17)$$

$$= \vec{a}_B + [\tilde{r}_i]^T \vec{\omega}_B \quad (18)$$

Equation [18](#) must be further simplified so that the unknown acceleration vectors, \vec{a}_B and $\vec{\omega}_B$, can be isolated. For this purpose, \vec{a}_B and $\vec{\omega}_B$ are combined into a 6×1 -body acceleration vector $\{a_B\}$ and a so-called forward matrix $[V_i]_{3 \times 6}$ is created as a linear mapping between $\{a_B\}$ and \vec{a}_i .

$$\vec{a}_i = \begin{bmatrix} \backslash & 1 & \backslash \end{bmatrix} \vec{a}_B + [\tilde{r}_i]^T \vec{\omega}_B \quad (19)$$

$$= \begin{bmatrix} \begin{bmatrix} \backslash & 1 & \backslash \end{bmatrix} \\ [\tilde{r}_i]^T \end{bmatrix} \begin{Bmatrix} \vec{a}_B \\ \vec{\omega}_B \end{Bmatrix} \quad (20)$$

$$= [V_i] \{a_B\}, \quad [V_i] = \begin{bmatrix} \begin{bmatrix} \backslash & 1 & \backslash \end{bmatrix} \\ [\tilde{r}_i]^T \end{bmatrix}, \quad \{a_B\} = \begin{Bmatrix} \vec{a}_B \\ \vec{\omega}_B \end{Bmatrix} \quad (21)$$

The accelerations measured by the sensors are represented with respect to the sensor coordinate system. This means that all \vec{a}_i are rotated relative to the global coordinate system (reference coordinate system). In order to use the measured accelerations $\vec{a}_{i,m}$, the torsion must be considered. This is true for all sensors. The equation [21](#) must be adjusted accordingly:

$$\vec{a}_i = [V_i] \{a_B\} \quad (22)$$

$$[R] \vec{a}_{i,m} = [V_i] \{a_B\} \quad (23)$$

$$\vec{a}_{i,m} = [R]^T [V_i] \{a_B\} \quad (24)$$

$$\vec{a}_{i,m} = [V_i] \{a_B\} \quad (25)$$

The two matrices occurring can be combined into a single matrix, namely $[V_i]$ to simplify the notation.

As mentioned above, $\vec{a}_{i,m}$ is the acceleration vector of a sensor. The equation [25](#) can be rewritten for the case when N sensors are present. In this case, all forward matrices are merged together. The same is true for the acceleration vectors of the sensors.

$$\{a\} = [V]\{a_B\}, \quad [V]_{3N \times 6} = \begin{bmatrix} [V_1] \\ [V_2] \\ \vdots \\ [V_N] \end{bmatrix}, \quad \{a\}_{3N \times 1} = \begin{Bmatrix} a_{1x} \\ a_{1y} \\ a_{1z} \\ a_{2x} \\ a_{2y} \\ a_{2z} \\ \vdots \\ a_{Nx} \\ a_{Ny} \\ a_{Nz} \end{Bmatrix} \quad (26)$$

The resulting equation describes a linear mapping between the acceleration vectors of the N sensors and the body acceleration vector. Thus, it is now possible to invert the total forward matrix $[V]$ and use it to calculate the body acceleration. However, for the case $N \neq 2$, $[V]$ the matrix is rectangular, and thus not directly invertible. The Moore-Pensore pseudo-inverse is then used. This method allows for the inversion of singular or non-square matrices. In the end, the final equation is obtained, which is used for the calculation of the body acceleration vector.

$$\{a_B\} = [V]^+\{a\} \quad \text{with} \quad [V]^+ = \left([V]^T[V]\right)^{-1} [V]^T \quad (27)$$

3.2.2 Powertrain accelerations

The analysis starts with importing the data acquired from the test bench. The information of the experiment description, position and orientation of the sensors and frequency range are given. It is, moreover, possible to activate/deactivate single accelerometer's channels. The purpose of this procedure is to select the desired sensor channels so that, for example, channels with high noise can be disregarded.

From the measured data, the kinematic analysis is started. From this, 2 matrices are formed, one with the real part of the sensor accelerations $[a_{Re,m}]$ and one with the imaginary part of the sensor accelerations $[a_{Im,m}]$. The matrices belong to $\mathbb{R}^{3N \times M}$, where N is the number of sensors (here $N = 6$) and M is the number of frequency stamps in the measurement (here $M = 241$). The forward matrix $[V]$ is formed according to the equations [21](#) and [26](#). The used location vectors \vec{r}_i are already known and thus all forward matrices $[V_i]$ are formed. As already mentioned in the derivation, the single forward matrices are rotated with the orientation data of the sensors and then the whole forward matrix $[V]$ is assembled. To calculate the body acceleration the pseudo inverse ([27](#)) is calculated. Using $[V]$, $[a_{Re,m}]$ and $[a_{Im,m}]$, the real and imaginary parts of the body accelerations can be calculated

according to Eq. [27](#) can be calculated:

$$\begin{aligned}\Re[a_B]_{6 \times M} &= [V]_{6 \times 3N}^+ \Re[a_m]_{3N \times M} \\ \Im[a_B]_{6 \times M} &= [V]_{6 \times 3N}^+ \Im[a_m]_{3N \times M}\end{aligned}$$

Finally, the body accelerations and the forward matrix are used to calculate the simulated data (according to Eq. [26](#)). In this step 2 matrices are created, one contains the real part of the simulated accelerations and the other the imaginary part:

$$\begin{aligned}\Re[a_s]_{3N \times M} &= [V]_{3N \times 6} \Re[a_B]_{6 \times M} \\ \Im[a_s]_{3N \times M} &= [V]_{3N \times 6} \Im[a_B]_{6 \times M}\end{aligned}$$

The simulated and measured data are now to be compared. For this purpose, a new quantity is introduced, the consistency.

3.2.3 Geometric Consistency

The geometric consistency is used as a metric to check the accuracy of the simulated data. A similar approach can be found in the thesis of Häussler [\[60\]](#), and van der Seijs [\[5\]](#). First, the difference between measured and simulated data is formed, for both real and imaginary parts. The magnitude of all values in both difference matrices is taken. Both matrices are then summed row by row and a $3N \times 1$ column vector ($\{e_{Re}\}$ and $\{e_{Im}\}$) is formed, whose elements correspond to the total difference for each sensor (in x , y and z directions, respectively). The new column vectors are added together and a total difference vector $\{e_{ges}\}$ is formed. This latter is scaled relative to the maximum resulting value. Both matrices, measured real and imaginary part matrix, are considered. Then, further scaling is performed so that the vector represents the average deviation, finally it is divided by $2 \cdot M$, where M corresponds to the number of frequency ranges considered.

The mathematical formulation of the consistency vector is:

$$\begin{aligned}\{Corr\}_{3N \times 1} &= \frac{\Re\{e\} + \Im\{e\}}{\max(\Re[a_m], \Im[a_m]) \cdot 2 \cdot M} \\ \{\Re\}_{3N \times 1} &= (\Re[a_m]_{3N \times M} - \Re[a_s]_{3N \times M}) \cdot \{1\}_{M \times 1} \\ \{\Im\}_{3N \times 1} &= (\Im[a_m]_{3N \times M} - \Im[a_s]_{3N \times M}) \cdot \{1\}_{M \times 1}\end{aligned}$$

The geometry consistency check allows to verify that all accelerometers are working correctly and that their positioning is accurate. Graphical results' comparisons are shown in figure . The results are rather satisfactory. Only the real components of

3 POWERTRAIN MOUNTS CHARACTERIZATION

the accelerations have small errors, while the imaginary components match closely the measured ones. For these functions the measured and synthesized curves lie on each other, making it difficult to distinguish them as far as the x and z components are concerned.

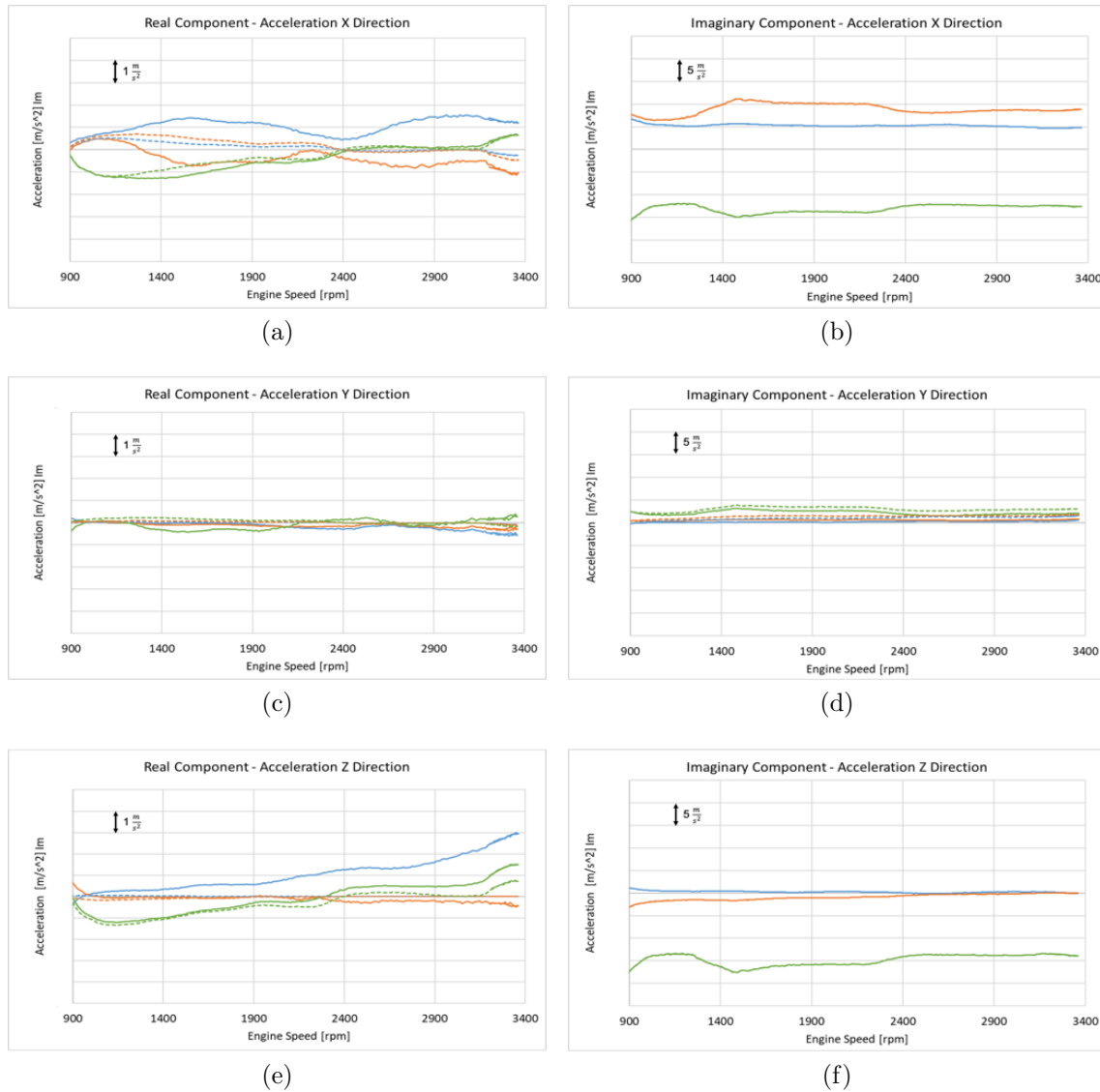


Figure 14: Geometrical consistency for the accelerometers placed on the three main mounts:

- EnM — GeM — TSM (measured values)
- - - EnM - - - GeM - - - TSM (geometric consistency)

3.2.4 Virtual Point

In the introduction to this chapter, the term virtual point was used. In this paragraph we describe what is meant by this definition. Usually, the blocking forces acting between active and passive components are reduced to only 3 DoF, i.e. the translation ones. This is also the case for what is performed for the synthesis of the SPL in this chapter. Especially at low frequency, neglecting the rotational degrees of freedom does not lead to loss of accuracy from the CTPA point of view.

The term Virtual Point (VP) transformation refers to the transfer, based on kinematic considerations, of forces and accelerations at a point. The fact that the complete powertrain behaves as a rigid body, when mounted with insulating elements, and up to 100 Hz, allows to assume that the accelerations within the single mounts can be derived from the global kinematics. Thus, for each mount, a VP is defined which is located at the dynamic elastic center of the mount.

Since the geometric coordinates of the elastic center of each mount can be derived from CAD data, we can refer to the equation [25](#). If in this instead of the matrix $[V_i]$ we use the matrix $[V_{VP,i}]$, where this is defined as:

$$[V_{VP,i}] = \begin{bmatrix} \backslash 1 \backslash \\ [\tilde{r}_{VP,i}]^T \end{bmatrix} \quad (28)$$

The operating accelerations in the VPs placed inside the mounts are thus obtained.

A more general definition is given in the work of Häussler et al. [38](#). One can in general also define a virtual point when the analyzed structure is globally flexible. In this case, the assumption that at least locally, where the [38](#) is defined, the structure behaves rigidly is used. In this way, using an overdetermined system of measurements, forces and accelerations (displacements) can be synthesized in this point.

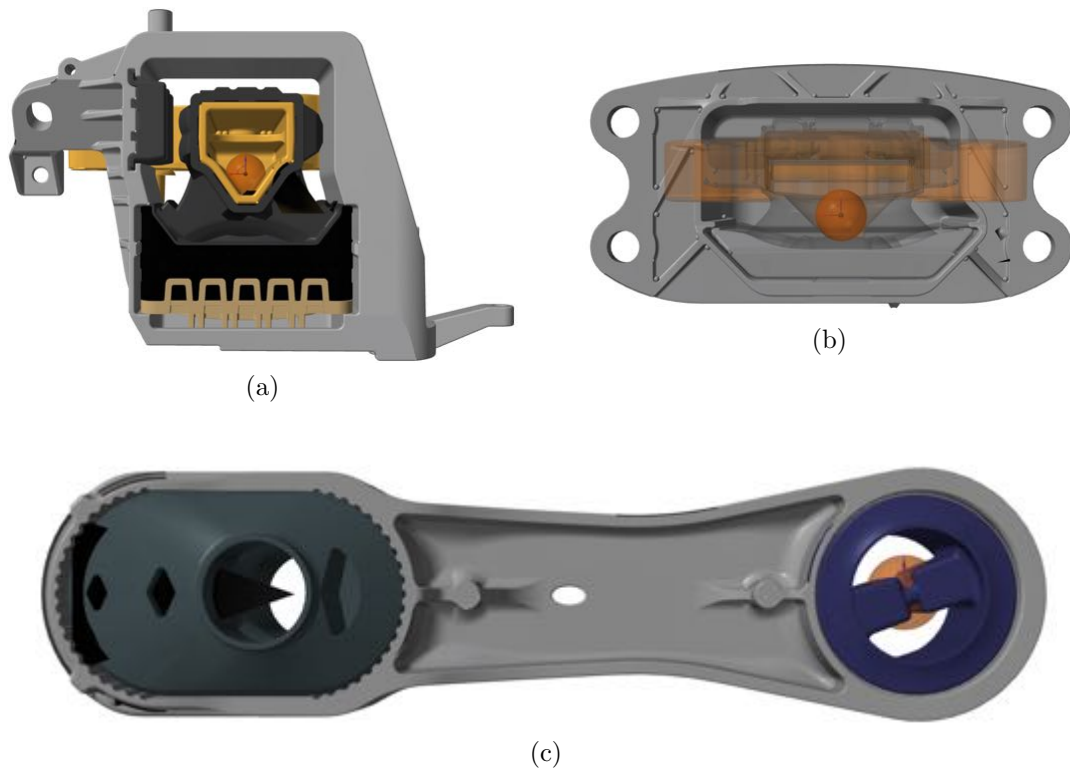


Figure 15: Positioning of the virtual points in the powertrain mounts.
a - Engine Mount
b - Gearbox Mount
c - Torque Strut Mount

As can be seen in the figure [15](#) in each mount the VP in a central position, internally to the mount. This location is chosen coincident with the EC of each mount. This location has the advantages described above.

In the TPA, when synthesis in the VP is not used, accelerations measured near the mount are preferred. Accelerometers and excitations are usually applied as close as possible to the connection point between passive and active components. There is, however, a non-negligible difference between the two methodologies. The positioning of the accelerometers affects the acceleration value. In figure [16](#) an example of the difference between these values is visible. It can be noted how the values differ of about $5m$ around $1600rpm$. This would lead for the two upper mounts to an underestimation of the dynamic stiffnesses while for the TSM the estimation would be more precise.

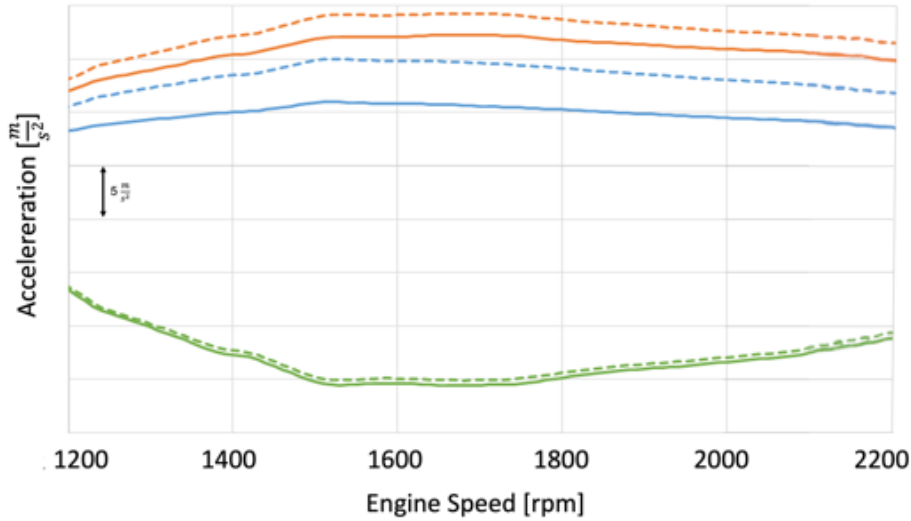


Figure 16: VP - acceleration synthesis. Comparison of values measured outside the mount and synthesized at the virtual point.

— EnM, — GeM, — TSM: accelerations synthetised in the VP
 - - - EnM, - - - GeM, - - - TSM: acceleration measured in the mounts proximity

3.3 Dynamic Force Transfer Procedure

Up to this point the accelerations, and therefore the displacements measured on the operating powertrain, have been synthesized within each mount, using what has been called the virtual point technique. Both in order to perform a synthesis of the SPL using the CTPA, and also to determine the stiffness of the mounts, however, it is necessary to proceed with the determination of the measured blocked forces, in the VP.

To perform this transformation, a procedure has been devised by which dynamic transfer matrices are generated, which allow to transfer the acquired forces to the desired geometrical coordinates.

As previously mentioned, triaxial load cells are mounted under each powertrain mount. Before installing the powertrain, a measurement is performed to determine the transfer functions for the dynamic forces.

For each position of interest, thus EnM, GeM, and TSM, adapters have been produced that allow the application of an inertial shaker. Each one of them allows the shaker to be screwed along the three main directions x, y and z, providing a shaker alignment accuracy of $\pm 1^\circ$, and a mounting accuracy of $0.01mm$. The geometry is designed so that the shaker force is applied in the same geometric coordinates as the VP, in which the powertrain accelerations are synthesized.

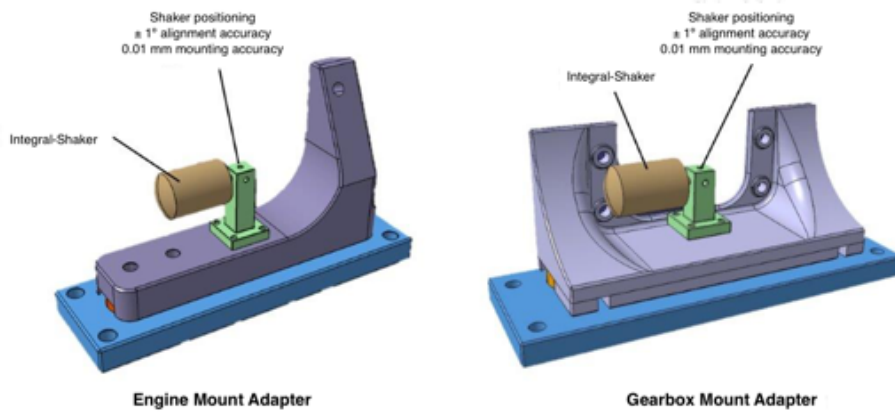


Figure 17: Measurement procedure for obtaining transfer matrices between VPs and force sensors

An inertial shaker from Siemens is used to this practice. Those being designed for the applicability of forces in difficult to reach positions. The inertial shakers generate excitations between $20 \div 20000$ Hz, well above the $20 \div 80$ Hz. After acquiring the signals, the paired force components are added for each measurement position. In this way, for each measuring point three signals are obtained, one for each degree of freedom.

It has been said, although, that the virtual points between active and passive components are defined using 6DoF. Therefore, it can be written in general that:

$$\{\vec{F}_{meas}\} = [FTM]\{\vec{F}_s\} \quad (29)$$

where $\{\vec{F}_{meas}\}$ is the vector of measured forces and moments, while $\{\vec{F}_s\}$ is the vector of forces and moments exerted by the shaker. The transfer matrix $[FTM]$ is a 6×6 dimensionless matrix. In the procedure used, as written above, only the exerted and measured forces are considered, and the moments are neglected. This reduces the number of degrees of freedom of the virtual point to just the translations DoFs.

The individual transfer functions obtained are evaluated in frequency to assess that trend throughout the measured range remains constant.

As can be seen in figure [18](#), where an example is given for the VP of the EnM, the values do not exhibit any frequency dependence. Therefore, it is decided to use the frequency-averaged value as the transfer factor. The procedure was repeated several times, between different uses of the test bench, to verify the stability of the system, which did not show any alterations over the different measurements. The dynamic forces acquired and analyzed, are then multiplied by the corresponding

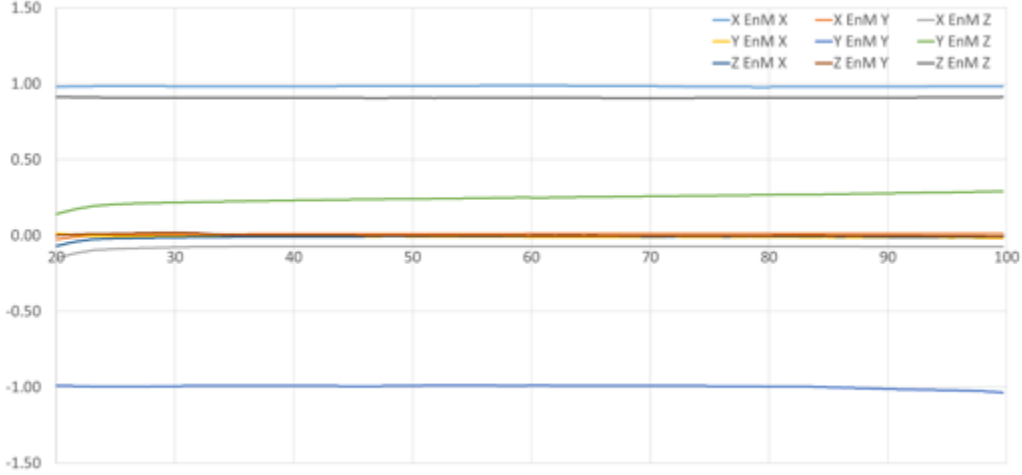


Figure 18: Frequency transmission ratio for individual degrees of freedom measured at the EnM.

transfer functions, thus providing the desired values in the VPs. The effects of any torques are thus corrected for, although the moments are not measured.

3.4 Powertrain Mounts Characterization

From the measurements performed on the test bench, for each degree of freedom of each mount it was possible to define, in VP defined as in [3.2.4](#), the displacements and the dynamic forces acting. Since these quantities are expressed as functions of frequency and torque (static preload), it is possible to map both quantities as a function of these two variables. The dynamic stiffness, which is the intended value, is derived by the complex division of displacement by dynamic forces for each measured frequency.

$$K_{dyn,i} = \frac{\Re(f_i(\omega))\Re(s_i(\omega)) + \Im(f_i(\omega))\Im(s_i(\omega))}{\Re(s_i(\omega))^2 + \Im(s_i(\omega))^2} + i \frac{\Im(f_i(\omega))\Re(s_i(\omega)) - \Re(f_i(\omega))\Im(s_i(\omega))}{\Re(s_i(\omega))^2 + \Im(s_i(\omega))^2} \quad (30)$$

In this way, we obtain the dynamic stiffness, expressed through its real and imaginary components, as a function of three parameters.

$$K_{dyn,i} = f(\tau, d, \omega) \quad (31)$$

Both the real and imaginary components of the dynamic stiffness of the mounts, are therefore representable by a four-dimensional space. Where the main axes are displacement, torque (static preload) and frequency. These parameters define cer-

3 POWERTRAIN MOUNTS CHARACTERIZATION

tain points in the solution space, each of which has a value of dynamic stiffness. The value of this can be identified through a chromatic range. The sidebar in the diagrams is the value in $\frac{[N]}{[mm]}$.

Since interpreting the data into real and imaginary components is not intuitive, a more detailed analysis of the dynamic stiffness of the TSM in the x-direction is presented, analyzing its dynamic stiffnesses as magnitude and phase angle.

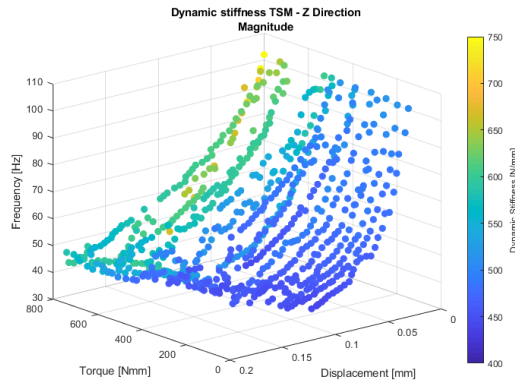


Figure 19: Dynamic TSM stiffness - Magnitude $\left[\frac{N}{mm}\right]$.

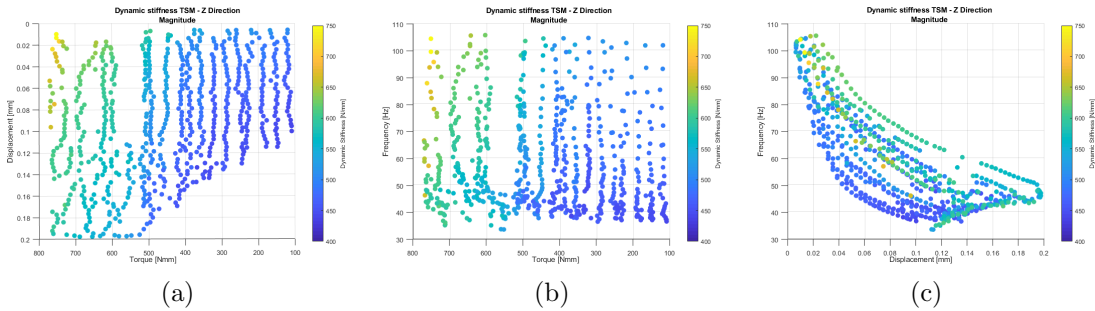


Figure 20: Dynamic Stiffness magnitude in $\left[\frac{N}{mm}\right]$ - Dependence of the individual considered parameters.

In the figure [20a](#) the correlation between torque (static preload) and displacement dependence is visible. Thus for the same torque values, smaller displacement amplitudes mean higher dynamic stiffness. Please note that in this diagram the y-axis is reversed. Therefore, lower displacement values are found at the upper part of the diagram, increasing as moving towards the lower part of the diagram.

3 POWERTRAIN MOUNTS CHARACTERIZATION

In figure 20b we see the relationship between torque (static preload) and frequency dependence. As it can be noticed the most important dependence in this constellation is the one deriving from the torque. In fact, moving on a constant frequency line, it can be observed that as the torque increases, the dynamic stiffness increases consequently.

Finally, the correlation between frequency and displacement dependence is shown in the figure 20c. In this case, the trend, is more difficult to identify due to overlapping data in 3 dimensions. However, it can be observed that for the same frequency, smaller displacements lead to an increase in dynamic stiffness.

The same, more detailed, analysis is also proposed for the phase angle. It can be seen how and in this case, the three variables have an influence on the dynamic characteristics of the mount.

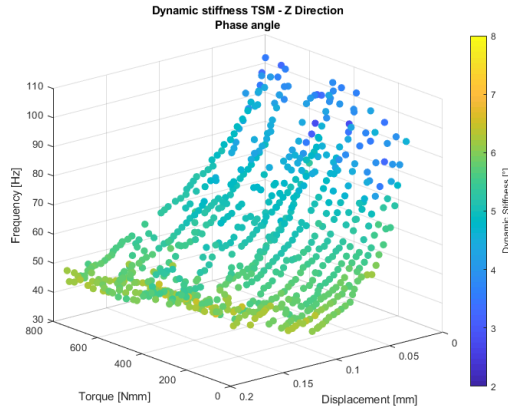


Figure 21: Dynamic TSM stiffness - Phase Angle [°].

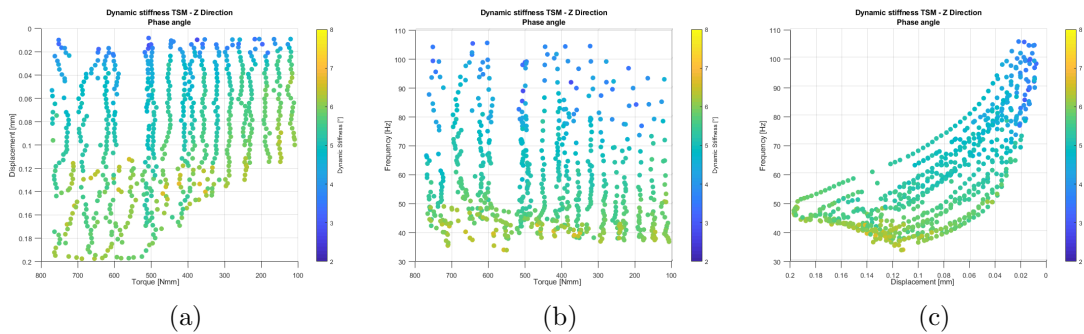


Figure 22: Dynamic stiffness phase angle in [°] - dependence of the individual considered parameters.

This behavior is not always so marked, and easy to be identified. More importantly, can only be evaluated in the x and z components of the obtained dynamic stiffnesses. It must be kept in mind that the excitation force used to characterize the mounts derives, in fact, from the operation of the motor itself. This almost exclusively transfers a torque along its axis of instantaneous rotation. Although this is not exactly orthogonal to the xz plane, it still has a very small angle to the y axis. As a result, the main forcing is an applied moment in y. The main reaction components are therefore reaction forces in the x and z directions. Forces in the y-direction are difficult to observe. This results, in a nonphysical spread of the values of the imaginary component of dynamic stiffness in y. The cause of this behavior is due to the division by values close to zero, as near-zero displacements are measured.

The dynamic stiffness values for three simultaneously measured mounts can be seen in the three figures [23](#) [24](#) [25](#), where in order, the dynamic stiffnesses are represented as real and imaginary components of EnM, GeM, and TSM in x, y, and z directions, respectively. The same results are obtained for each different combination of mounts mounted in the test bench. The data are then exported to a database that allows their further processing.

The final result of a measurement campaign then results in a map of the dynamic characteristics of each mount in each of the three main directions. For simulation reasons, it is preferred to keep the dynamic stiffnesses expressed as real and imaginary components; conversion to other representations is therefore not performed.

3 POWERTRAIN MOUNTS CHARACTERIZATION

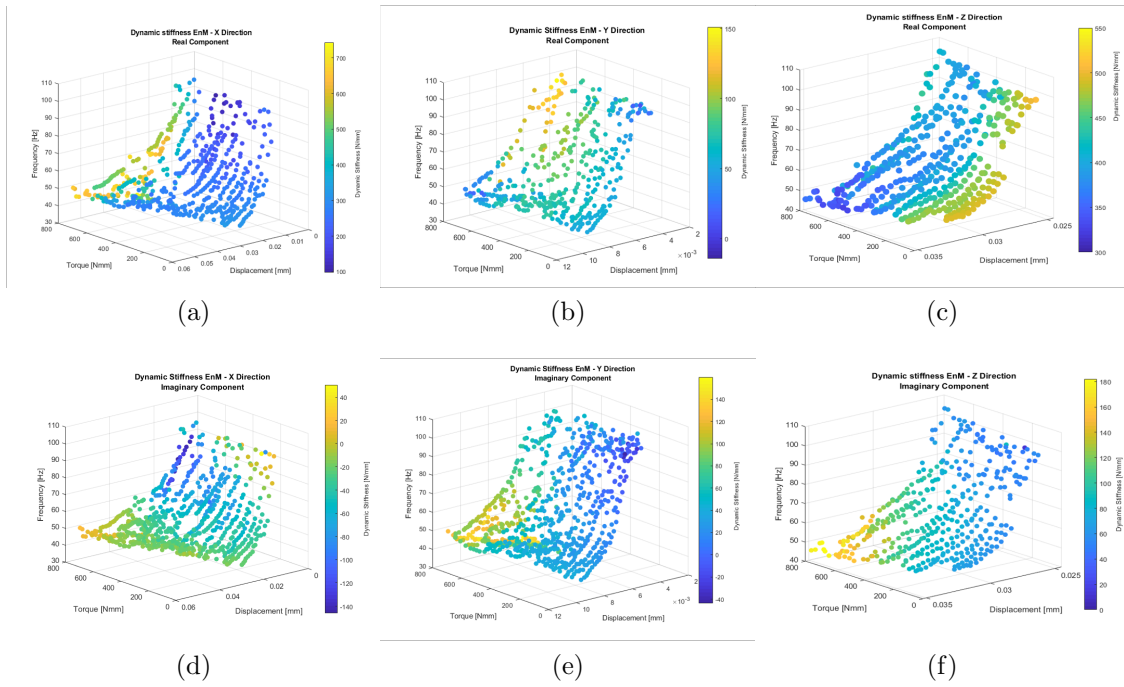


Figure 23: Dynamic Stiffness of the EnM.

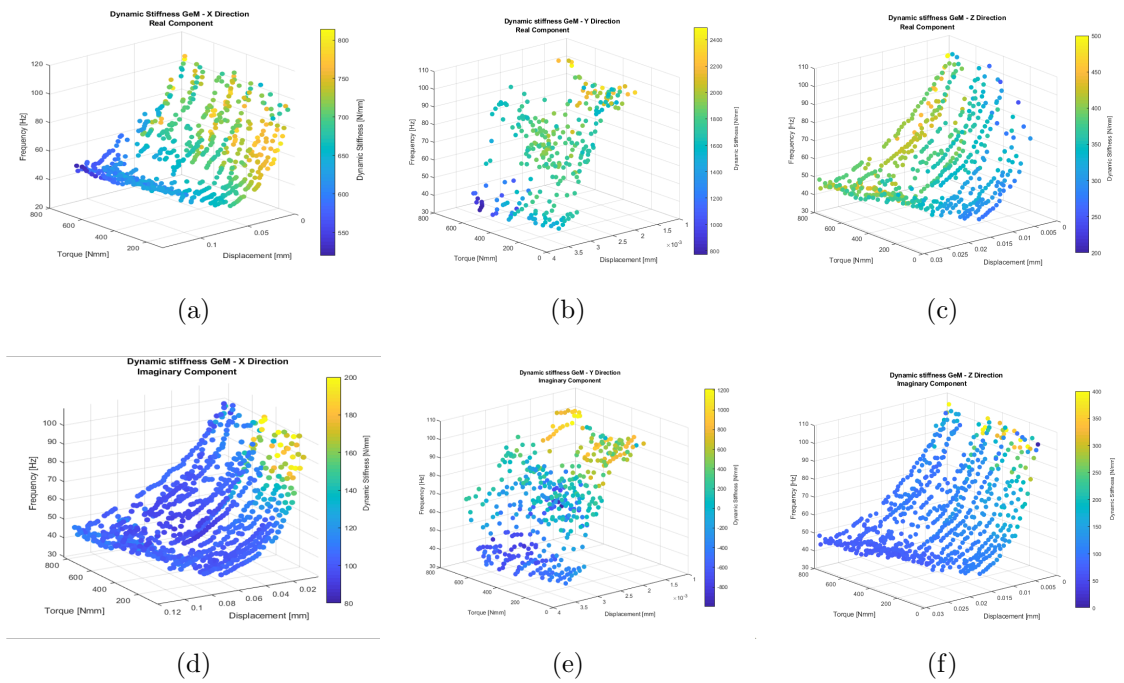


Figure 24: Dynamic Stiffness of the GeM.

3 POWERTRAIN MOUNTS CHARACTERIZATION

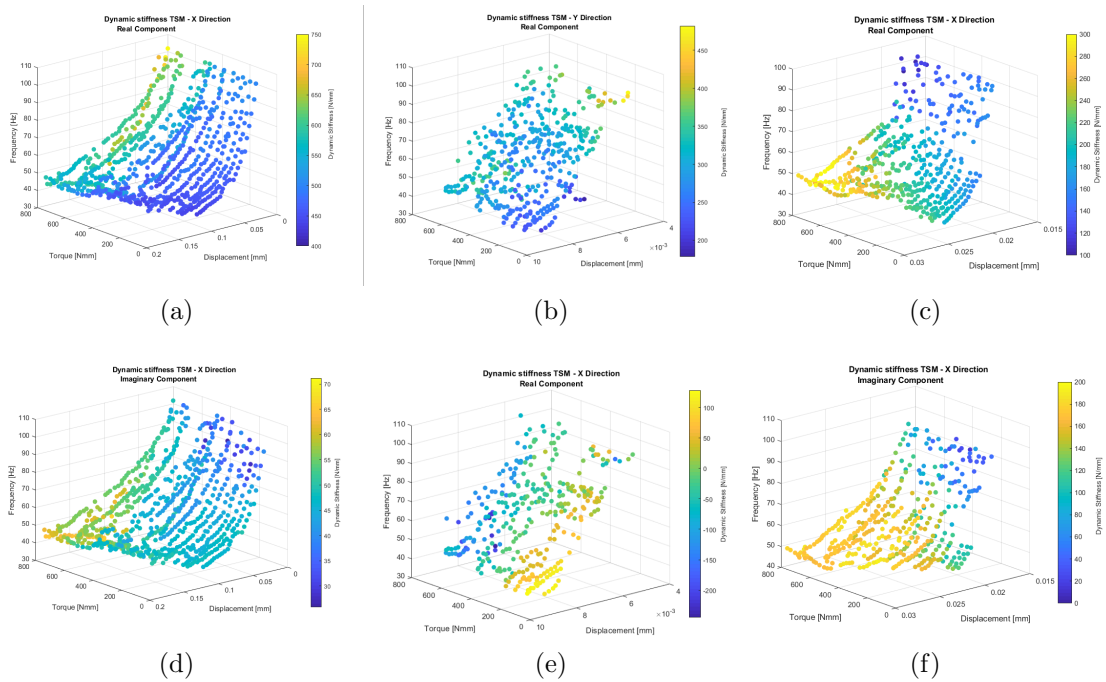


Figure 25: Dynamic Stiffness of the TSM.

3.5 Parametric response model generation

From the obtained dynamic stiffnesses, response surfaces RS are generated. The use of surface responses for the characterization of resilient properties has already been used by Fragasso et al. [61], although limited to the analysis of quasi-static properties.

Although the measurements obtained on the test bench can be used to identify the typical hysteresis that occurs in elastomeric elements, this feature is not modeled. The booming phenomenon resulting from the powertrain was, through driving tests, identified only under acceleration, and not under deceleration. For this reason, the experimentally obtained dynamic stiffness values are filtered, and only values that correspond to an increase in torque are selected.

The surface responses, generated from the experimental values, are generated using a polynomial multire-gression. A polynomial of the third degree is used for each variable considered. The complete formulation can be seen in equation [32].

$$\begin{aligned}
 K_{dyn,i} = & c_0 + \sum_{i=1}^3 p_{\tau,i} \cdot \tau^i + \sum_{j=1}^3 p_{d,j} \cdot \tau^j + \sum_{k=1}^3 p_{F,k} \cdot F^k \\
 & + p_{\tau d} \cdot \tau \cdot d + p_{\tau F} \cdot \tau \cdot F + p_{dF} \cdot d \cdot F + p_{\tau d F} \cdot \tau \cdot d \cdot F \\
 & + p_{\tau^2 d} \cdot \tau^2 \cdot F + p_{\tau d^2} \cdot \tau \cdot d^2 + p_{\tau, d^2} \cdot \tau \cdot F^2 \\
 & + p_{d^2, F} \cdot d^2 \cdot F + p_{d, F^2} \cdot d \cdot F^2
 \end{aligned} \tag{32}$$

The model thus generated would use 20 parameters for the characterization of the dynamic stiffness in each DoF. The analyzed mounts, however, present multiple inflection points in the [Static Force - Dynamic Stiffness] diagram. This representation is an internal standard, which is used to define the characteristic curves of the individual DoFs of a mount. The polynomial model, defined as in equation 32, is therefore found to be inadequate for modeling this strongly nonlinear behavior. An example, of what has just been described can be seen in figure 26. The data scatter in this figure, is due to the three-dimensionality of the graph. In fact, the graph derives from a 2-dimensional projection of a 3-dimensional graph.

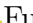



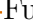
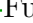


Figure 26: Multiple inflection points in a typical static force - dynamic stiffness diagram. The inflection points are highlighted with red markers. The domain is divided into two halves, identifying a static preload value as the splitting point. In the vicinity of such a point the two generated models are overlapped admitting a 2% superposition.

To overcome this problem, the solution space is divided into two parts, using the static preload parameter as the value to define the division point. In this way, two different models are used, one for low values of static preload and one for higher values of static preload. This split point is identified using the error of the values extracted from the RS as a criterion in comparison to the measured values. When the value exceeds the predefined threshold of 3%, the split point is identified. From this, a second model is then generated to fit the remaining points. For the addition of the two models, a 2% overlap is used at the split point. The models generated in this way use, therefore, 40 parameters for characterizing each degree of freedom of each mount.

To validate the surface responses, a stepwise procedure is followed. First, a direct comparison is executed between the directly obtained dynamic stiffness values and the values extracted from the generated response surfaces. A kinematic model of the powertrain is used to extract individual dynamic stiffness values. Using a vector describing the motor torque, and one describing the powertrain displacement, the dynamic stiffnesses, as a function of frequency, can be extracted from the response surface and compared to values directly calculated using experimental data.

Data from 6 specific operating conditions are used to perform this verification. These are the last 3 available gears at different motor torque values (booming noise typically occurs at higher gears). As previously mentioned, the torque can be controlled during the measurements. In the list below, the legend color coding, for the following graphs is given. The solid lines refers to measured quantities, while the dotted ones represent the synthesized data.

-  Full load in 5th gear, limited to 120Nm
-  Full load in 5th gear, limited to 220Nm
-  Full load in 6th gear, limited to 120Nm
-  Full load in 6th gear, limited to 160Nm
-  Full load in 6th gear, limited to 220Nm
-  Full load in 7th gear, limited to 220Nm

The following graphs, [33](#), [34](#), [35](#), [30](#), , share the description laid out in the bulleted list above. For the sake of simplicity, the graph legend is not defined for each image separately.

3 POWERTRAIN MOUNTS CHARACTERIZATION

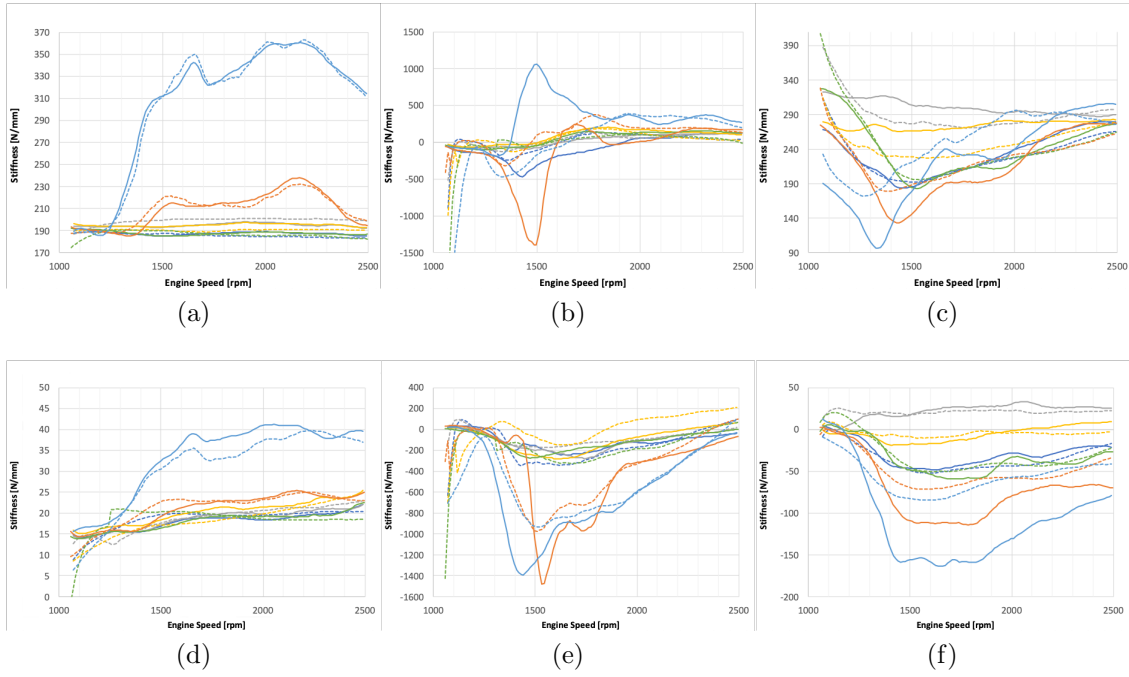


Figure 27: Dynamic Stiffness of the EnM

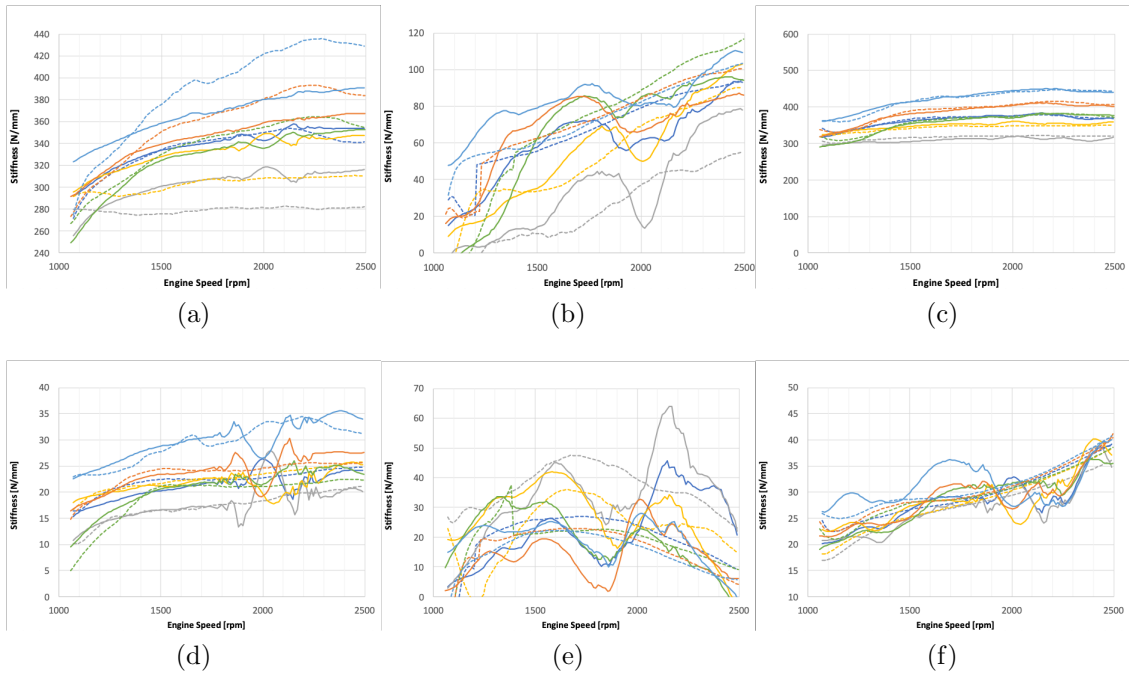


Figure 28: Dynamic Stiffness of the GeM .

3 POWERTRAIN MOUNTS CHARACTERIZATION

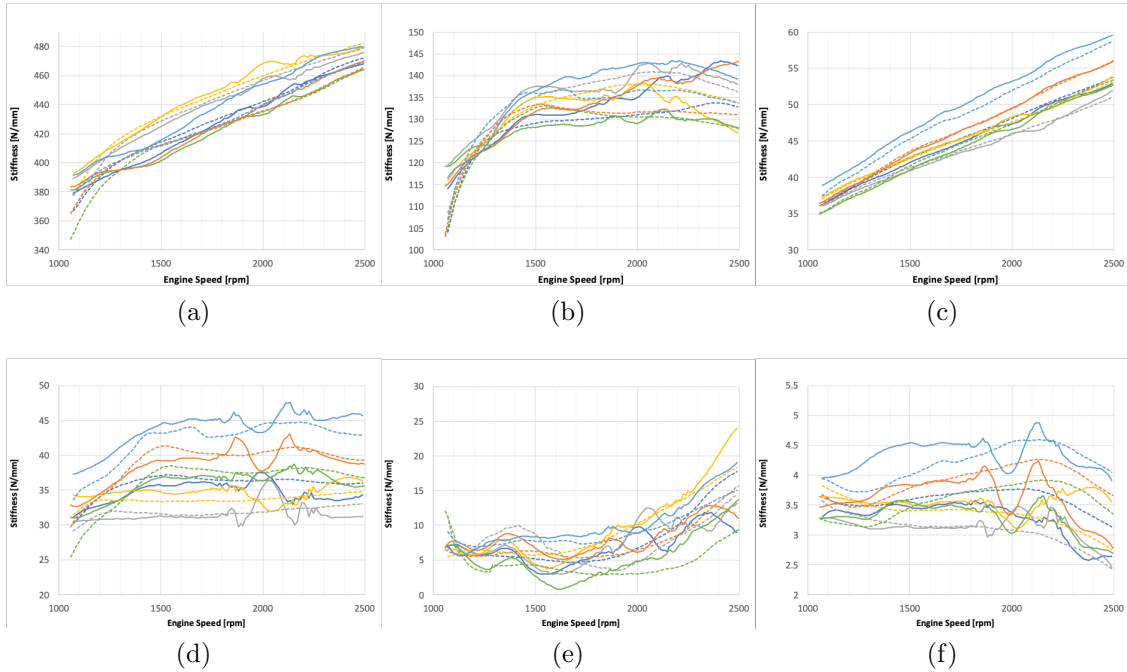


Figure 29: Dynamic Stiffness of the TSM.

Considerations can be directly drawn from the graphs. The dynamic stiffness values obtained from RS are generally able to represent the values obtained from measurements, under all load conditions. This is true for both real and imaginary components. Exceptions to this are the DoF y of the EnM and the GeM. As previously described, these two mounts are not sufficiently stressed in this direction, during the measurement and therefore their characterization not satisfactory. Especially for the EnM, up to 1800 $[rpm]$, the simulated results deviate strongly from the measured data. Another characteristic that can be identified is the dependence of dynamic stiffness on preload. It can be observed that with the same gear used, the dynamic stiffness increases significantly as a function of the torque developed. This is in line with what is identified in the dynamic stiffness maps.

It is then proceeded to verify the simulative ability of the RS to simulate the dynamic forces. In fact, since the dynamic forces are, to all intents and purposes, the most important quantities for the synthesis of the SPL. It is then checked, as previously done, whether for the operating conditions previously described, the results are in line with what has been seen for the dynamic stiffnesses.

3 POWERTRAIN MOUNTS CHARACTERIZATION

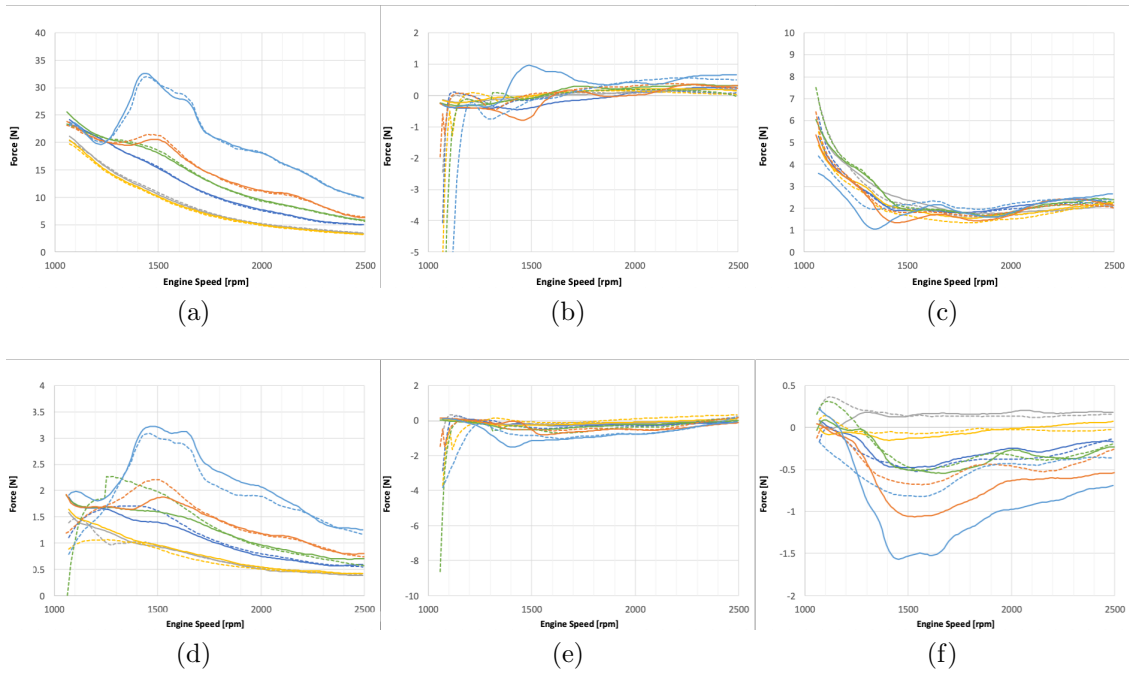


Figure 30: Dynamic Forces of the EnM.

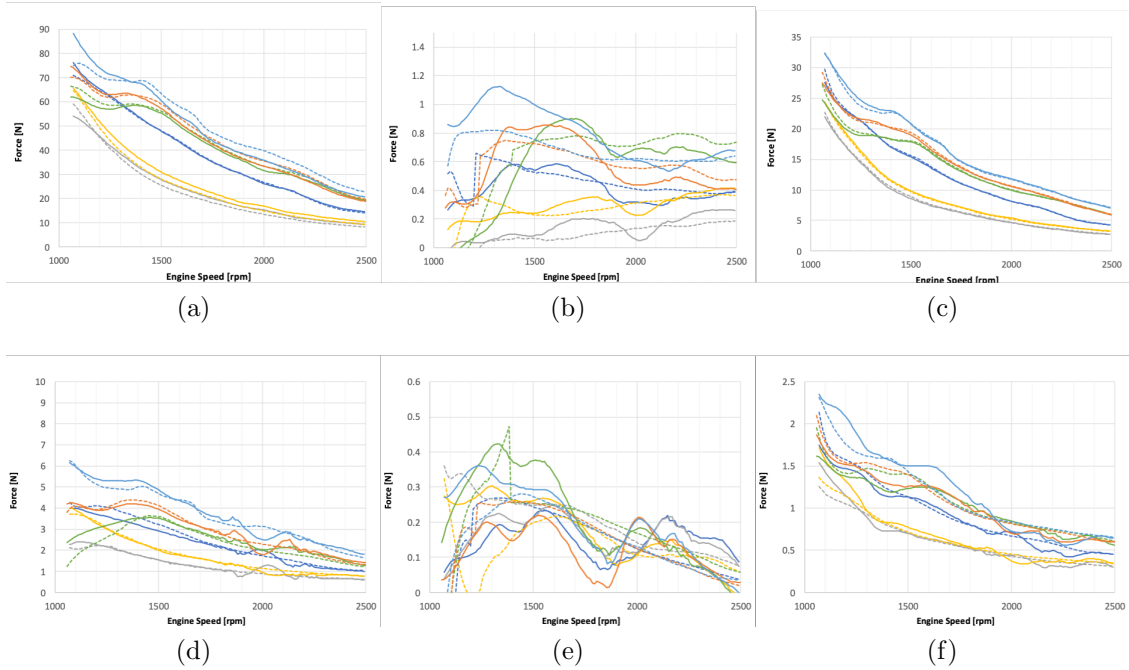


Figure 31: Dynamic Forces of the GeM.

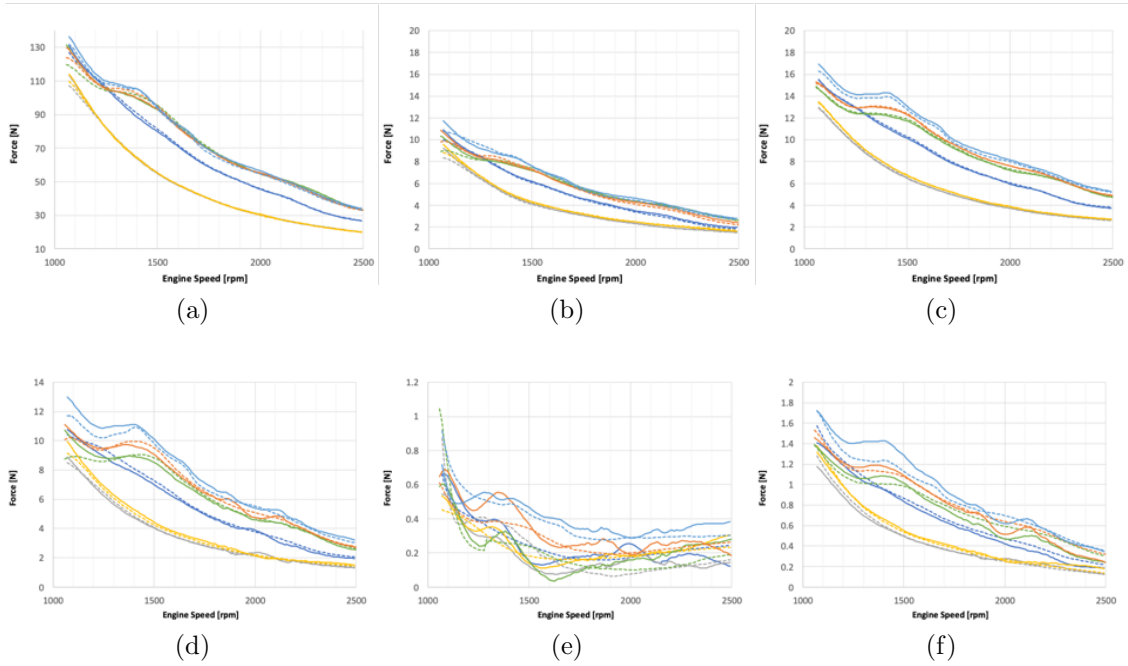


Figure 32: Dynamic Forces of the TSM.

As can be seen in the diagrams [30](#), [31](#), [32](#), the dynamic forces extracted from the RS are very satisfactory. The largest discrepancies between simulated and measured data remains confined to the DoF y of EnM and GeM. In addition, the errors due to the division with near-zero values is reduced, since the divisions with near-zero values are compensated by the multiplication for non-zero displacements. This phenomenon makes the simulated dynamic forces less sensitive to errors.

The last comparison that is proposed involves a direct comparison of dynamic stiffness values as a function of static preload. As described for [26](#), this representation is probably the most widely used in industry. In these graphs, the characteristic curve of the mounts can be recognized. Again, it can be observed that the models generated for the y-components of EnM and GeM are less accurate than all the modeled DoFs. Again, the scatter in the data is due to the projection of three-dimensional graphs into a two-dimensional graph.

3 POWERTRAIN MOUNTS CHARACTERIZATION

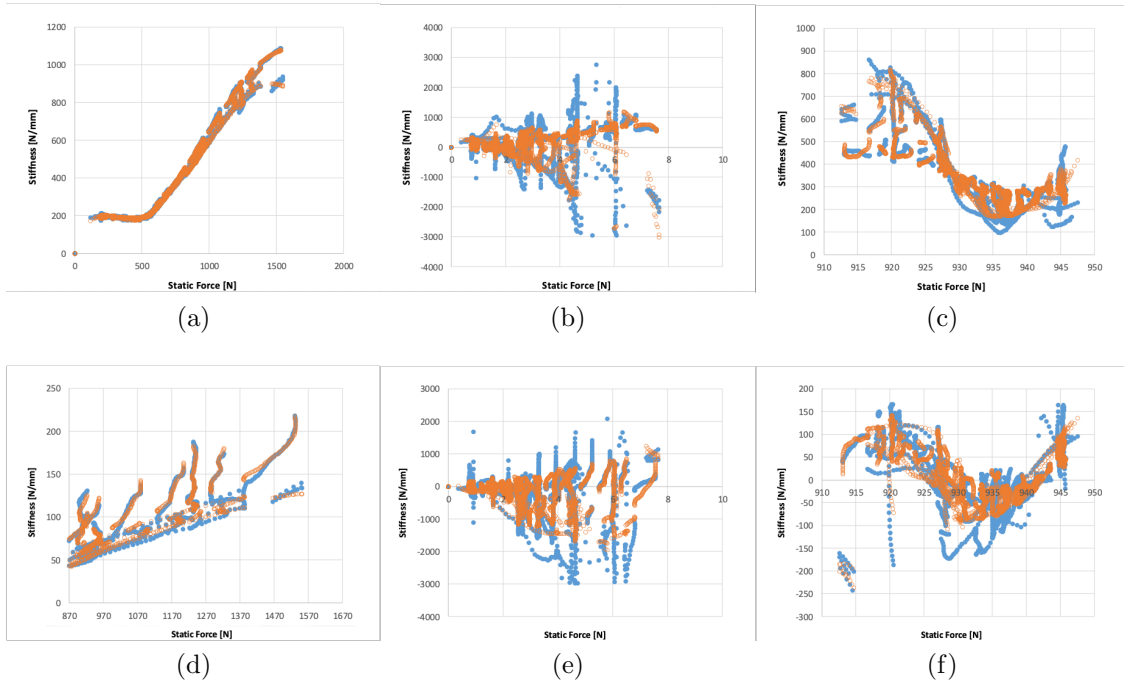


Figure 33: Dynamic Stiffness of the EnM.

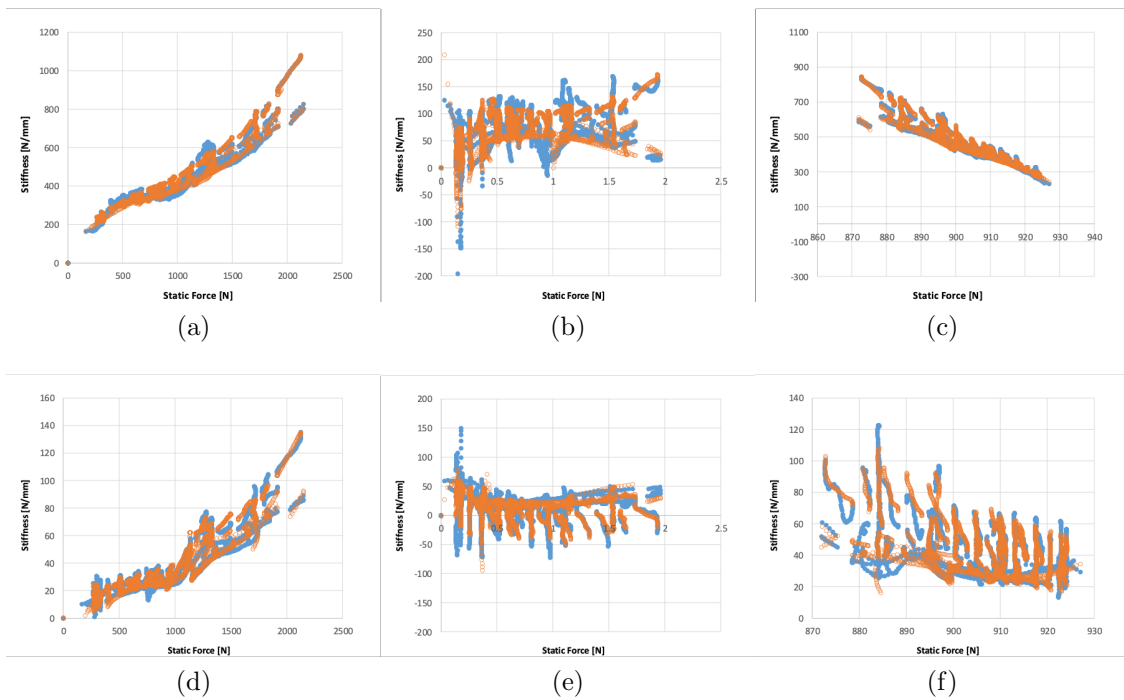


Figure 34: Dynamic Stiffness of the GeM.

3 POWERTRAIN MOUNTS CHARACTERIZATION

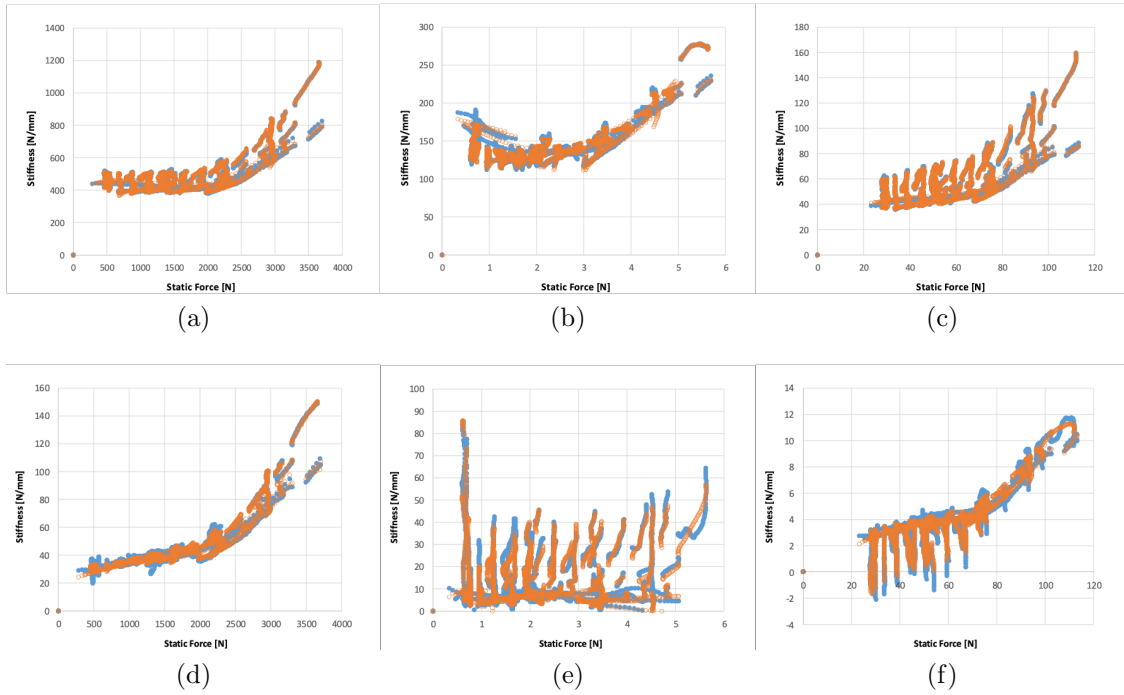


Figure 35: Dynamic Stiffness of the TSM.

All values presented in the diagrams so far are now evaluated in quantitative manner. As a criterion for assessing the reliability of the simulated values relative to the measured values, the R^2 correlation criterion is used. Although this criterion has limitations, especially when applied to assess the accuracy of nonlinear regressions, its value is considered a good method here. First, the expected trend of the curves is known a priori. In this way it can be checked whether the values obtained are plausible. A different situation is when one generates models of functions whose trend is not known a priori. Secondly, numerical validation of the models is followed by validation through the synthesis of the SPL that follows in the next chapters. The results obtained are shown in table 6 regarding the EnM, in table 7 the values of the EnM are shown and finally in table 8 the results regarding the TSM. Values that are not considered satisfactory are highlighted in red. These coincide with what has been seen in the diagrams up so far.

Component	EnM - Dynamic Stiffness			EnM - Dynamic Force		
	X	Y	Z	X	Y	Z
Real	99.978	60.865	99.249	99.975	87.228	99.518
Imaginay	99.665	69.366	88.197	99.614	68.713	82.635

Table 6: R^2 Values for stiffnesses and dynamic forces - EnM

Component	GeM - Dynamic Stiffness			GeM - Dynamic Force		
	X	Y	Z	X	Y	Z
Real	99.654	92.474	99.441	99.794	92.146	99.612
Imaginay	99.441	74.168	98.691	99.612	85.348	98.726

Table 7: R^2 Values for stiffnesses and dynamic forces - GeM

Component	TSM - Dynamic Stiffness			TSM - Dynamic Force		
	X	Y	Z	X	Y	Z
Real	99.976	99.912	99.969	99.975	99.949	99.976
Imaginay	99.828	97.146	99.204	99.874	94.955	99.710

Table 8: R^2 Values for stiffnesses and dynamic forces - TSM

3.6 SPL synthesis and methodology validation

It is at this point necessary to verify if, through the dynamic force acquisition procedure on the test bench, the synthesis of the SPL is in line with that measured in the vehicle during the same operating conditions. Secondly, it is necessary to verify if the dynamic force values obtained from the surface responses allow to obtain the same quality, and if through the generated numerical models it is really possible to generate new PMS configurations. In this way the test bench could be used not only to estimate the SPL due to the forces generated by the engine, but also to identify individually the mounts, and generate a digital twin that allows simulations based on experimental data.

3.6.1 SPL Synthesis

The figure [36](#) shows the values of a measured SPL, with those of a synthesized SPL, in the same conditions, 5th gear wide open throttle. The comparison is performed for the typical booming problem described so far, therefore limited to the range between 20 ÷ 55 Hz.

It can be observed that the synthesis of the acSPL is very satisfactory. Not only is it possible to replicate the trend, but also the general deviation of the generated sound pressure from the simulated one is contained. The maximum deviation among SPL peaks is in fact $3dB$.

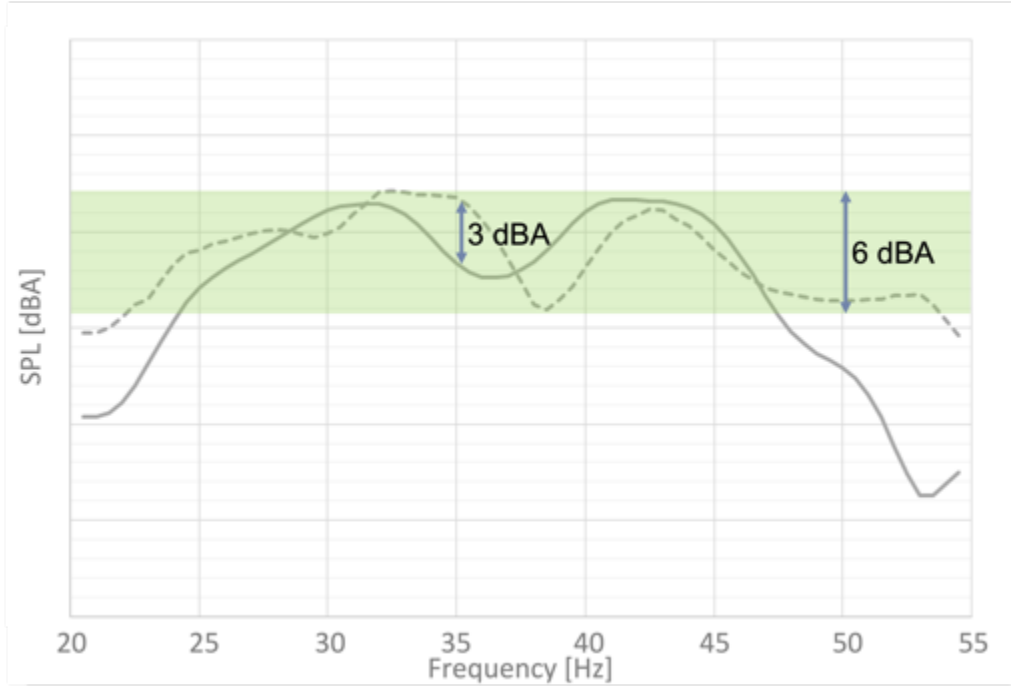


Figure 36: Comparison of the measured and synthesised SPL - A-Weighted

—measured SPL
 ---synthetized SPL

Two correlation criteria are also used, to check the error of sound synthesis, named $corr_f$ and $corr_s$, defined as [62]:

$$corr_f = \|1 - MAC\| \quad (33)$$

Where $corr_f$ represents the correlation error between the two curves considered, and is therefore a criterion that describes the similarity between the measured and synthesized SPL.

$$corr_s = \|1 - MSF\| \quad (34)$$

$corr_s$ describes the error in the amplitude between the two curves.

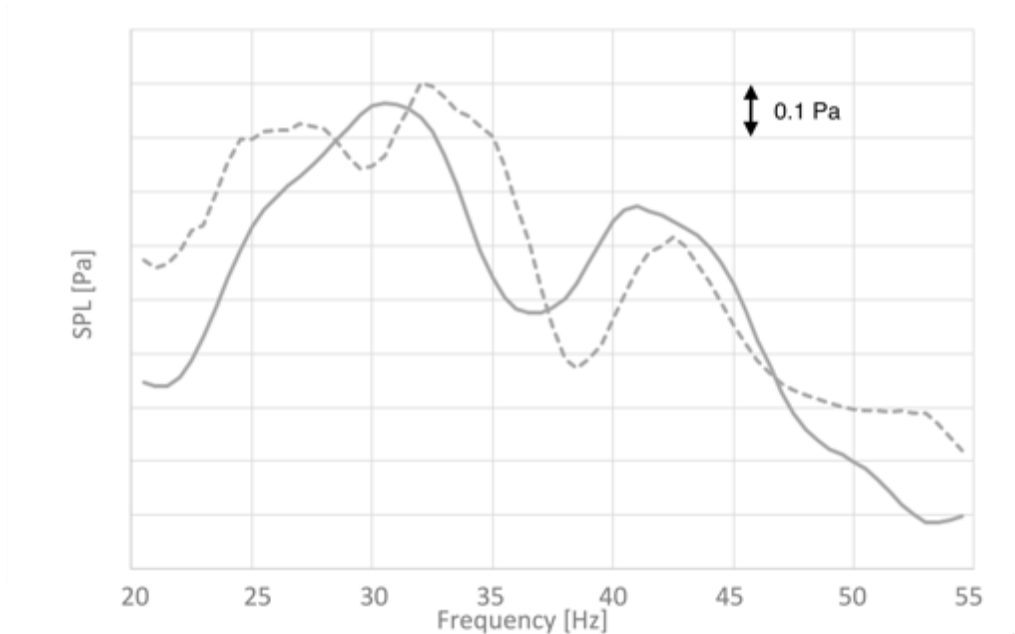


Figure 37: Comparison of the measured and synthesised SPL - synthesis error
 — measured SPL
 --- synthesized SPL

The results of $corr_f$ and $corr_s$ for the specific vehicle considered are 5% and 10%, respectively, and thus guarantee the desired accuracy.

3.6.2 Evaluation of the RS methodology

After verifying the validity of the proposed methodology for acquiring the blocked forces, the verification of the methodology used to characterize the mounts is now carried out.

It has been previously observed, in the [3.5](#) section, that the dynamic stiffness values of the mounts obtained through the RS are in line with those measured. The comparison of the SPL values obtained when the dynamic forces are obtained from the dynamic stiffnesses is now proceeded with.

This comparison is carried out as follows.

A complete set of mounts (consisting of EnM, GeM, TMS and whisbone mounts) is used to attach the powertrain to the test bench. The complete measurement campaign is performed and the characterization of the individual mounts is carried out, as described in [3.5](#). Two approaches can then be used to synthesize the SPL at the driver's ear. First, the dynamic forces transferred into the VPs, acquired during the measurements, can be used. This methodology has been previously validated. Alternatively, one can use the dynamic forces obtained from numerical models of

the dynamic stiffnesses of individual mounts. This comparison is shown in Figure 38. A 5th run at 220Nm is used for the synthesis, under conditions, therefore, of wide open throttle.

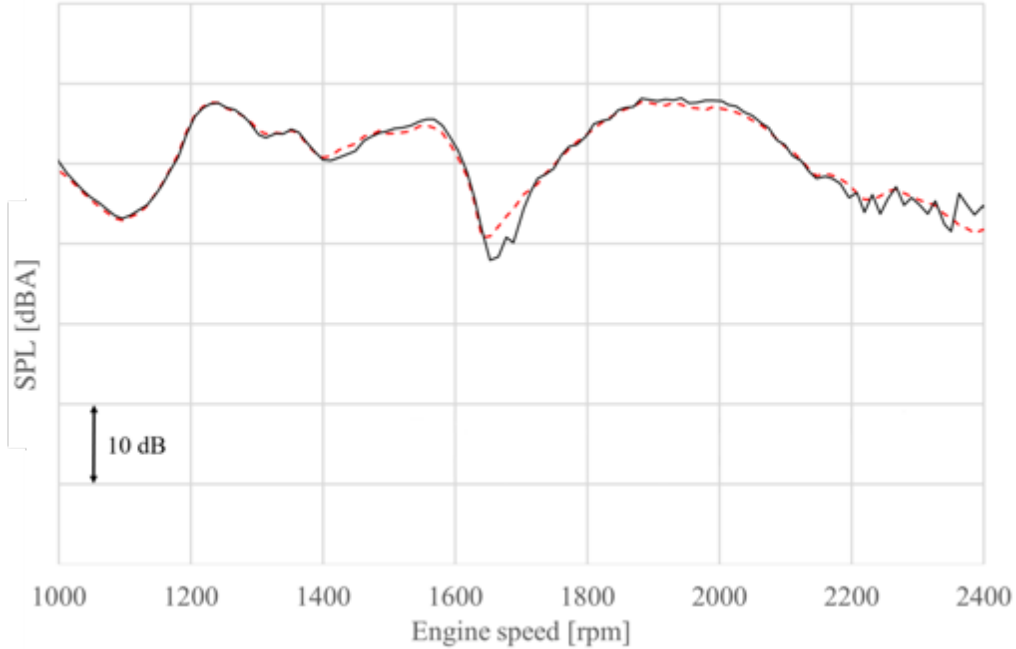


Figure 38: Comparison of the SPL - A-Weighted
 — SPL synthesized utilizing the blocked forces transferred in the VPs
 - - - SPL synthesized utilizing the dynamic forces extracted from RS models

The results are extremely satisfactory for the whole frequency range (engine rpm) considered. In this way the generated surface responses are further validated.

From the above validation, however, it is not possible to determine whether the individual mounts have been characterized independently, or whether the numerical models developed are constrained to the specific simulated design. If this were the case, then through the generation of RS there would be no gain in terms of simulative capability. In fact, the idea is to obtain, through the characterization of each group of PMSs, numerical models of mounts that can then be used to generate virtual designs. As shown in Figure 39.

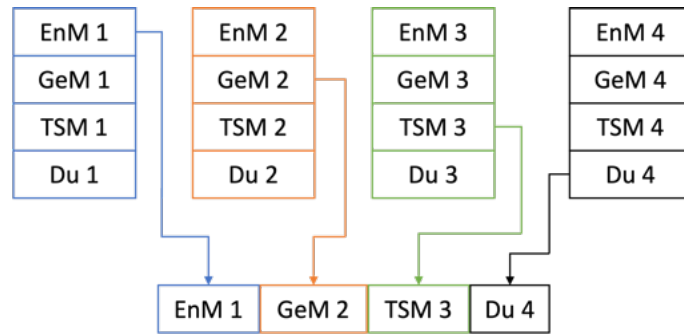


Figure 39: Virtual Design Creation Scheme - Surface mount responses generated are combined to create a new virtual design

Five measurements are then made separately, using the same engine, but changing the sets of PMS used. Following the nomenclature of figure 39, during the first test 4 mounts are characterized, named (1), in the second test another four mounts are characterized, named (2) and so on. A characterization is also performed, using the following mount configuration: EnM1, GeM2, TSM3 and Du4.

A comparison of the synthesized SPLs can now be performed using the dynamic forces obtained directly, or using the dynamic forces obtained from the virtual design, obtained by combining the dynamic forces of the mounts, extracted from the surface responses. The comparison between the measurement used as a reference, and the result obtained from the virtual design can be seen in Figure 40.

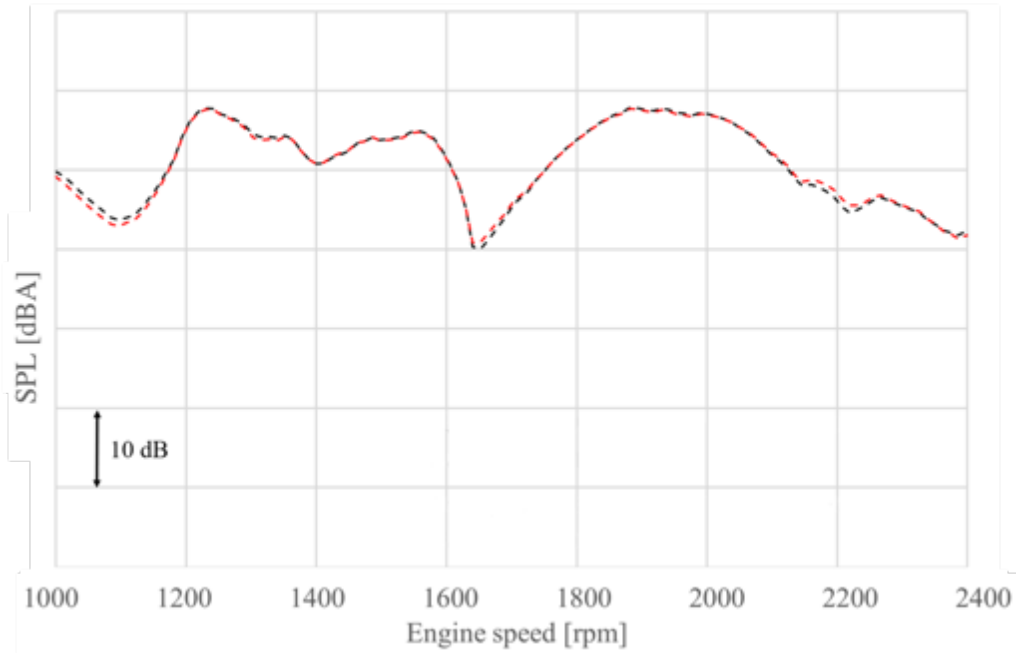


Figure 40: Comparison of the SPL - A-Weighted
 ---SPL synthesized utilizing the blocked forces from the PMS design used as reference
 - - -SPL synthesized utilizing the dynamic forces extracted from RS models used to generate a virtual design

As can be seen, the results are very good, and allow us to conclude that the characterization of the mounts is independent of the configuration in which they are identified. This statement is also valid for motors. The generated surface RS responses can be used in coupling with other engines as well, and in general multiple designs can then be generated from the characterized mounts.

3.7 NTF Estimation Errors

Before proceeding with further analysis, it is desired to dwell again on the synthesis of SPL, and possible sources of errors and uncertainties in the analysis of this phenomenon. Previously, in the chapter on TPA, we described how there is a known variability in the NTFs of different vehicles. However, there is also the risk of failing to control measurement errors when acquiring NTFs from the TMB.

In this chapter we consider the same vehicle, which was used for the SPL synthesis in Figure 38. Indeed, there are several measurements of this TMB that allow for considerations of SPL synthesis. The NTFs of this vehicle (TMB) were acquired

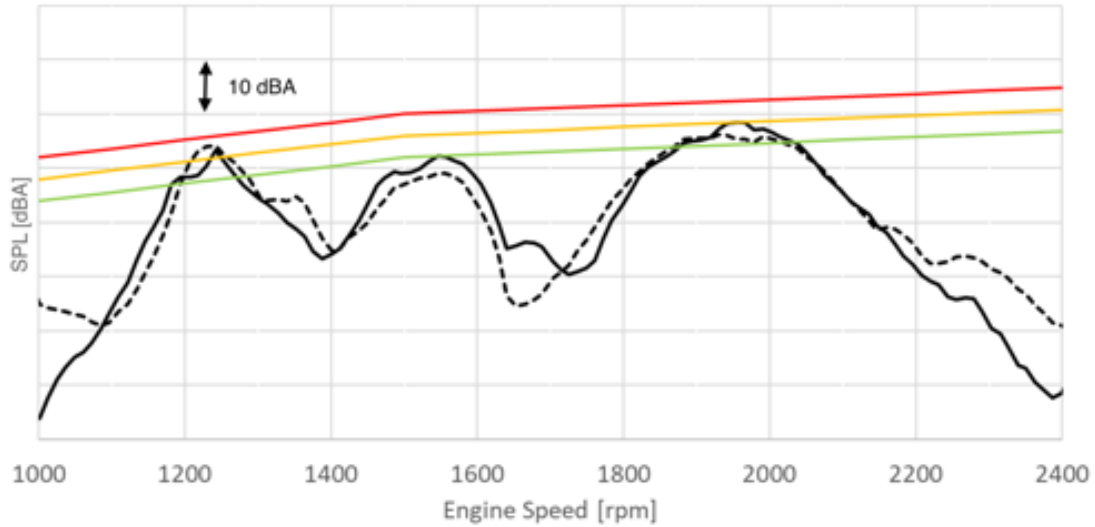


Figure 41: Comparison of the SPL obtained using, NTFs measured by the reciprocal method, and that obtained from instrumented hammer impacts measurements.

- NTF obtained via reciprocal measurements
- NTF obtained via hammer impact measurements.

twice, once using the reciprocity method, and then using point excitations via instrumented hammer. Refer to the section [2.4.1](#) for more details.

Differences in synthesis can be found over the entire frequency spectrum considered. It can be seen how, even in the different SPL peaks, the two curves present differences that are between 1 and 2 dB. Although this value may seem small, in an analysis that aims to reduce errors in the simulations it is important to understand the reason for them. A first indication comes from the analysis of the individual contributions to the total SPL. In figure [42](#) the individual contributions to the total SPL can be observed. First of all we can see that the resulting SPL comes from a compensation of the different paths. In the graph it is possible to observe how the contributions from TSM are compensated by the contributions from EnM and GeM. In order not to complicate further the reading of the graph, the gray line represents the sum of all contributions in the Z direction. Finally, the yellow line shows the contribution of the wishbone mounts in the X direction. All contributions from the Y direction are not represented as they are close to zero.

What can also be seen in figure [42](#), is how the differences due to NTF are not consistent. In fact we can see that in certain frequency ranges the SPL obtained through the reciprocal is higher, and in others is the opposite. To clarify this point it is decided to perform a model analysis of the TMB, to investigate in more detail

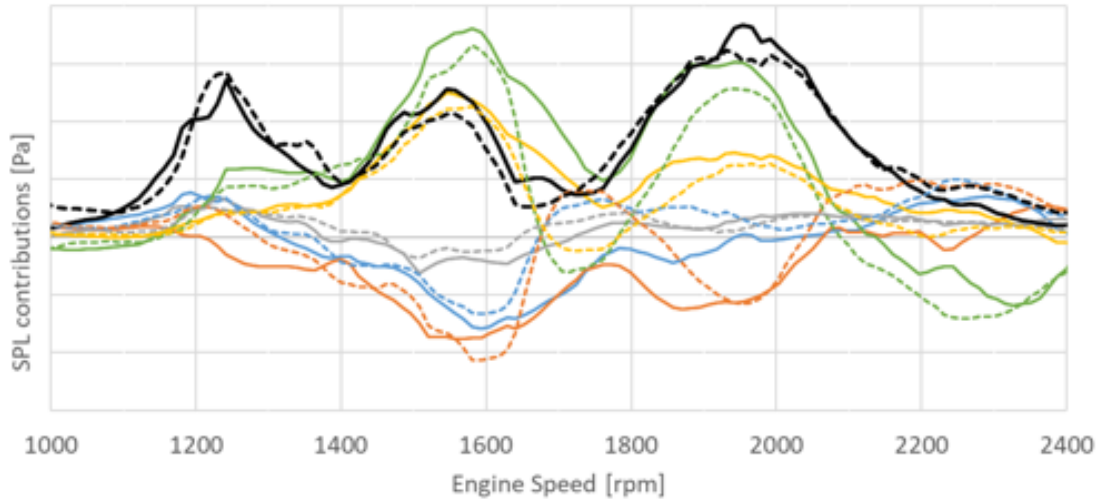


Figure 42: Comparison of the SPL obtained using, NTFs measured by the reciprocal method (—) , and that obtained from instrumented hammer impacts measurements (---).

— EnM - Contribution in X; — GeM - Contribution in X; — TSM - Contribution in X; — Wishbone Mounts (Du) - Contribution in X; — Sum of all contribution in Z.

how the vehicle behaves in the identified SPL peaks.

3.7.1 Vehicle Modal Analysis

SPL synthesis and the study of NTFs are usually not sufficient to identify the mechanism that generates an acoustic phenomenon. In the booming phenomenon, as previously described, the dynamics of the body are coupled to that of the contained fluid. The vehicle surfaces then interact with the fluid. A very interesting discussion on this topic can be found in Brandstätter’s doctoral thesis [63], where the influence of various surfaces on low frequency booming, due to excitations from the road, is thoroughly explained. Therefore it is often necessary to observe the operational deflection shapes of the TMB, or to perform a modal analysis, to identify an acoustic problem. [4].

The theory of modal analysis is well known, so the discussion is left out, for a full and extensive description of the methodology refer to [64]. The modal analysis was calculated using the Siemens Polymax algorithm, and the MLMM criterion, for these refer to [65] and [66].

The modal analysis is performed for the vehicle that will also be considered in the other chapters of this thesis. This is a BMW 2 series Tourer, front wheel drive, with cross engine. The body is the same one used for the SPL synthesis shown in figures [41],[42].

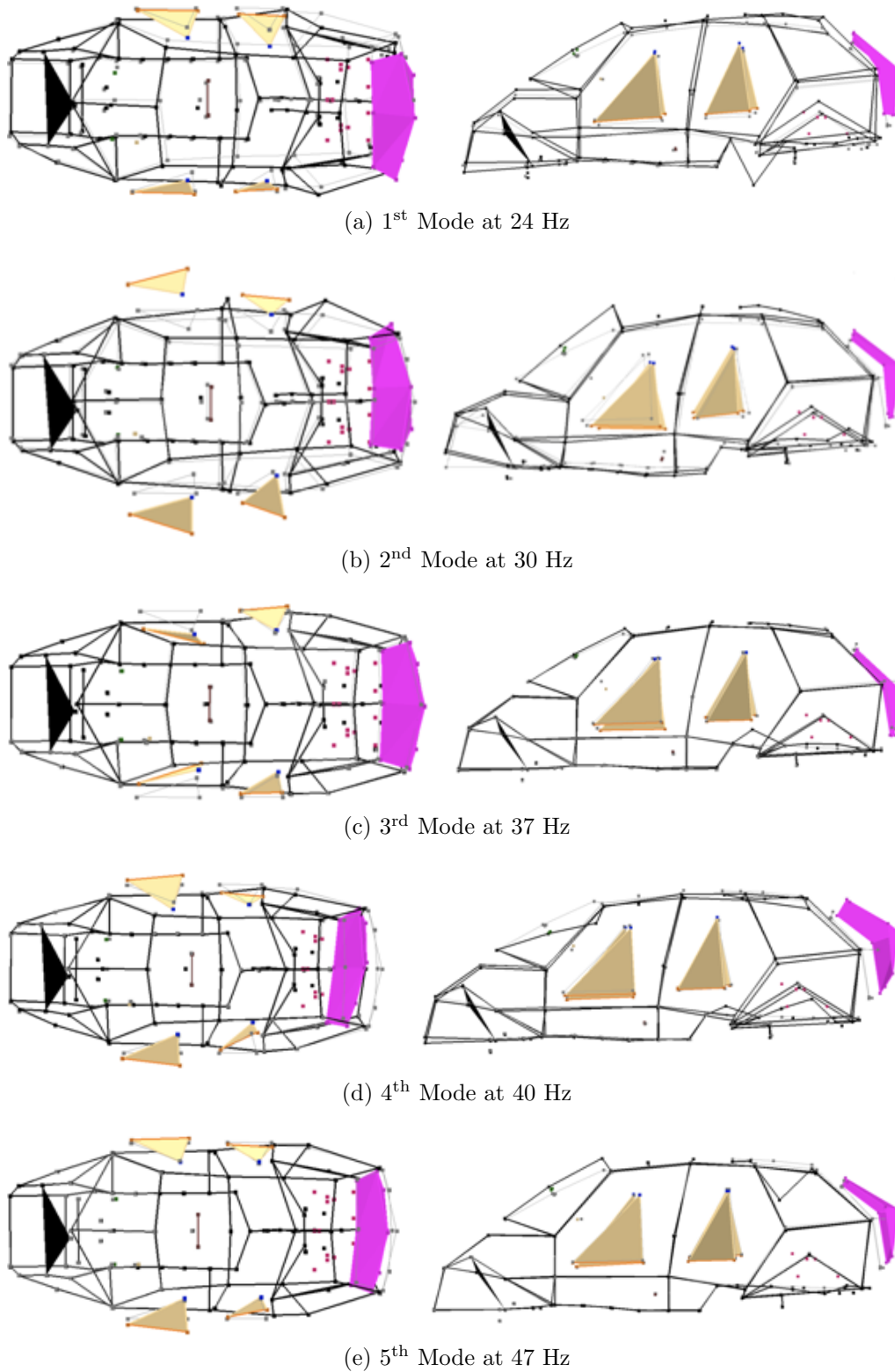


Figure 43: Modal Analysis of the complete TMB - 2 Series Touring. The modal analysis is performed using a reciprocal method (Loud Speaker excitation)

Between 20 and 80 Hz, 5 modes are identified, which are visible in figure [43](#).

- a First mode at 24 Hz - The greatest contribution comes from the trunk floor.
- b Second mode at 30Hz - The TMB reacts with a second flexural mode. The front subframe has a marked flexural behavior on the axis y. Simultaneously doors, front windshield and trunk door excite in phase the volume enclosed in the cabin.
- c Third mode at 37Hz - The main contribution derive from the from the front doors, which in phase excite the volume enclosed in by the cabin.
- d Fourth mode at 40Hz - The mode shape in in this case dominated by the contribution of the trunk door. The rear side doors move in phase with it, exciting the fluid, while the front side doors move in anti-phase.
- e Fifth mode at 47Hz - the main contributions derive from the roof (antenna area) and the trunk floor. They move in phase towards the cabin volume. The front carrier has a torsional behavior around the x axis.

Of the five identified modes, the most interesting is certainly the first. In this modal shape, it can be seen how the front carrier undergoes a bending, which has as its axis of rotation a point located near the TSM. It is therefore clear how a non-perfect positioning of the accelerometers placed on the components of the front carrier, can magnify or reduce the displacements detected. The SPL peak at 1550rpm is characterized by the overlap of the two modes identified at 37 and 40Hz. Especially in the 40 Hz modal shape, the fluid volume inside the cabin is excited by the windshield and the trunk door. However, it can also be seen that the front carriage exhibits a slight bending, making it sensitive to accelerometer misplacements in this area. The last mode, in which the roof contributes in a dominant way to excite the cabin fluid, presents a torsion of the front carrier around the x-axis (direction of travel). This way, again, makes the results particularly sensitive to the positioning of the accelerometers.

3.8 Optimization

Up to this point, it has been verified that the methodology developed to measure blocked forces, guarantees a very good synthesis of the SPL for the desired frequency range. It is also seen that the developed RS are able to model the mounts with accuracy, and allow to synthesize the SPL in a reproducible manner. Since the numerical models are fully parameterized, the logical next step is to perform an optimization to reduce the SPL in as many vehicles as possible.

This section then presents the optimization of all powertrain mounts simultaneously. For the synthesis of the SPL, mechano-acoustic noise transfer function data

are used. It is thus possible to consider the variability of the passive side and the active side at the same time. The optimization also uses real stiffness values. The parameters of the mounts are allowed to vary within ranges applicable in an advanced state of development. The goal is in fact to generate a solution that can be really industrialized, without altering the development costs.

3.8.1 Design of experiments - all vehicles

The optimization study is carried out on a group of 15 vehicles. Since data from vehicles are not easy to obtain except with intensive measurement campaigns, and as already specified, it is difficult to obtain reliable synthetic transfer functions, the vehicles are divided into 3 different groups. Taking advantage of the fact that the location of the mounts is shared by multiple vehicles of the same platform, 5 nominally identical vehicles for each sub-group are used. The set is formed as follows:

- BMW - U06 (2 Series Touring)
- BMW - F39 (X2)
- BMW - F45 (2 Series Touring - old version)

Since the vehicles considered belong to the same sub-category, they exhibit many similarities. However, they are not identical, and as seen above, even within a population of identical vehicles there is marked variability. It is therefore decided to first test whether or not, with respect to the SPL due to booming, the vehicles exhibit some measure of correlation.

This study is performed by means of a DOE analysis. Numerical models of the mounts are used to generate virtual vehicle designs. The dynamic stiffness parameters of the mounts in each individual direction are varied, using the previously identified nominal value as the central value. The allowable variation from the nominal stiffness value is $\pm 15\%$. This value is within the tolerances of these components.

A total of 300 different powertrain mounting system designs are generated. These are then combined with the transfer functions of the considered vehicles, for a total of 1500 vehicles, divided into 3 groups of 500 vehicles each.

As a comparison value between the different vehicles, a scalar quantity is defined representing the SPL between 20 ÷ 60Hz, i.e. where the booming phenomenon occurs with greater intensity. This quantity is defined, for each vehicle as:

$$SPLV = \sum_{p=20}^{60} SPL(\omega_p) \quad (35)$$

In this way it is possible to identify with a single value the performance of a vehicle. The results of the 5 vehicles of each group are added together, and a booming index is generated for each design, relative to each group.

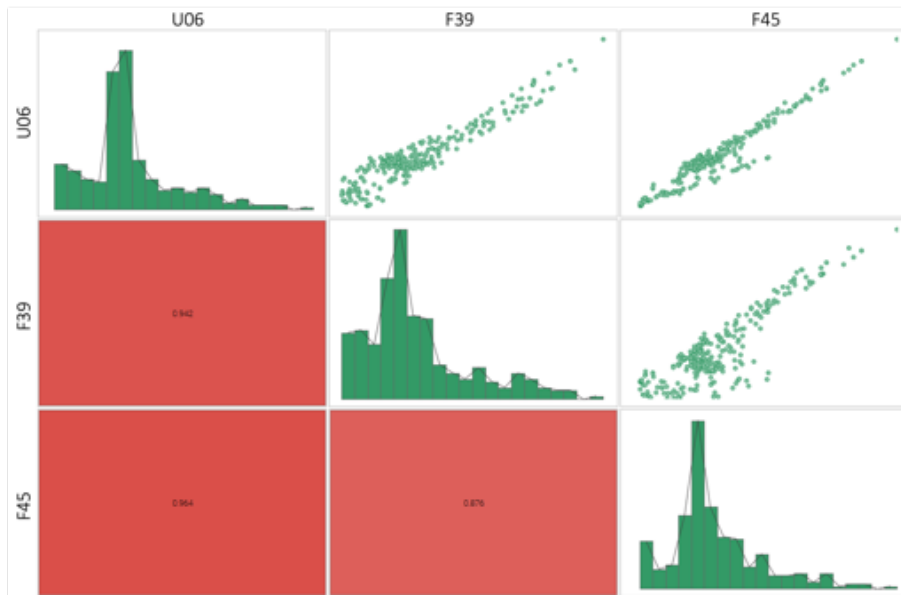


Figure 44: SPL correlation matrix of SPLs for the 3 groups of vehicles.

The results of the analysis are shown in graphical form in figure [44](#). For representation, a correlation matrix is used. In this graph, the correlation between the performance of vehicles in one group with that of vehicles belonging to the other two vehicle groups. It can be seen that although the vehicles are different, they are correlated with each other in terms of low frequency booming. This means, that each different PMS design used, results in a similar variation of the SPL in the three vehicle groups. Or in other words, the three vehicle groups react the same way to changes in the powertrain support system.

From this consideration, in order to streamline the computational operations, it is decided to focus on only one vehicle group, that of U06.

3.8.2 Optimization strategy

We then move on to a more detailed analysis of the vehicles belonging to the U06 group only.

Also in this case a DOE analysis is carried out first, with the aim of identifying possible correlations between the vehicles considered. In this case each vehicle is treated separately, and its booming index between $20 \div 60$ Hz is compared, utilizing the previously defined index *SPLV*, as in equation [35](#).

Again, 300 different designs are generated, similar to what was done previously.

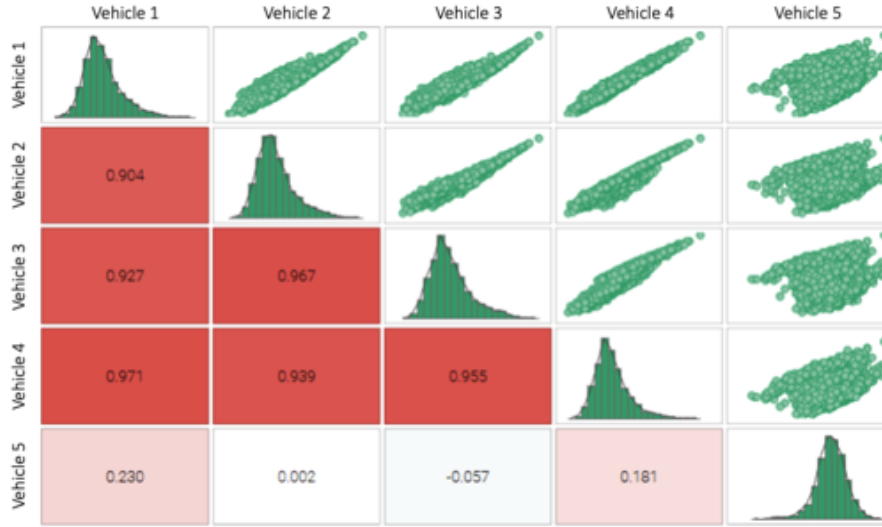


Figure 45: SPL correlation matrix for U06 vehicles.

In figure [45](#) the correlation of the booming noise performance among the 5 considered vehicles is then shown in graphical form. It can be seen, in this case with more detail, that the first four vehicles of the group present a linear correlation between them, regarding the SPL due to booming. This means that their sensitivity to the variation of the PMS is very similar. It can therefore be expected that by improving the SPL of one vehicle, the others will tend to benefit as well. The fifth vehicle, on the other hand, exhibits a more dispersed distribution, although with a linear base trend. It is believed that this fact is due to the type of vehicle considered. In this vehicle, in fact, there is an oversized battery placed under the bank of the rear seats. Although the geometries of the engine compartment and the rest of the body are identical. For this vehicle it cannot, a priori, be concluded that the performance variations of SPL follow those of the other 4 vehicles.

An optimization process is therefore defined for the vehicles of group U06.

The first objective of the optimization is to reduce the simulated SPL in the 5 vehicles considered. Second, we also want to take into account the variability of the elastomeric components. As reported in [2.3](#), the values of a mount can deviate $\pm 15\%$ from the predetermined nominal value. The combination of variability in transfer functions and transmitted forces can clearly lead to problems. Some vehicles

may have clearly superior acoustic qualities, while others may not meet the defined requirements.

Therefore, the individual dynamic stiffness values are allowed to vary around their mean value. This value is considered to be industrially applicable. Lower dynamic stiffness values would conflict with other functionalities, such as durability. With higher values, there would firstly be a problem with the vibrational comfort, the mounts would in fact isolate too little at low frequencies. Second, since the geometry of the mount housing is already defined, there would be problems with industrialization. Further stiffening a mount (more than 20% more) means adding elastomeric material. This is no longer possible in a trouble shooting phase.

In addition to the variability of the average dynamic stiffness value, a relative dispersion of the considered dynamic stiffness value is also defined. In this way the tolerance of the insulating elements is modeled. A Gaussian distribution of the dynamic stiffness around the considered values is then used. For each new dynamic stiffness value obtained, 100 values are generated.

The optimization problem can be defined as follows:

$$\text{Minimize } \begin{cases} \sum_i^n SPLV_i(v, k_j, \sigma_{k_j}) \\ \sum_i^n \sigma_{SPLV_i}(v, k_j, \sigma_{k_j}) \end{cases}$$

being:

$$\forall n \in V, \forall j \in M$$

with the following boundaries:

$$\begin{aligned} k_{lj} &\leq k_j \leq k_{uj} \\ \sigma_{lj} &\leq \sigma_j \leq \sigma_{uj} \end{aligned}$$

where:

- $SPLV_i$ is the SPL value for the i^{th} vehicle
- σ_{SPLV_i} is the standard deviation of the i^{th} vehicle's SPL
- n is the number of considered vehicles in the set set V
- k_j is the dynamic stiffness of the each mount's DoF, extracted from the set of available mounts M. Each dynamic stiffness is allowed to vary its mean value between the two boundaries k_{lj} and k_{uj} . These are fixed to $\pm 20\%$ of the nominal stiffness value.

3 POWERTRAIN MOUNTS CHARACTERIZATION

- σ_{k_j} is the standard deviation of the k_j dynamic stiffness. 100 gaussian distributed values, defined from the considered dynamic stiffness, are generated for each iteration with a spread of $\pm 15\%$.

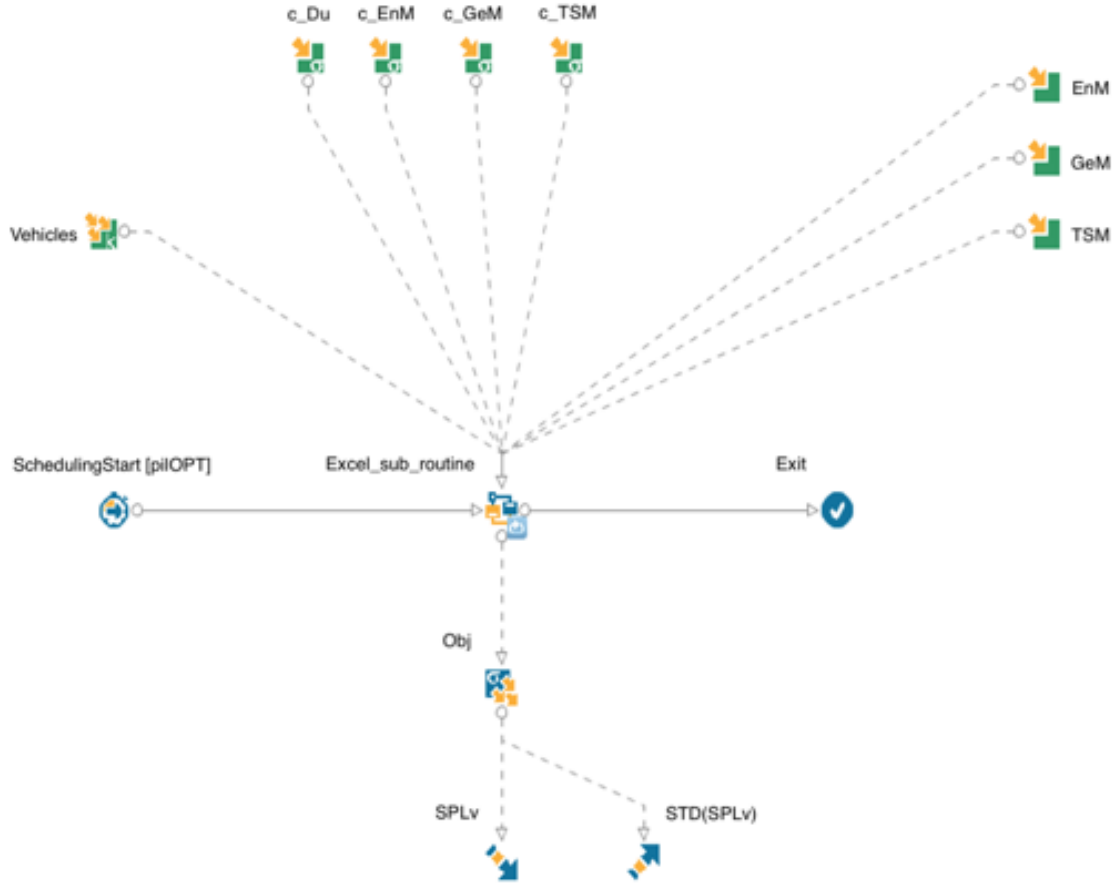


Figure 46: Optimization process scheme.

In figure 46 we see the flow diagram adopted for the optimization. For this phase modeFrontier software is used. The central node of the optimization is a spreadsheet fully programmed in excel. In the spreadsheet the calculations for the synthesis of the SPL are performed. The databases of response surfaces and NTF of the measured vehicles are also managed. Finally, the kinematic model used to extract the motor torque values is inserted. As can be seen, on the right side of the picture, the individual characterized mounts are selectable, different designs are then generated. At the top of the diagram, the parameters referring to the dynamic stiffnesses of the mounts are visible. The parameters that can be modified are therefore:

- c_{Du} : dynamic stiffness of the wishbone mount
- c_{EnM} : dynamic stiffness of the engine mount

3 POWERTRAIN MOUNTS CHARACTERIZATION

- c_{GeM} : dynamic stiffness of the gearbox mount
- c_{TSM} : dynamic stiffness of the torque strut mount

Each of these stiffnesses is defined by three parameters in turn, which identify the stiffness of each individual mount in its main directions. Thus, 12 parameters are modified simultaneously to define the dynamic stiffness of the powertrain mounting system.

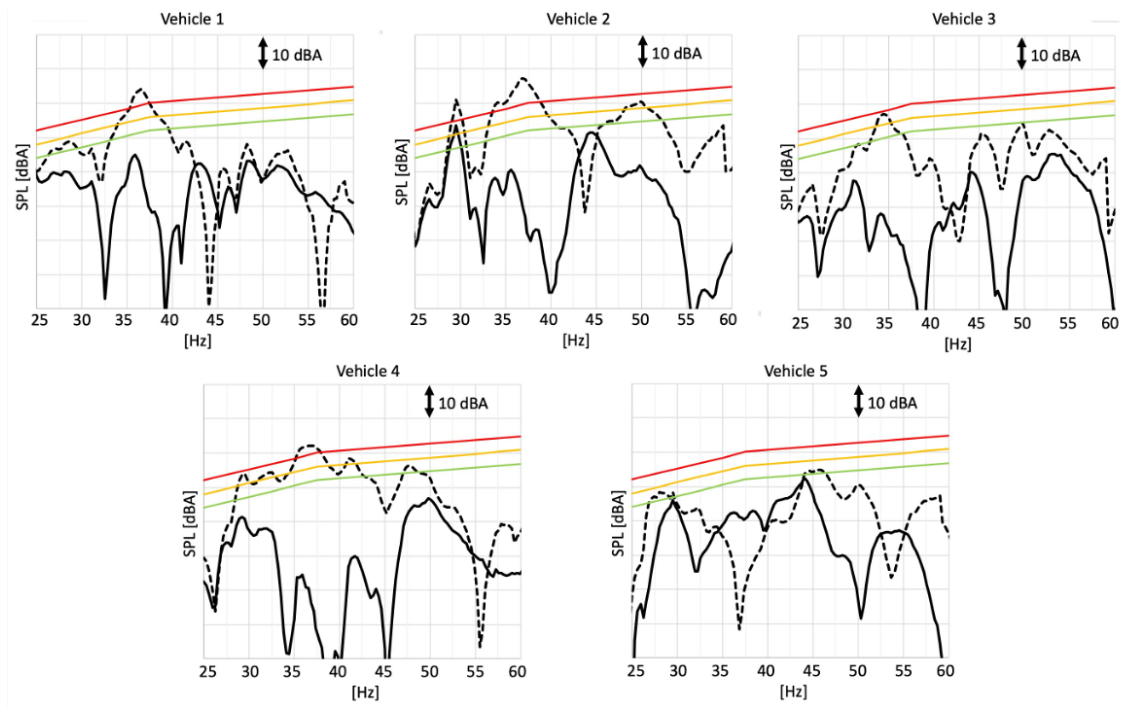


Figure 47: Result of optimization for each vehicle of the group studied in detail.
 — Baseline SPL value. The same baseline mounting configuration is used for all vehicles
 - - - Optimized SPL. The same optimized mounts are used for all vehicles.

The effect of the mount's optimization on the SPL of the considered vehicles can be verified. The results for each vehicle of the group are shown in figure 47 where the SPL obtained with a standard mount configuration (dashed line in the diagrams) and the SPL synthesized using the optimized mounts (solid line) is presented. The SPL derived from the structure borne noise, especially in the $25 \div 40$ Hz range, is considerably reduced in the first 4 vehicles considered. It is also noticeable how the booming at 37 Hz of the 4th vehicle is completely suppressed, while the reduction of booming at 50 Hz is less affected by the optimization (for all vehicles). In this region the behavior of the front sub-frame is less important. This area is in fact dominated by the compression of the fluid confined by the cabin, caused by the

3 POWERTRAIN MOUNTS CHARACTERIZATION

trunk and the windscreen, as visible in the modal analysis previously discussed. It is however possible, thanks to the mount modification, to obtain moderate improvements. The fifth vehicle, which has the lowest correlation with the others, has the lowest level of booming already with the non-optimized mounts. Optimization does not markedly improve the SPL of this vehicle, but it is not negatively affected either.

In conclusion, a sensitivity analysis is also performed, to identify which parameters have the greatest influence on the overall SPL, the study includes the coupled effects between the various parameters considered. The graphs shown in Figure [48](#).

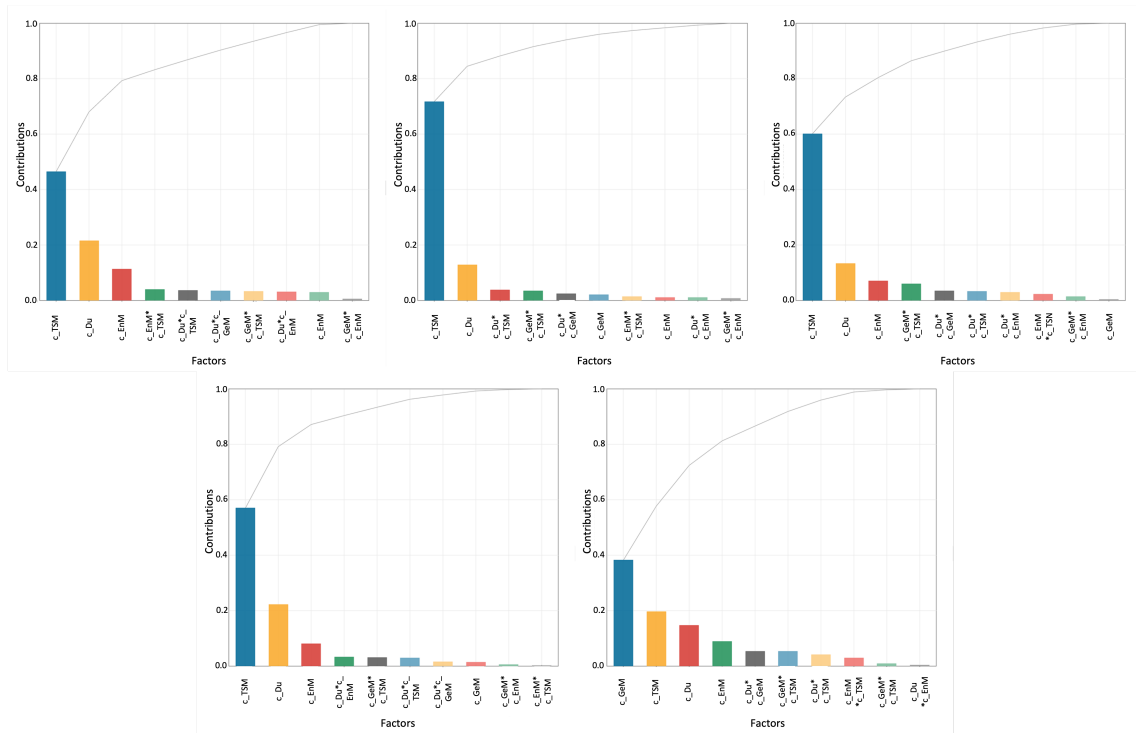


Figure 48: Results of sensitivity analysis for the five vehicles considered for optimization.

From the sensitivity analysis it can be seen that, for the first 4 vehicles, the most important parameters are the stiffness of the TSM and the wishbone mount, in different ratios. It is different for the fifth vehicle. In this case, the most important parameter is the stiffness of the GeM followed by that of the TSM.

4 Electric refrigerant compressor for air conditioning system

In this chapter, after having concluded the analysis of powertrain booming, the focus is on structural noise generated by electromechanical components in electric vehicles. Acoustics in conventional vehicles has always been dominated by the presence of the internal combustion engine. This fact, which certainly has negative aspects and often leads to problems, has the great advantage of masking the noise generated by other components, which would otherwise be present. This is the case, for example, with electromechanical components, such as the service box or the air conditioning system. The acoustics of the air conditioning system has always been important in itself, especially for the aero-acoustics issues. However, the structural noise during the operation of the vehicle did not usually present any criticality. As is well known, however, the HVAC system of an electric car, in addition to taking charge of the cooling and heating of the passenger compartment, has a function in electric vehicles that does not exist in traditional vehicles. In fact, the battery module must be heated in winter and cooled during charging cycles. Especially this second situation is of particular importance for the vehicle passengers.

Charging phases still occur more frequently than refueling in conventional vehicles, but above all they have a longer duration. The average duration for recharging a battery from 20 to 100% is about $3h$ when using traditional charging systems, [67]. At this stage, the refrigerant cycle compressor often runs at full speed to increase the efficiency of the operation. The component, which is attached directly to the chassis, or to an intermediate structure, is a major source of noise during this phase. For this reason, in this second part of the thesis, we focus on this component, the refrigerant compressor of the air conditioning unit.

For ACU systems in the automotive industry, the most used compressors are scroll type. These, as reported in the research work by [68] have superior performance to axial piston and rotary piston compressors, especially with respect to pressure pulsation effects. Also in the work of Ishii et al. [69], where a complete dynamic analysis of the compressor is performed, it is shown that the scroll compressor produces less vibration.

Compressors of this type are formed by two identical Archimedes spirals, a representation of the working principle can be seen in figure 49.

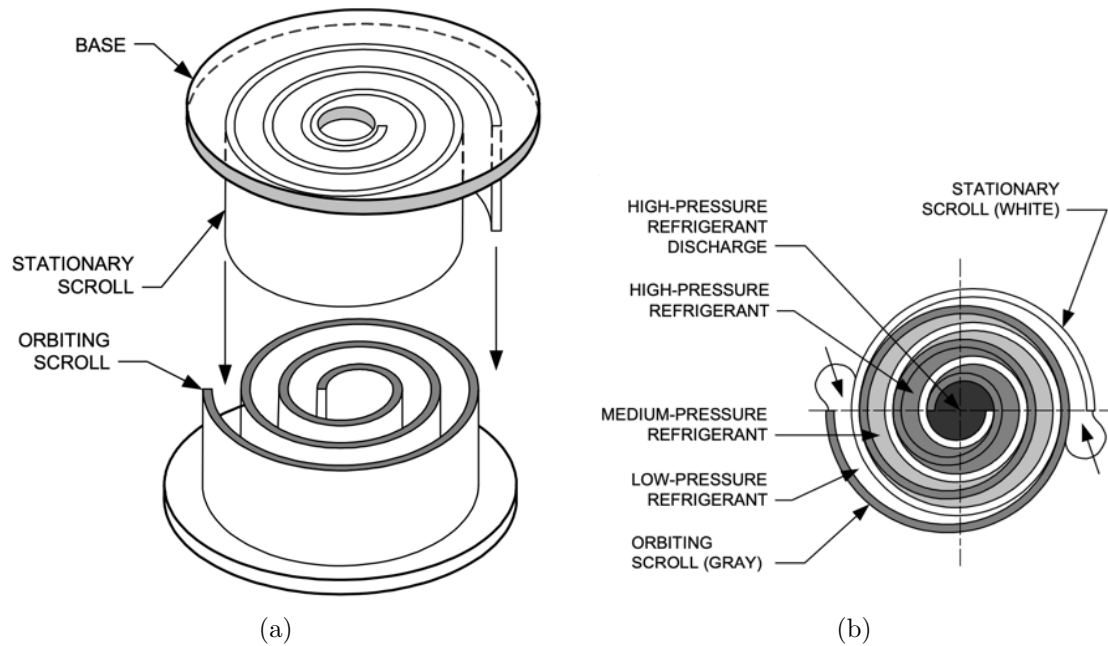


Figure 49: General representation of a scroll compressor [70]:

- a - The compression mechanism is formed by two identical scrolls. One is inverted and rotated 180° to intermesh with the opposite scroll
- b - The compression process is continuous, at any given time the scroll vanes contain pockets of low-, medium-, and high pressure refrigerant gas.

The study proposed in this section has two objectives. The first one is to identify, through "in-situ" measurements, the static and dynamic unbalance of the rotor. This analysis is used to identify the quality of the compressor, without having to use a dedicated component test-bench, measurements are made on the component mounted in the vehicle.

The starting point of this analysis is the determination of the inertance matrix of the compressor, mounted in the vehicle, using roving hammer impacts. Utilizing inversion techniques and virtual point transformation (similarly to what was previously done in [3.2.4]) the apparent mass matrix is determined. An extended discussion regarding this part of the analysis is presented in [4.3]. By combining, then, accelerations detected during operation, with the determined apparent mass, internal forces and unbalance characteristics are derived.

The second objective is to perform a complete synthesis of the SPL due to the dynamic excitations that the compressor transfers to the body. The synthesis is validated through in-vehicle SPL measurements under the same conditions. Unlike what was previously developed in the chapter [3], for this study the dynamic proper-

ties of the mounts are defined from component test bench measurements. The values thus obtained are used to define a complex dynamic stiffness model. Frequency and amplitude dependencies are modeled for both real and imaginary components, using a function to model the dynamic amplification factor.

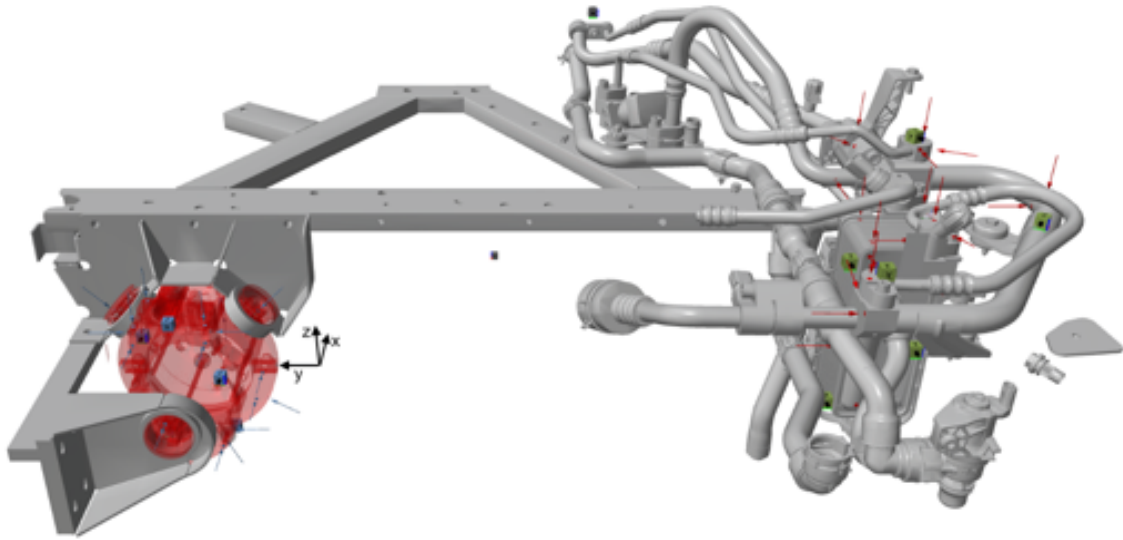


Figure 50: Representation of the system. The refrigerant compressor is highlighted in red. It is attached to the front chassis side utilizing a prototypal subframe. The mounting strategy is based on a single level of decoupling.

The system considered during this step can be seen in figure [50](#). On the left side the compressor can be seen, mounted using three rubber mounts identical to each other. The installation is prototypical, and is mainly used for compressor identification and structure isolation study. On the right side of the figure there are heat exchangers. The two components are connected by two pipes, a suction hose and a pressure hose. The two pipes are prototypical, and for this reason not included in the CAD drawing.

Similar to what was seen for the powertrain in the first part of the thesis, the compressor considered here also generates low frequency structural noise. The range considered is between $5Hz$ and $120Hz$. Also in this case, the major contribution of the excitations, come from the first order of rotation. Data acquisition is performed using an MKII system from Müller-BBM. The data are also preprocessed here. Since in fact we are only interested in excitations related to the first order of combustion, an order analysis according to internal standardize procedure is performed. This is done for all measured quantities, i.e. accelerations and forces. Using a tacho signal as reference for the analysis, the data are sampled at $16384Hz$, and processed with a resolution of $0.125Hz$.

4.1 Rotor unbalance

One of the qualities you want to control in a scroll compressor is the rotor imbalance. In fact, this is part of the specifications that are usually defined to the supplier. Therefore, in this section we will first define the quantities considered analytically, and then describe the estimation of the rotor unbalance through experimental measurements.

4.1.1 Scroll operational Excitation

Before proceeding with the experimental determination of the internal forces of the compressor, the quantities involved are defined analytically. These have their origin in rotor imbalances and forces resulting from gas compression. Also in this section, as in the whole compressor analysis, the quantities involved are considered at a virtual point (VP) coincident with the center of mass of the compressor.

The complex vector of acting forces and moments can be written as a function of frequency ω as:

$$\begin{Bmatrix} \vec{F}_{all,VP} \\ \vec{M}_{all,VP} \end{Bmatrix} = \begin{Bmatrix} \vec{u}_{stat,all,VP} \\ \vec{u}_{dyn,all,VP} \end{Bmatrix} \{w^2\} + \begin{Bmatrix} \vec{F}_{gas,VP} \\ \vec{M}_{gas,VP} \end{Bmatrix} \quad (36)$$

Without going into detail, and thus omitting the analytical derivation of all formulas, one can define the static and dynamic unbalances, in complex form, as:

$$\vec{u}_{stat,all,VP} = \sum_{i=1}^6 \vec{u}_{stat,i,VP} \quad , \quad \vec{u}_{dyn,all,VP} = \sum_{i=1}^6 \vec{u}_{dyn,i,VP} \quad (37)$$

where the static unbalance $\vec{u}_{stat,i,VP}$ depends on the position vector r_{VP} , which defines the distance between the principal axis, passing through the virtual point, and the unbalance. While the dynamic unbalance $\vec{u}_{dyn,i,VP}$ depends on $r_{VP}l$, thus defining an arm between the virtual point and the unbalancing mass.

For the definition of the term F_{Gas} , please refer to the work of Bin et al. [71], where a complete analytical derivation is done. Regarding the term M_{Gas} , on the other hand, are the moment resulting from gas compression. They can be derived as:

$$\vec{M}_{Gas} = \begin{Bmatrix} \underline{M}_{Gas} \\ 0 \\ 0 \end{Bmatrix}, \quad \underline{M}_{Gas} = M_{Gas} \cdot (\cos(\varphi) + i \sin(\varphi)) \quad (38)$$

4.2 Experimental estimation

In this section, starting from experimental measurements, the static and dynamic unbalances of the scroll compressor are identified. Since a dedicated test bench component is not available at the moment, the characterization of the component mounted in the car is carried out.

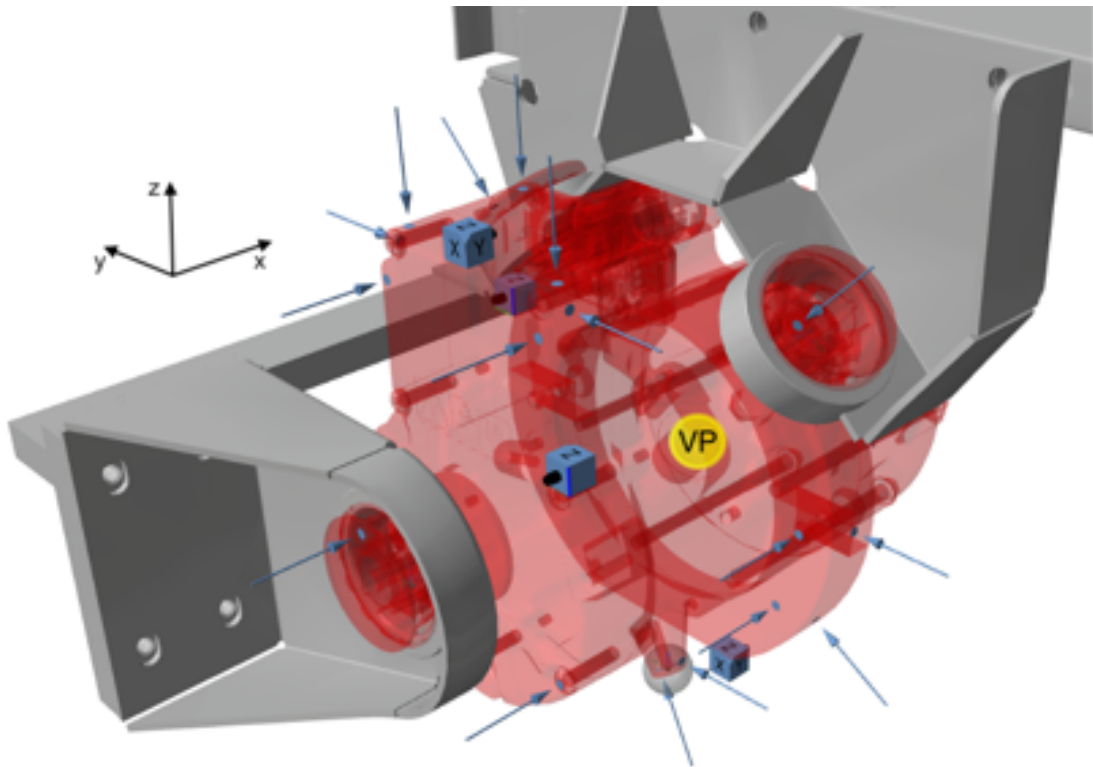


Figure 51: The compressor is excited with an instrumented hammer at the indicated points and directions. Accelerometers located on the compressor are also visible. At the center of the compressor, highlighted in red, the VP is defined, which coincides, in this case, with the compressor's center of mass.

To proceed to the experimental determination of F_{All} , as defined in equation [36](#),

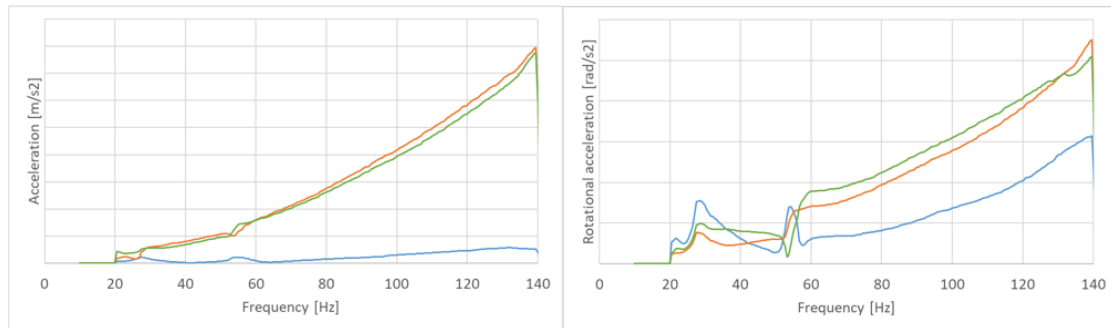
4 ELECTRIC REFRIGERANT COMPRESSOR FOR AIR CONDITIONING SYSTEM

one must use the accelerations measured during operation and the so-called apparent mass matrix, which is obtained by inversion of the compressor inertance matrix. This inverse technique, already described by Mas et al. [72], is used when force sensors cannot be inserted between source and receiver.

Also for the compressor, as was done for the powertrain, the virtual point technique is used. In this case, a virtual point (VP) is used, which coincides with the center of mass of the compressor itself. Since the derivation is identical to what was previously described in chapter 3.2, this is not described again. The transformation is carried out for all 6 DoFs that characterize the rigid-body motion of the assembled compressor.

Accelerations are acquired during several load cycles of the compressor, which is made to operate. Sweep cycles are mainly used, in which both the compressor speed and the delivery pressure are varied. For comparison, a sweep is used between 7.5 and 13.5bar of compression, and compressor rotating speed varying between 1000 and 9000rpm.

The compressor moves as a rigid body during these measurements, and its kinematics are summarized in the VP. The 6 acceleration components for this point can be seen in figure 52.



(a) Accelerations in the VP: —acceleration in x direction; —acceleration in y direction; —acceleration in z direction;
 (b) Rotational accelerations in the VP: —Rotational acceleration around the x axis; —Rotational acceleration around the y axis. —Rotational acceleration around the z axis.

Figure 52: Rigid body motion of the compressor under sweep operating conditions synthesized in the compressor VP.

Before proceeding with the synthesis, however, a parenthesis must be opened regarding the determination of the apparent mass matrix.

4.3 Derivation of the system's matrices

To continue with the derivation of the rotating unbalance forces, we proceed with the derivation of the mass and dynamic stiffness matrices at the virtual point considered.

4.3.1 Derivation of the mass matrix

The mass matrix for a reference point can be derived simply from the dynamic's second law, and the momentum theorem. Two points in a rigid body are considered, a virtual point VP and a mounting point i . By equilibrating forces in the body, it can be determined that $\vec{F}_{VP} = \vec{F}_i$ holds. The first thing to consider is the center of gravity theorem at the mounting point. Thus, a relationship between force and acceleration at point i is established.

$$\vec{F}_i = [M] \cdot \vec{a}_i$$

The acceleration \vec{a}_i is considered as unknown. On the contrary, the acceleration and the force at the reference point are known. The acceleration at the mounting point can be described by the reference point acceleration assuming that the location vector \vec{r}_i (location vector from reference point to mounting point) is known. Inserting the relative acceleration description and $\vec{F}_{VP} = \vec{F}_i$ yields

$$\vec{F}_{VP} = [M] \cdot (\vec{a}_{VP} + \vec{\omega}_{VP} \times \vec{r}_i) = [M] \cdot (\vec{a}_{VP} + [\tilde{r}_i]^T \vec{\omega}_{VP}) = [M] \vec{a}_{VP} + [M][\tilde{r}_i]^T \vec{\omega}_{VP}, \quad (39)$$

where $[\tilde{r}_i]$ is the cross product matrix of the location vector \vec{r}_i .

Using the torque equilibrium about point VP , the relationship between torque, acceleration and angular acceleration at the reference point can be established.

$$\vec{M}_{VP} = \vec{F}_i \times \vec{r}_i = [\tilde{r}_i] \vec{F}_i = [\tilde{r}_i] ([M] \vec{a}_{VP} + [M][\tilde{r}_i]^T \vec{\omega}_{VP}) = [\tilde{r}_i][M] \vec{a}_{VP} + [\tilde{r}_i][M][\tilde{r}_i]^T \vec{\omega}_{VP} \quad (40)$$

The equations [39](#) and [40](#) can be combined in matrix notation. This results in the mass and inertia moment matrix .

$$\begin{Bmatrix} \vec{F}_{VP} \\ \vec{M}_{VP} \end{Bmatrix} = \underbrace{\begin{bmatrix} [M] & [M][\tilde{r}_i]^T \\ [\tilde{r}_i][M] & [\tilde{r}_i][M][\tilde{r}_i]^T + [I] \end{bmatrix}}_{\text{Mass and inertia moment matrix}} \begin{Bmatrix} \vec{a}_{VP} \\ \vec{\omega}_{VP} \end{Bmatrix} \quad (41)$$

The element with index 2, 2 in the mass and inertia moment matrix corresponds including the Huygens-Steiner part of the moment of inertia, therefore the inertia tensor $[I]$ must be added additionally.

4.3.2 Derivation of the stiffness matrix

The stiffness matrix is derived analogously to the mass and inertia moment matrix. The general spring equation is used as a starting point:

$$\vec{F}_i = [K] \cdot \vec{s}_i.$$

In this case, the force at the virtual point VP, is also identical to the force at the connection point, $\vec{F}_{VP} = \vec{F}_i$. The position vectors \vec{s}_i and \vec{s}_{VP} describe the position of the mounting and virtual point, respectively, relative to the initial position after the force excitation. Analogous to accelerations, the location vector \vec{s}_i can be described by the vectors \vec{s}_{VP} and \vec{r}_i . After inserting this relation, the equation is rewritten.

$$\vec{F}_{VP} = [K] \cdot (\vec{s}_{VP} + \vec{\varphi}_{VP} \times \vec{r}_i) = [K] \cdot (\vec{s}_{VP} + [\tilde{r}_i]^T \vec{\varphi}_{VP}) = [K] \vec{s}_{VP} + [K][\tilde{r}_i]^T \vec{\varphi}_{VP} \quad (42)$$

The torque equilibrium is used here exactly as above. Thus, the torque at the reference point can be represented as a function of (\vec{s}_{VP} and $\vec{\varphi}_{VP}$)

$$\vec{M}_{VP} = \vec{F}_i \times \vec{r}_i = [\tilde{r}_i] \vec{F}_i = [\tilde{r}_i] ([K] \vec{s}_{VP} + [K][\tilde{r}_i]^T \vec{\varphi}_{VP}) = [\tilde{r}_i][K] \vec{s}_{VP} + [\tilde{r}_i][K][\tilde{r}_i]^T \vec{\varphi}_{VP} \quad (43)$$

The equations [42](#) and [43](#) can be combined in matrix notation to define the stiffness matrix as:

$$\begin{Bmatrix} \vec{F}_{VP} \\ \vec{M}_{VP} \end{Bmatrix} = \underbrace{\begin{bmatrix} [K] & [K][\tilde{r}_i]^T \\ [\tilde{r}_i][K] & [\tilde{r}_i][K][\tilde{r}_i]^T \end{bmatrix}}_{\text{Stiffness Matrix}} \begin{Bmatrix} \vec{s}_{VP} \\ \vec{\varphi}_{VP} \end{Bmatrix} \quad (44)$$

4.3.3 Apparent Mass matrix

Apparent mass is one of the possible ways to represent an FRF matrix. The most common representations of FRFs are given in tabular form, as described by Ewins [\[64\]](#), in table [9](#).

4 ELECTRIC REFRIGERANT COMPRESSOR FOR AIR CONDITIONING SYSTEM

Response Parameter R	Standard $\frac{R}{F}$	Inverse $\frac{F}{R}$
R = x	Receptance Admittance Compliance Dynamic flexibility	Dynamic Stiffness
R = \dot{x}	Mobility	Mechanical impedance
R = \ddot{x}	Inertance Accelerance	Apparent mass

Table 9: FRFs definitions

The classical form of the FRF is the receptance, the ratio between a displacement (amplitude) and the excitation force. The Apparent Mass describes the relationship between the excitation force and acceleration. Its inverse is called the inertance. The definition of apparent mass comes from the general equation of motion for an oscillator with external excitation force.

$$M\ddot{x} + C\dot{x} + Kx = F_a \quad (45)$$

The excitation force F_a can be expressed in the form $F_a(t) = Fe^{j\omega t}$. Thus, the solution to the equation of motion is of the form $x(t) = Xe^{j\omega t}$. The associated velocity and acceleration can be easily derived. They are defined as $\dot{x} = j\omega Xe^{j\omega t}$ and $\ddot{x} = -\omega^2 Xe^{j\omega t}$, respectively. After inserting these quantities, the equation [45](#) can be simplified.

$$-M\omega^2 Xe^{j\omega t} + Cj\omega Xe^{j\omega t} + KXe^{j\omega t} = Fe^{j\omega t} \quad (46)$$

$$-M\omega^2 X + Cj\omega X + KX = F \quad (47)$$

$$\underbrace{-\omega^2 X}_{\text{acceleration term}} \left(M + \frac{Cj}{\omega} + \frac{K}{-\omega^2} \right) = F \quad (48)$$

The term $(-\omega^2)X$ (acceleration) is factored out so that the force/acceleration ratio can be formed. After the ratio is formed, the remaining terms are summarized and from this the Apparent Mass AM is formed. The 2 resulting terms correspond to a (real) mass M and a complex frequency dependent stiffness $\underline{K}(\omega)$, where the real

part is a stiffness and the imaginary part is a damping.

$$AM = \frac{F}{-\omega^2 X} = M + \frac{Cj}{\omega} + \frac{K}{-\omega^2} \quad (49)$$

$$= M + \frac{-Cj\omega + K}{-\omega^2} \quad (50)$$

$$= M + \frac{K(\omega)}{-\omega^2} \quad (51)$$

4.4 Experimental Derivation of the Apparent Mass

Experimental derivation of the apparent mass matrix is performed on the system visible in [50]. The compressor is excited using 18 excitation points, using an instrumented hammer, from PCB (model 086D05) with a measurement range of $\pm 22240 Npk$ and a sensitivity of $0.23 \frac{mV}{N}$. Accelerations are recorded with 6 triaxial accelerometers from PCB (356A series), with a usable frequency range of $2 \div 5000$ Hz and a sensitivity of $10.2 \frac{mV}{s^2}$. This results in an overdetermined system, which allows synthesis at virtual point VP , as previously defined. The transformation is performed, in this case, using the post processor included in the acquisition system, Dirac (from Vibes Technology). The virtual point transformation operation using this technique is described in the work of Van der Seijs [5], and later also used by Häussler [60].

A 6x6 dimension inertance matrix is then obtained, in which the dynamic acting forces and the acting responses are synthesized at the virtual point. This point named VP, chosen coincident with the compressor's center of mass, but not coincident with the elastic center of the system. The system of mounts used, and their positioning, in fact, do not generate an elastic center within the structure. Thus, coupled effects are obtained in the inertance matrix, in which linear forces applied along one direction produce rotations of the virtual point, resulting in a non-diagonal matrix.

The situation is like that represented in figure [53], where in matrix form (and qualitative) are reported excitations and responses. It can be seen that off-diagonal elements are present. The apparent mass matrix is obtained by inversion of this matrix.

All this brings to the situation visible in figure [53]. Here, in a qualitative way, the relationship between the response of the 6 DoFs and a unit excitation applied to a single DoF is shown. For example, if an excitation applied to Tx is taken into account, it can be seen that the system is not decoupled. In an ideal case, a pure excitation along the x direction, should produce an acceleration of the body in the x direction only, without generating other accelerations. In this case, only the first

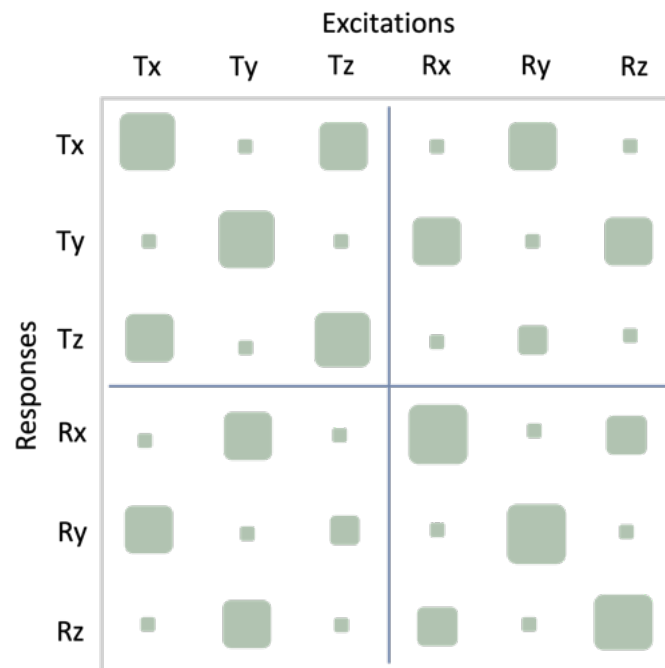


Figure 53: Inertance Matrix for the electric compressor measured in-situ for the 6DoF of the virtual point-VP. The squares in the figure represent the response of each individual degree of freedom, to a unit excitation in each of them

term of the first row of the matrix would be populated. Since through the mounting system EC is not coincident with the center of mass, coupled phenomena exist, thus the measured inertance matrix is not diagonal.

Since we have a general description of the system, refer to the sections, [4.3.1](#), [4.3.2](#) and [4.3.3](#), it is possible to compare numerical with experimental data obtained both at the inertance matrix level and its inverse. Where clearly the latter derived from the numerical system is not affected by noise, or measurement error, and are therefore treatable as reference value.

The mass and stiffness matrices are determined from given initial values, which are defined by suppliers or from CAD data. It is therefore possible, through modal analysis and modal superposition to calculate the response of the system, at the virtual point. Analogous to what is done experimentally.

The actual dynamic stiffness values of the mounts in their three main directions are not available in this case. And since it is decided to identify the system by in-situ measurements, it is not possible to place load cells to determine the desired values. Therefore, the quasi-static stiffness values are used as starting values to define the dynamic stiffnesses. These are defined through analytical functions, hyperbolic in character, which model both the stiffening factor and the amplitude dependence. These are defined as follows:

$$[K] = \underline{v}(\omega, s) \cdot [K_{EC}], \quad s = |\underline{s}(\omega)| \quad (52)$$

where $[K_{EC}]$ is the stiffness matrix of each mount in its elastic center (EC), refer to section [2.3.2](#). This matrix is described as purely diagonal. In real and imaginary terms it can be written as:

$$\underline{v}(\omega, s) = \Re(\underline{v}(\omega, s)) + i\Im(\underline{v}(\omega, s)) \quad (53)$$

The functions adopted to model the dependence are of hyperbolic type, and are combined together as follows, with respect to both their real and imaginary components.

$$\Re(\underline{v}(\omega, s)) = v_{rel} \left(\Re(v_{f\infty}) - \frac{1}{\Re(m_\omega)\omega + \Re(\omega_0)} \right) \left(\Re(v_{s\infty}) + \frac{1}{\Re(m_s)s + \Re(s_0)} \right) \quad (54)$$

4 ELECTRIC REFRIGERANT COMPRESSOR FOR AIR CONDITIONING SYSTEM

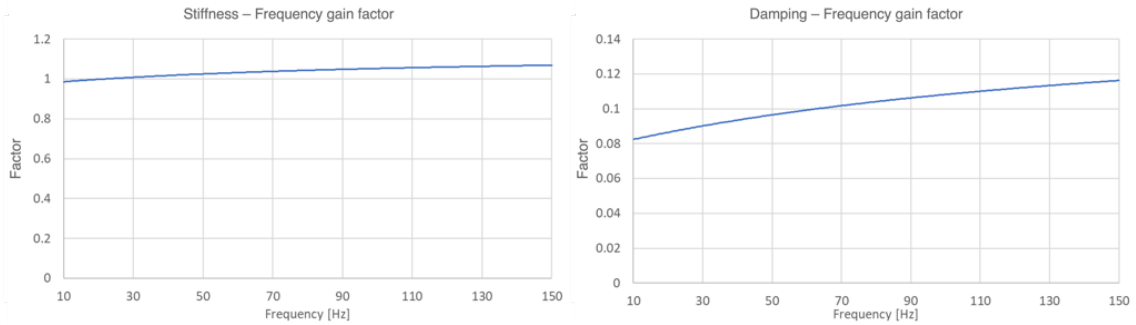
$$\mathfrak{I}(\underline{v}(\omega, s)) = v_{rel} \left(\mathfrak{I}(v_{f\infty}) - \frac{1}{\mathfrak{I}(m_\omega)\omega + \mathfrak{I}(\omega_0)} \right) \left(\mathfrak{I}(v_{s\infty}) + \frac{1}{m_{\mathfrak{I}(s)}s + \mathfrak{I}(s_0)} \right) \quad (55)$$

If it is decided to consider only the frequency dependence, leaving out the amplitude dependence, the functions reduce to:

$$\Re(\underline{v}(\omega)) = v_{rel} \left(\Re(v_{\omega\infty}) - \frac{1}{\Re(m_\omega)\omega + \Re(\omega_0)} \right) \quad (56)$$

$$\mathfrak{I}(\underline{v}(\omega)) = v_{rel} \left(\mathfrak{I}(v_{\omega\infty}) - \frac{1}{\mathfrak{I}(m_\omega)\omega + \mathfrak{I}(\omega_0)} \right) \quad (57)$$

Where the values of $v_{\omega\infty}$ and $v_{s\infty}$ are parameters used to define the asymptotic limits of the defined functions.



(a) Dynamic stiffness gain factor over frequency (b) Damping gain factor over frequency

Figure 54: Dynamic stiffness and damping gain factors - analytically defined.

Having then defined the dynamic stiffness, the assembly of the analytical system can be proceeded with. The equation of the system with damping, subjected to harmonic excitation, can be written, in the frequency domain, as:

$$[M]\{\ddot{x}(t)\} + [C]\{\dot{x}(t)\} + ([K] + i[D])\{x(t)\} = \{f(t)\} \quad (58)$$

or

$$(-\omega^2[M] + i\omega[C] + [K] + i[D]) \cdot \{\underline{s}(\omega)\} = \{\underline{f}(\omega)\} \quad (59)$$

with stiffness-proportional damping and the complex dynamic gain factor $\underline{v} =$

$\underline{v}(\omega, s)$ and with $[C] \sim [K]$, $[D] \sim [K]$ results in:

$$i\omega[C] + [K] + i[D] = \underline{v}[K_c] \quad (60)$$

where $[K_c]$ is the complex dynamic stiffness matrix. The simplified equation of motion can be written as:

$$(-\omega^2[M] + \underline{v}[K_c]) \cdot \{\underline{s}(\omega)\} = \{\underline{f}(\omega)\} \quad (61)$$

switching to modal coordinates, results in:

$$[\Psi]^T (-\omega^2[M] + \underline{v}[K_c]) [\Psi] \cdot [\Psi]\{\underline{s}(\omega)\} = [\Psi]\{\underline{f}(\omega)\} \quad (62)$$

resolved according to the modal shift

$$[\Psi]\{\underline{s}(\omega)\} = \left([\Psi]^T (-\omega^2[M] + \underline{v}[K_c]) [\Psi]\right)^{-1} [\Psi]\{\underline{f}(\omega)\} \quad (63)$$

with the diagonalisation characteristic of the eigenvector matrix

$$[\Psi]\{\underline{s}(\omega)\} = \left[-\omega^2 \left[\backslash m_{r\backslash}\right] + \underline{v} \left[\backslash k_{r\backslash}\right]\right]^{-1} \cdot [\Psi]\{\underline{f}(\omega)\} \quad (64)$$

with retransformation into physical coordinates

$$\{\underline{s}(\omega)\} = [\Psi]^{-1} \left[-\omega^2 \left[\backslash m_{r\backslash}\right] + \underline{v} \left[\backslash k_{r\backslash}\right]\right]^{-1} [\Psi] \cdot \{\underline{f}(\omega)\} \quad (65)$$

$$\{\underline{s}(\omega)\} = [\Psi]^{-1} \left[\backslash S(\omega)\backslash\right] [\Psi] \cdot \{\underline{f}(\omega)\}, \quad \left[\backslash S(\omega)\backslash\right] = \left[-\omega^2 \left[\backslash m_{r\backslash}\right] + \underline{v} \left[\backslash k_{r\backslash}\right]\right]^{-1} \quad (66)$$

It is then possible at this point, thanks to the modal superposition, to calculate the forced response of the system.

To simplify the calculation, the diagonal of the matrices $\left[\backslash m_{r\backslash}\right]$ and $\left[\backslash k_{r\backslash}\right]$ are extracted and put into vector form.

$$\{m_r\} = \begin{Bmatrix} m_1 \\ m_2 \\ \vdots \\ m_6 \end{Bmatrix}, \quad \{k_r\} = \begin{Bmatrix} k_1 \\ k_2 \\ \vdots \\ k_6 \end{Bmatrix} \quad (67)$$

With the standard functions:

$$\{\underline{S}_r\} = \begin{Bmatrix} \underline{S}_1 \\ \underline{S}_2 \\ \vdots \\ \underline{S}_6 \end{Bmatrix}, \quad \underline{S}_r = \frac{1}{\underline{v} k_r - \omega^2 m_r}, \quad \underline{S}_r = \frac{1}{(\Re(\underline{v}) + i\Im(\underline{v})) k_r - \omega^2 m_r} \quad (68)$$

as Real- and Imaginary components

$$\Re(\underline{S}_r) = \frac{\Re(\underline{v}) k_r - \omega^2 m_r}{(\Re(\underline{v}) k_r - \omega^2 m_r)^2 + (\Im(\underline{v}) k_r)^2}, \quad \Im(\underline{S}_r) = \frac{-\Im(\underline{v}) k_r}{(\Re(\underline{v}) k_r - \omega^2 m_r)^2 + (\Im(\underline{v}) k_r)^2} \quad (69)$$

Thus the sum representation for the displacements results in:

$$\underline{s}_i(\omega) = \sum_{r=1}^6 \sum_{k=1}^6 \psi_{ri} \psi_{rk} \cdot \underline{S}_r(\omega) \cdot \underline{f}_k(\omega) \quad (70)$$

or

$$\underline{s}_i(\omega) = \sum_{r=1}^6 \psi_{ri} \cdot \underline{S}_r(\omega) \cdot \sum_{k=1}^6 \psi_{rk} \cdot \underline{f}_k(\omega) \quad (71)$$

Displacement by force and mode superposition Summary with element-wise vector multiplication \odot :

$$\{\underline{s}(\omega)\} = \Psi(\{\underline{S}(\omega)\}) \odot \Psi^T\{\underline{f}(\omega)\} \quad (72)$$

simplified with

$$\{\underline{Y}(\omega)\} = \Psi^T\{\underline{f}(\omega)\} \quad (73)$$

$$\{\underline{s}(\omega)\} = [\Psi](\{\underline{S}(\omega)\} \odot \{\underline{Y}(\omega)\}) \quad (74)$$

$$\Re\{\underline{s}(\omega)\} = [\Psi] \left(\Re(\{\underline{S}(\omega)\}) \odot \Re(\{\underline{Y}(\omega)\}) - \Im(\{\underline{S}(\omega)\}) \odot \Im(\{\underline{Y}(\omega)\}) \right)$$

$$\Im\{\underline{s}(\omega)\} = [\Psi] \left(\Re(\{\underline{S}(\omega)\}) \odot \Im(\{\underline{Y}(\omega)\}) + \Re(\{\underline{S}(\omega)\}) \odot \Im(\{\underline{Y}(\omega)\}) \right) \quad (75)$$

Thus, having now the system fully described, the FRFs generated, can be inverted, obtaining the apparent mass matrix.

As mentioned, the system matrices used to build the analytical model contain uncertainties. These are not numerical in origin, but arise from the accuracy of the initial data. Recall, in this regard, the variability of the elastomeric components, as described in [2.3](#). Other parameters, such as mass, geometric coordinates and inertia matrix, are derived from CAD data. Also these parameters may have tolerances, which are not known in the prototype configuration considered. Experimental measurements of the compressor, can then be used to verify the accuracy of the data used. Parameters are then defined, which are optimized to fit, simultaneously, both the FRFs of the inertance matrix and its inverse, based on experimental data.

The determination of mass properties of rigid bodies from experimental measurements was a very popular research topic towards the end of the last century. Methodologies for determining the properties of rigid bodies from measurements have been developed, showing excellent results. A very interesting work that allows accurate results using direct solutions was presented by Fregolent and Sestieri [\[73\]](#). In the work of Vahid et al. [\[74\]](#), the determination of the mass properties of an engine using in-situ derived FRFs is proposed.

All parameters considered are allowed to vary, within limits deemed physical, so that the solutions remain applicable, small deviations from the nominal values are therefore allowed.

It is therefore started from the following values, determined through data received from suppliers and determined from CAD data:

	Coordinates [mm]			Rotation[°]			Static Stiffness[N/mm]		
	x	y	z	Rx	Ry	Rz	Axial	Radial_1	Radial_2
Mount 1	-143.41	0.10	8.16	0	0	180	23	13	13
Mount 2	-14.83	-67.94	76.49	0	45	90	23	13	13
Mount 3	-14.84	67.09	76.49	0	135	90	23	13	13

Table 10: Initial values

4 ELECTRIC REFRIGERANT COMPRESSOR FOR AIR CONDITIONING SYSTEM

The General Reduced Gradient (GRD) algorithm [75] is used for parameter optimization. Two frequency ranges are defined, one in which rigid compressor modes occur ($10 - 30Hz$) and a high frequency range free of resonances ($100 \div 150Hz$). The parameters defined are then modified so that the error between the numerically generated and measured FRF is minimized. This, both for the inertance matrix, and for its inverse.

The parameters used are:

- Position of each mount - allowed to vary within $\pm 12.5mm$ from the nominal value
- Rotation of each mount - allowed to rotate of 5° from the nominal value
- Static stiffness - allowed to vary within $0.25 \frac{N}{mm}$ from the nominal value
- Moments of inertia- allowed to vary of about $300kgm^2$
- Products of inertia - allowed to vary within $\pm 2.5kgm^2$
- Coordinates of the CoG - allowed to vary within $\pm 3mm$ from the initial values
- Total mass - allowed to vary within $\pm 0.5kg$

The parameters defining the dynamic stiffness factor, and amplitude dependence as described in equation [56] and in [57] are also optimized.

The values following optimization are given in tabular form [11].

	Coordinates [mm]			Rotation[$^\circ$]			Static Stiffness[N/mm]		
	x	y	z	Rx	Ry	Rz	Axial	Radial_1	Radial_2
Mount 1	-155.92	3.750	19.98	-4.9	-4.9	185	29.9	10.8	12.2
Mount 2	-19.44	-67.495	77.98	2.5	43.3	87.5	29.7	12.9	11.8
Mount 3	-8.46	73.576	82.34	2.2	131.5	89.4	29.2	10.6	10.3

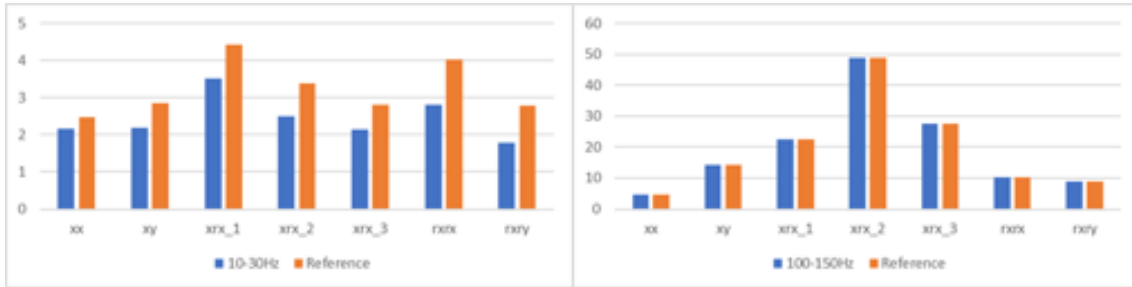
Table 11: Optimized Values

The mass value, not reported in the table, is increased from 6,8 kg to a value of 7,2 kg, which is still considered realistic.

First, the eigenvectors obtained analytically and the experimental ones are compared, considering the results separately, for the two frequency ranges above defined. In figure [55a] the comparison for the range where rigid modes occur can be seen. Already in this diagram, differences between the reference and simulated values can be observed. In figure [55b] the same diagram is proposed, using in this case, values

4 ELECTRIC REFRIGERANT COMPRESSOR FOR AIR CONDITIONING SYSTEM

in the frequency range $100 \div 150$ Hz. Already from this representation it is recognized how, when no more rigid modes occur, the analytical model and experimental measurements have better superposition.



(a) Frequency range $10 \div 30$ Hz

(b) Frequency range $100 \div 150$ Hz

Figure 55: Comparison of compressor eigenvectors, obtained analytically and experimentally.

It has been said that when dealing with matrix inversion, one often runs into ill-conditioning problems. One parameter to check, therefore, is the condition number of the matrix that is being inverted. Figure 56 shows the condition number over frequency. It can be seen that the matrix is poorly conditioned, and therefore more sensitive to any measurement errors at low frequencies, more specifically up to 50 Hz. This fits with what previously observed. The experimental FRFs of the apparent mass matrix, especially in the low-frequency range, show deviations from the analytical ones.

The condition number, then, decreases to values close to 450 starting at 50 Hz and then remains constant. As noted earlier, the comparison between experimental and analytical FRFs is very satisfactory in the frequency range $100 \div 150$ Hz. It can therefore be deduced that the conditioning of the matrix, for values above 50 Hz, is sufficient to effect its inversion without running into errors that dominate the solutions.

The optimization gives very good results regarding the frequency range in which no more rigid body modes occur. It is certainly more interesting to concentrate on the range between $10 \div 30$ Hz, i.e. where the 6 rigid body modes do occur. In this part in fact the dynamic stiffness and damping parameters play a predominant role, while at higher frequencies the mass matrix does.

Therefore, the comparisons between simulated and experimental FRFs for the frequency range $100 \div 150$ Hz are not reported in graphical form.

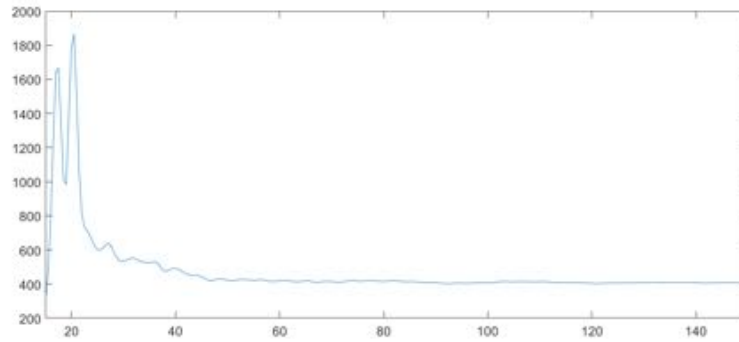


Figure 56: Condition number of the inertia matrix as function of frequency.

The first comparison presented concerns the FRFs related to the R_i-R_i terms, as defined in figure 53, these are the terms R_x-R_x , R_y-R_y and R_z-R_z . It can be observed in figure 57 how in this case, the results of the analytical model have an excellent correlation with the values determined through experimental measurements. Both with regard to the FRFs of the inertia matrix (visible in real component in figure 57a and imaginary in figure 57c), and with regard to the same FRFs of the apparent mass matrix (visible in real component in figure 57b and imaginary in figure 57d).

4 ELECTRIC REFRIGERANT COMPRESSOR FOR AIR CONDITIONING SYSTEM

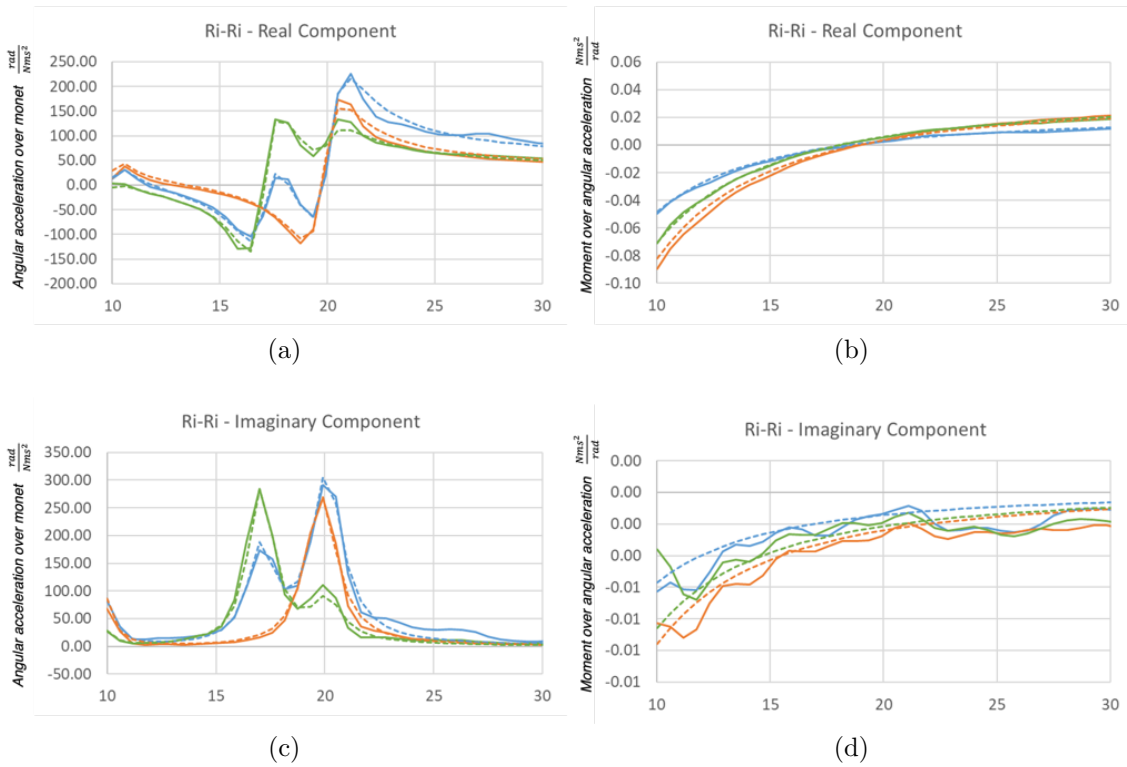


Figure 57: Comparison of the simulated (---) and experimentally determined FRFs (—), both in the inertance and apparent mass FRF Matrix
 Rx-Rx — blue; Ry-Ry — orange; Rz-Rz — green

The second case presented, regards the Ti-Ti FRFs, is visible in figure 58. These are identified by Tx-Tx, Ty-Ty and Tz-Tz, with reference to the nomenclature used in the figure 53. Again, it can be seen that the FRF-level comparison of the inertance matrix remains very good. Also with respect to their inverse, the comparison between FRF of inertance and apparent mass is still satisfactory. More in detail, the comparison between the FRFs of the inertance matrix (visible in real component in figure 59a and imaginary in figure 59c) are in line with what we have seen previously. As for the FRFs of the apparent mass matrix, the real values (visible in figure 59b) are very satisfactory. Differently, the imaginary components of the same FRFs (visible in figure 59d) show discrepancies. The share values of matrix elements influence the matrix condition number. Specific submatrices have elements of different order of magnitude. This matter, combined with the matrix inversion and the apparent mass FRF-calculation leads to different result quality.

4 ELECTRIC REFRIGERANT COMPRESSOR FOR AIR CONDITIONING SYSTEM

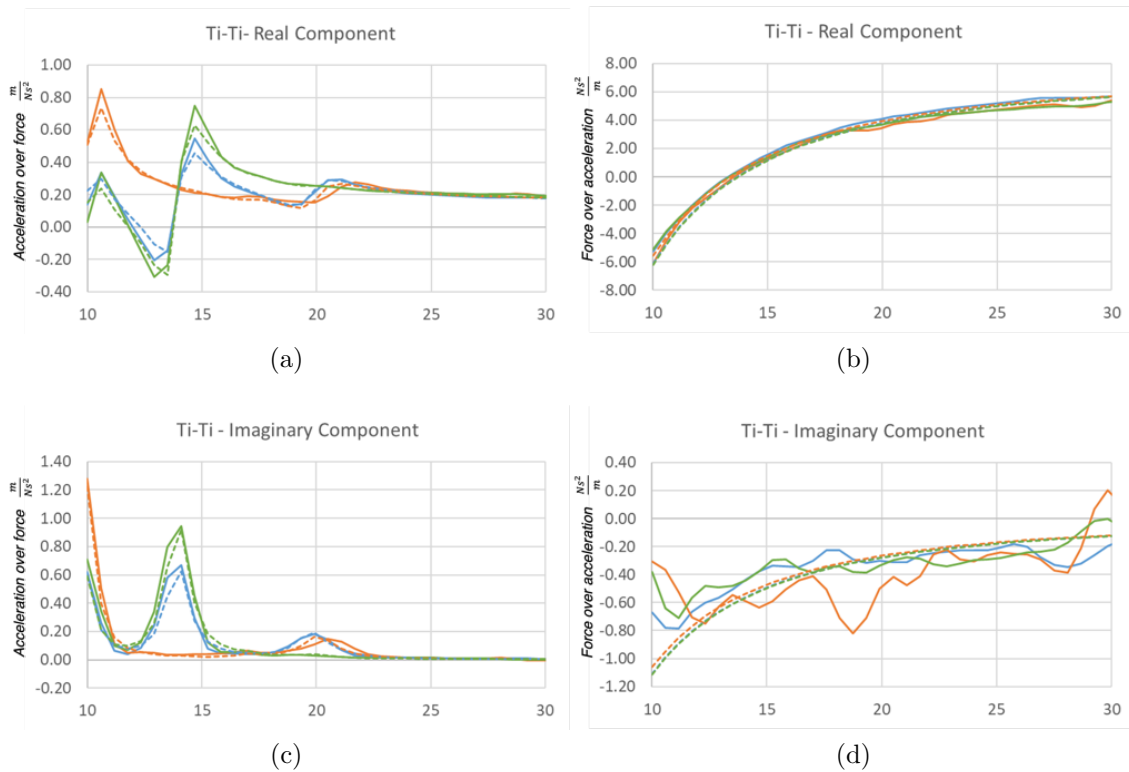


Figure 58: Comparison of the simulated (---) and experimentally determined FRFs (—), both in the inertia and apparent mass FRF Matrix
 Tx-Tx —; Ty-Ty —; Tz-Tz —

The last case presented concerns the off-diagonal terms, in the sub-matrix T_i-T_j . These are the elements, which with reference to the nomenclature used in the figure 53, are identified as T_x-T_y , T_x-T_z and T_y-T_z . As with the previous graphs, we compare analytically and experimentally determined FRFs. Unlike the FRFs that identify the main diagonal of the two matrices considered, the results visible in fig. 59 are not of equal quality. It can be seen that the FRFs of the inertia matrix (both the real components in fig. 59a, and the imaginary components in fig. 59c) present a very good correlation. In contrast, the same FRFs in the apparent mass matrix exhibit very poor correlation (both the real components in fig. 59b, and the imaginary components in fig. 59d). This result is caused by the conditioning number of the inertia matrix. Measurement errors are amplified and do not allow obtaining reliable values for these FRFs.

4 ELECTRIC REFRIGERANT COMPRESSOR FOR AIR CONDITIONING SYSTEM

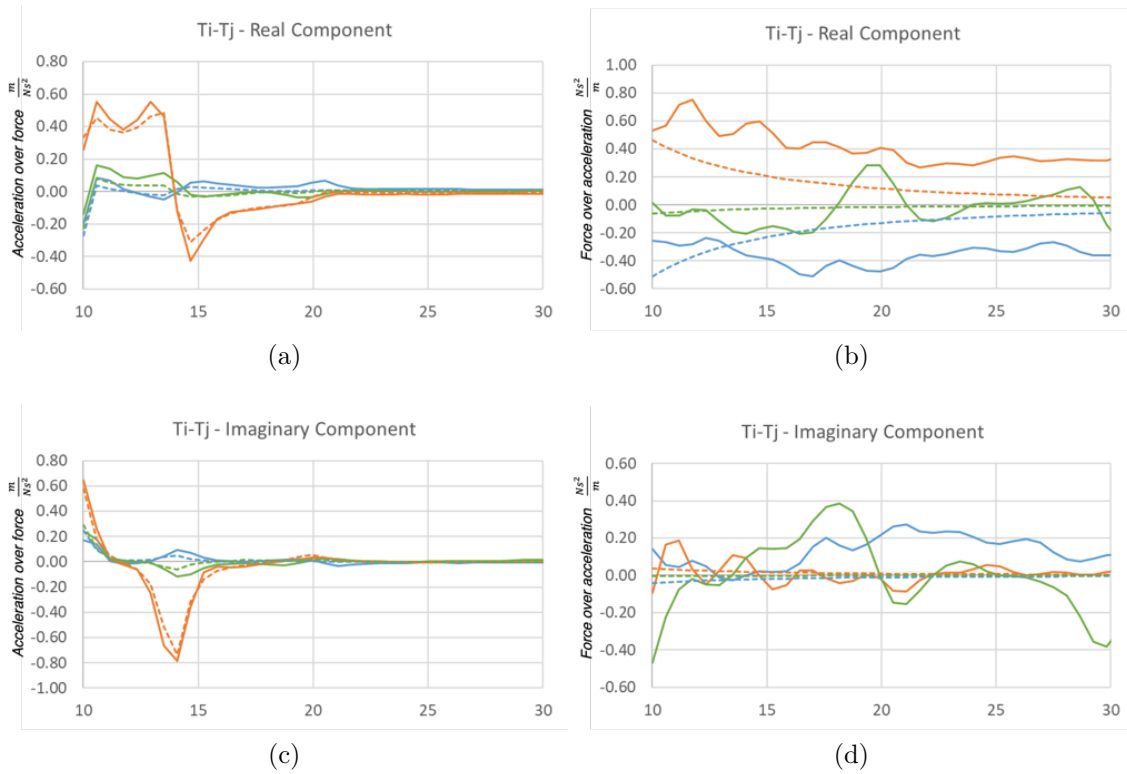


Figure 59: Comparison of the simulated (---) and experimentally determined FRFs (—), both in the inertia and apparent mass FRF Matrix
 Tx-Ty —; Tx-Tz —; Ty-Tz —

From what is presented in the diagrams above, it can be said that regarding the inertia matrix, the analytical models and the experimental data present a very good correlation. On the other hand, with respect to the apparent mass matrix, it can be observed that the elements of the main diagonal (named Ti-Ti and Ri-Ri), do not present criticalities in the inversion. Other components not belonging to the main diagonal, however, are subject to inversion errors. These, due to the condition number of the inertia matrix, do not allow to obtain a stable inversion.

4.4.1 Experimental Results

After having experimentally determined the apparent mass matrix, one can proceed with the experimental identification of the compressor's rotating unbalance characteristics. These are obtained precisely by multiplying the matrix just identified with the compressor accelerations, measured during operation.

The system can be identified under three different conditions, represented schematically in figure [60](#). Since no information is available with respect to the dynamic

characteristics of the hoses, the inertance matrix is identified without the supply and return lines attached, as shown in figure [60a](#). On the other hand, the accelerations of the compressor in operation are identified in two configurations. In the standard configuration, visible in figure [60b](#), normal piping is used. Then there is a third configuration, in which the hoses are replaced, as depicted in figure [60c](#). In this last case, much longer and more flexible pipes, on which masses are mounted, are used. By doing so, the structural noise transmission channels, which pass through the pipes, are cut off.

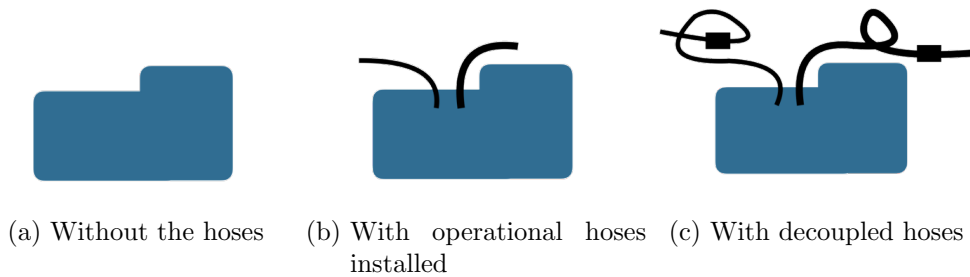
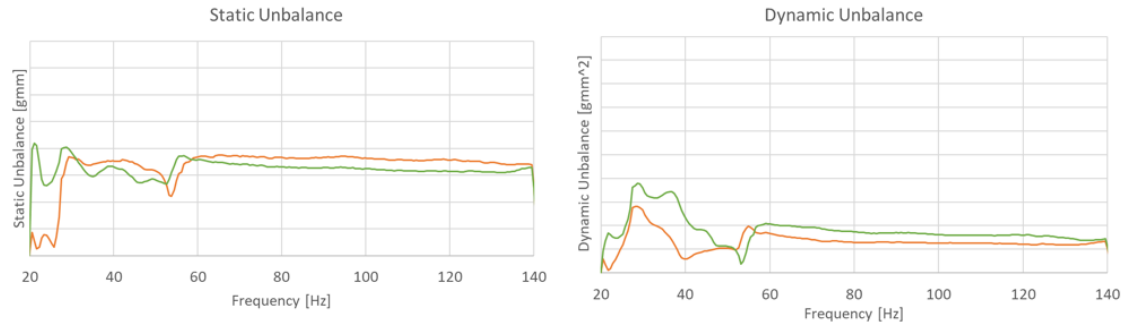


Figure 60: Configurations in which compressor characteristics can be identified.

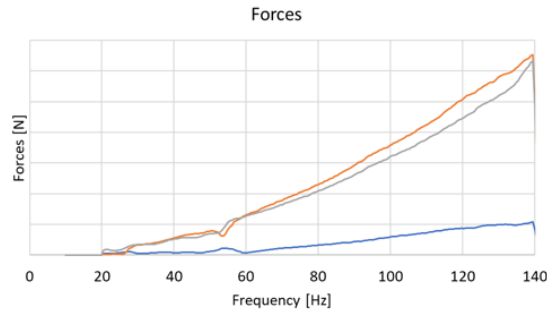
Obviously, using the apparent mass data of the compressor without hoses corresponds to a distortion, since the component cannot be put into operation. However, this study allows to isolate the influence of the piping on the dynamic behavior of the compressor. Moreover, the identification of the system with the hoses would not be able to capture the contribution of the latter to the total system behavior.

In Figure [61a](#), measurements are used in which the contribution of the piping has been isolated. It is first noticed that, in the frequency range between $20 \div 50$ Hz, the influence of the rigid modes of the mounted compressor coupled with a bad condition number, disturbs the evaluation of the rotor unbalance. This phenomenon is especially observable in figure [61a](#), where the static unbalance is graphed. In this graph, the two degrees of freedom in y and z are visible. Since the rotation axis is coincident with the x -axis, the two curves must lie above each other. The result is satisfactory, and the value remains constant with frequency. In figure [61b](#) the dynamic rotating imbalance values are shown, where similarly to what has just been said, the low frequency range is disturbed by the presence of the rigid compressor modes. Finally, in figure [61c](#), the dynamic forces developed by the compressor are visible. It can be seen that the forces due to the rotating unbalance are dominant. Also seen here in blue is the force due to gas compression, and it can be seen that it is, in the first line negligible compared to the rotating unbalance forces.

4 ELECTRIC REFRIGERANT COMPRESSOR FOR AIR CONDITIONING SYSTEM



- (a) Static Unbalance: — Unbalance evaluated utilizing the DoF in y direction. — Unbalance evaluated utilizing the DoF in z direction.
- (b) Dynamic Unbalance: — Unbalance evaluated utilizing the DoF in y direction. — Unbalance evaluated utilizing the DoF in z direction.

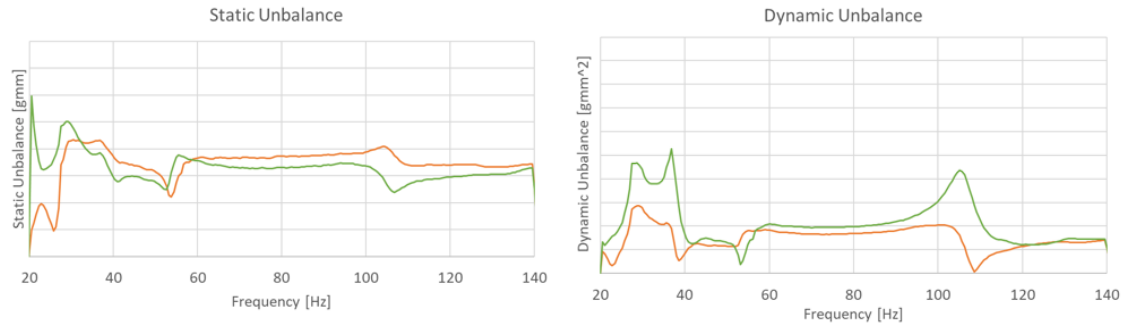


- (c) Dynamic forces: — Rotating unbalance force evaluated using the y DoF. — Rotating unbalance forces evaluated using the z DoF. — Gas forces in x direction.

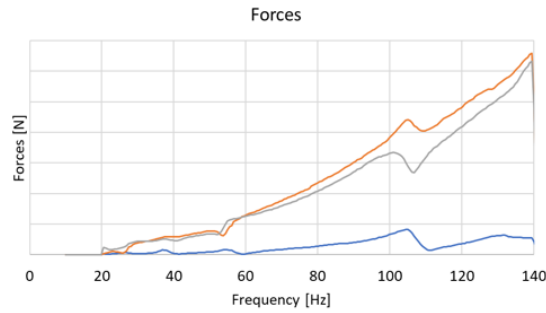
Figure 61: Evaluation based on experimental data of compressor characteristics. Measurement made without hoses mounted on the compressor.

The same analysis is now carried out, however, by connecting the suction and discharge hoses to the compressor. It can be observed, how also in this case, the range between 20 and 50 Hz is disturbed by the rigid body modes of the compressor mounted in its mounts. However, an additional problem occurs in this case. In all figures, but especially in figure 62a, at 100 Hz the curves are no longer constant. What is seen depicted is the influence of flexible piping. The same phenomenon was identified in the work of Tim et al. [7]. In their work it is seen that among the different structural noise paths, those represented by the pipes are, in this case even the dominant ones.

4 ELECTRIC REFRIGERANT COMPRESSOR FOR AIR CONDITIONING SYSTEM



- (a) Static Unbalance: — Unbalance evaluated utilizing the DoF in y direction. — Unbalance evaluated utilizing the DoF in z direction.
- (b) Dynamic Unbalance: — Unbalance evaluated utilizing the DoF in y direction. — Unbalance evaluated utilizing the DoF in z direction.



- (c) Dynamic forces: — Rotating unbalance force evaluated using the y DoF. — Rotating unbalance forces evaluated using the z DoF. — Gas forces in x direction.

Figure 62: Evaluation based on experimental data of compressor characteristics. Measurement made without hoses mounted on the compressor.

The in situ approach used allows to identify the rotor unbalance characteristics of the compressor. It is also possible to isolate the contribution of the flexible pipes, which, in this configuration, is not negligible for frequencies higher than 100 Hz.

4.5 SPL Synthesis

The following step is the synthesis of the generated low frequency booming noise. The goal, again, is to synthesize the sound pressure level at the driver's ear. Everything that has been previously described regarding the TPA analysis so far is still valid. However, in this case, not having a dedicated test bench, the TPA technique is used, refer to [2.4.2](#). The component is then identified and characterized only in its

assembled state and cannot be transferred to other designs. Similarly to what was done for the analysis of the rotor imbalance and internal forces, the contribution of the hoses is also isolated here. For the SPL synthesis as well two different configurations are considered. In one case the structural noise paths through the hoses are left active, in the second case they are blocked, refer to [60b](#) and [60c](#). Regarding the determination of the dynamic forces transferred by the mounts, these are determined by analytical models of the mount stiffnesses. Since the supports cannot be characterized during the measurements, a different approach is taken in this case.

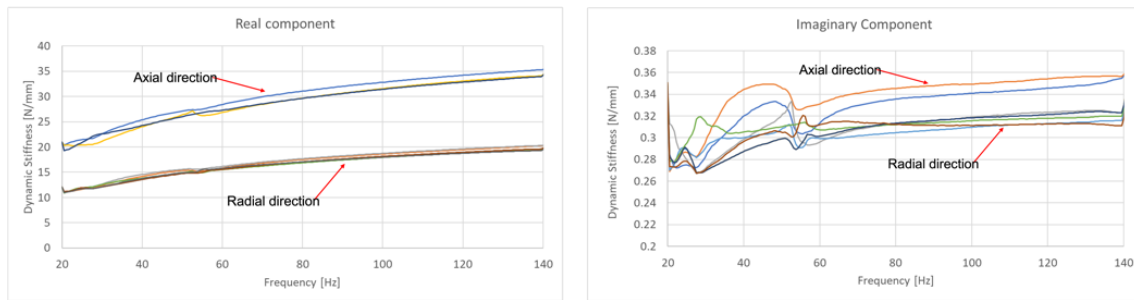
4.5.1 Dynamic stiffness - Compressor's mounts

Differently from what was done during the analysis of powertrain mounts, a test bench for detecting blocked forces is not available here, and it is therefore impossible to characterize the dynamic stiffnesses of the DoFs of each mount. The two alternatives are, to use inverse techniques or to rely on experimental measurements. For the compressor mounts, static stiffness values are available in the three main directions, the axial and the two radial. The supports are in this case radially symmetrical and identical to each other.

To determine the dynamic forces transferred through the supports, an analytical dynamic stiffness model, previously described in [4.4](#), is used. With what has just been described, and starting from the available static stiffness values, dynamic stiffness and damping, expressed as an imaginary component of stiffness are obtained. The latter, expressed as a function of frequency, can be seen in figure [63](#).

The mechano-acoustic noise transfer functions are detected by removing the compressor from its housing, as can be seen in figure [64](#). The presence of the compressor in fact makes it impossible to excite every connection point between component and support with the desired precision. Since the structure used cannot generally be considered rigid up to 140 Hz, every one of its components must be treated separately. It can be seen in the figure how the locations are highlighted with different colors. Therefore, 3 triaxial accelerometers are used for each mount position. Each of these are also excited in an overdetermined way using hammer impacts in all directions, which are also visible in the figure.

4 ELECTRIC REFRIGERANT COMPRESSOR FOR AIR CONDITIONING SYSTEM



(a) Dynamic stiffness - Real Component

(b) Dynamic stiffness - Imaginary Component

Figure 63: Dynamic stiffness modeling

4.5.2 Noise Transfer Functions

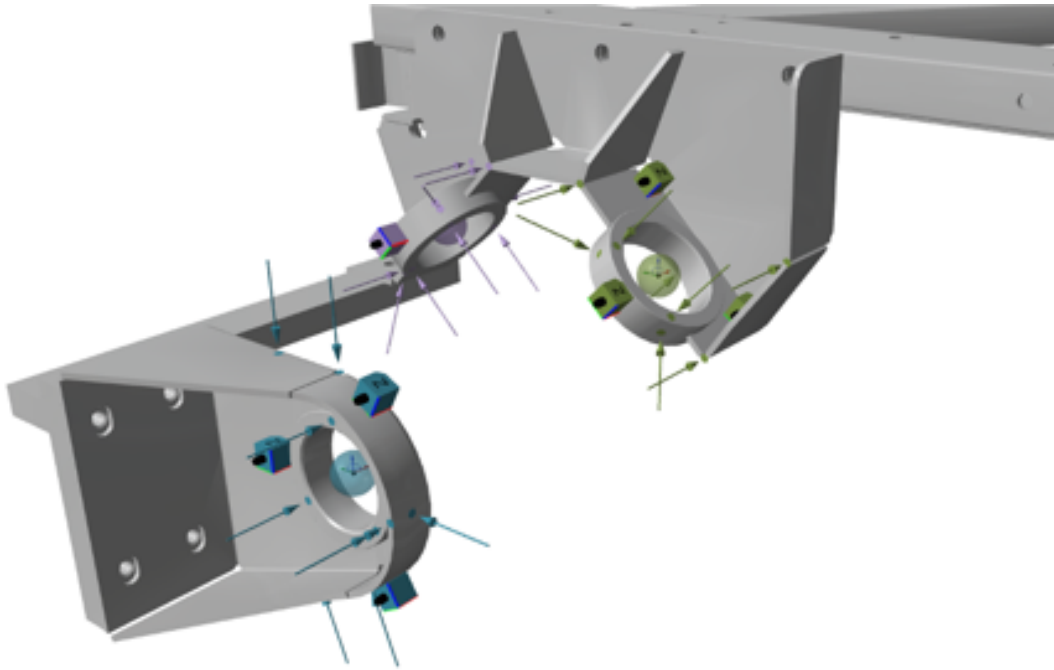


Figure 64: Measurement campaign for the acquisition of the noise transfer functions from the compressor holder to the driver's ears.

In addition, it can be seen in figure [64](#), how for each point the NTFs are concentrated in a VP. This coincides, as previously described, with the elastic center of each mount. The transformation of NTFs to a virtual point is treated by Van der Seijs in his doctoral thesis [5](#). It is based in general on geometric transformations analogous to those described in [3.2](#). For each of the points, NTFs are then obtained by considering 6DoFs of the virtual point.

4 ELECTRIC REFRIGERANT COMPRESSOR FOR AIR CONDITIONING SYSTEM

Using then the classical TPA, the dynamic forces transferred from each mount to the structure, in each degree of freedom, is multiplied with the corresponding NTF. As described in [2.4.2](#)

The first comparison is made by isolating the contribution of flexible piping to the SPL. This is done using data from measurements in which the pipe paths are drastically reduced by adding mass to the pipes. The kinematic analysis of the compressor is then performed using this data, and the corresponding dynamic forces transmitted by the individual mounts are then determined. The synthesized SPL is compared to the SPL directly measured by microphones placed in the driver's ear during the same measurement. The results are between 20 ÷ 140 Hz, which is the range considered so far. Only in the range between 25 and 35 Hz, the simulated results deviate from the measured ones. The cause of this phenomenon is due to the presence of rigid compressor modes, which occur precisely in this frequency band. However, the synthesis shows an accuracy in line with that desired for the remaining frequency range.

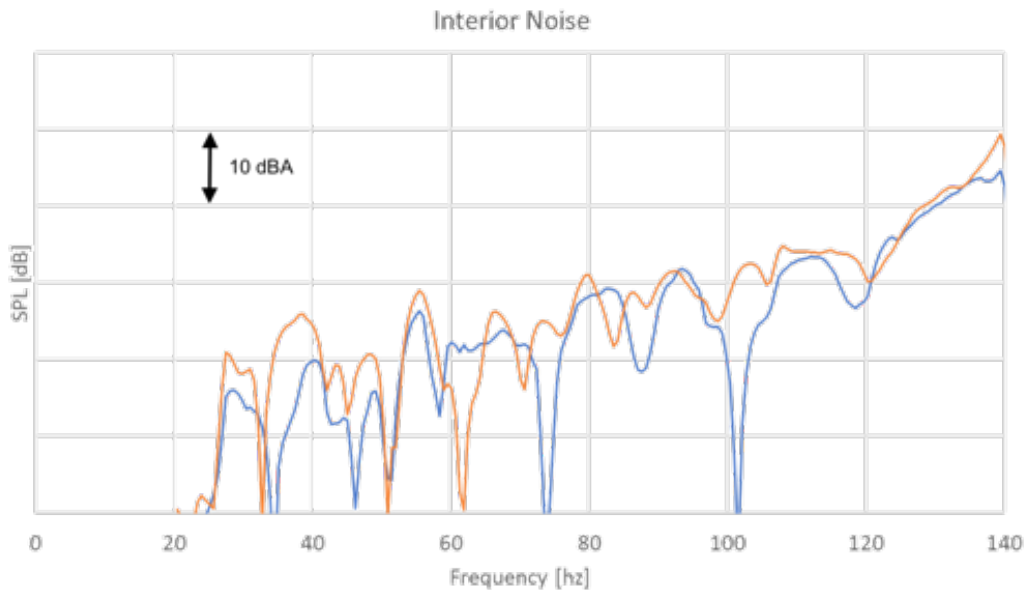


Figure 65: Comparison of the synthesized and simulated driver-perceived SPL without considering the flexible hoses influence
— Measured SPL
— Synthesized SPL

It is now intended to verify the contribution of the hoses to the SPL resulting from the compressor. To do so, the SPL previously synthesized, i.e. without the contribution of flexible hoses, is compared with the experimentally measured SPL

in vehicle, as visible in figure [66](#).

It can be seen that at low frequencies, i.e. up to 80 Hz, the contribution of the hoses is not apparent. For frequencies between 90 ÷ 140 Hz, the contribution of the hoses leads to an increase in SPL between 5 and 10 dBA. It can be seen that the hoses have a considerable contribution to the structural noise generated by the compressor. The latter derives from the dynamic stiffness of the hoses themselves and influences in a not negligible way the SPL after 80 Hz.

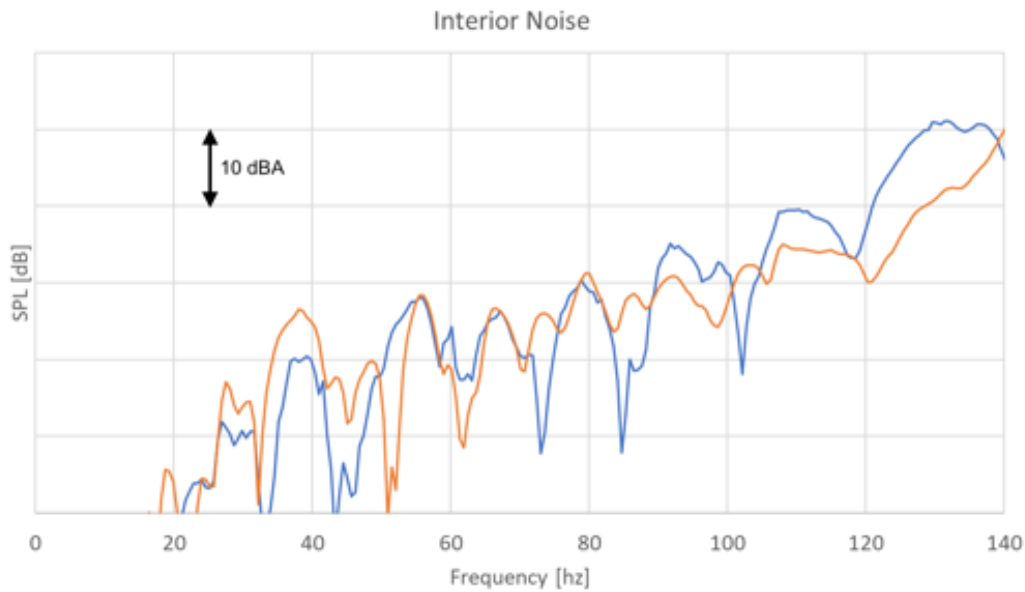


Figure 66: Comparison of the synthesized and simulated driver-perceived SPL considering the flexible hoses influence

- Measured SPL including the flexible hoses' contribution SPL
- Synthesized SPL not including the flexible hoses' contribution to SPL

SPL synthesis due to coolant compressor booming, provides excellent results. The proposed modeling of the mounts, and the in situ analysis of the component allow the production of reliable synthetic SPLs. It must be pointed out, however, that the contribution of the hoses is not modeled, and that this, as shown, is not negligible.

If it is already difficult to obtain information about the dynamic stiffness of mounts, as previously described, it is even more so for that of flexible pipes.

These elements are composed of layers of different materials, resulting in a global dynamic stiffness that can hardly be obtained by analytical functions. A very extensive work on this topic can be found in Sentpali's doctoral thesis [\[76\]](#). Here, functions are defined to deal with certain geometries; however, damping modeling

is not addressed.

There are also still limitations when it comes to the experimental determination of the dynamic properties of flexible pipes. Very often these are only determined in one direction. In the work of Johnston et al. [77] only the axial dynamic stiffness is characterized by experimental tests. Other experimental evidence for the characterization of flexible hoses can be found in the doctoral dissertation by Hölke [78]. Where the pressure dependence and the volume of the transported fluid are studied as a function of frequency.

However, it is not possible nowadays to completely model the dynamic behavior of a flexible hose.

5 Conclusions

In this work the focus was on low frequency structural noise, more specifically booming, perceived in the vehicle. The objective behind the research was to better understand the phenomenon, and at the same time generate tools and methodologies to be able to improve the vibro-acoustic quality of vehicles. In the first part of the thesis, the problem of low-frequency structural noise was described in general, and the methodologies used for its analysis and simulation were also described.

The rubber mount characterization was described in detail, comparing our findings with recent and current research results focused on the dynamic stiffness of these components. The analysis has been extended to the components' variability. Both rubber mounts' and complete vehicle's variability have been addressed with regard to the acoustic performance.

In the most general case the dynamic stiffness of the mounts is described by a 12x12 frequency dependent matrix. For the studied application, thanks to the frequency band of interest, to the inertia characteristics of the mounted components and to the decoupling between source and receiver, it is possible to concentrate the dynamic of the mounts in a single virtual point. In these conditions the condensed 6x6 matrix is further reduced, neglecting the 3 rotational effects. The virtual point transformation relies on geometrical relations between the physical description of the mount and the position of the selected VP. In order to synthesis the SPL at the driver's ear position, TPA methodologies are used, those implies matrix inversion techniques. This operation is influenced by the matrix element's order of magnitude and the deriving condition number. To overcome this problem experimental overdetermined matrices have been used.

All these technologies combined, have been used to tackle two problems: one on the booming deriving from the powertrain in internal combustion engine vehicles and the other on the booming from the coolant compressor in electric vehicles.

The industrial outcome of the mentioned merged are the following methodologies:

1. **Mounts' dynamic stiffness characterization procedure and tool:** given a new mount, it is possible to measure all its dynamic properties as function of static preload, frequency and amplitude of the excitation. The developed testing procedure relies on a dedicated test bench in which the mounts are connected and excited with forces derived from operational conditions. The outcomes of the tool are the dynamic stiffnesses in the selected mount's DoF, for the above mentioned variable parameters.
2. **Mounts' modeling from experimental results:** On the base of the out-

come of tool1, fitting response surfaces are obtained. The latter are based on a parametric model, that allows to describe and modify, punctually, the dynamic behavior of the mount in the different directions and according to the actual working condition.

3. **Mounts' selection and optimization tool for vehicle platform:** The numerical models obtained in 2 are one of the input for the optimization. This uses the mount informations together with the chassis NTFs to predict the SPL at the driver's ear. A DOE analysis is used to explore the possible solutions space, defined by the allowed variability of the different needed components.
4. **Sub-component "in-situ" dynamic identification tool:** The presence of subsystems, produced by third parties requires for a validation tool both for the assessment of the dynamic properties and the acceptability of the product. The tool allows to perform the requested characterization through experimental measurements.

The latest results obtained in this thesis, have highlighted the role of flexible hoses in the propagation of structural noise in vehicles. However, there are no standardized methods for simulation and identification of this phenomena to date. The main problem with these components is the determination of their dynamic properties. If it is, in fact, difficult to characterize rubber mounts experimentally, it is even more difficult to characterize flexible hoses, which are composed of multiple layers of isotropic materials.

At the end of my thesis I will work for BMW Group, and my task will be to develop and validate a methodology to identify and model the dynamic stiffness of those hoses. The result of the ongoing activity on the topic will be published in the work of Ricci et al. [79].

Appendix

For completeness to what was reported in [Experimental Derivation of the Apparent Mass](#), where only specific results were discussed. Comparisons between FRFs of the inertness matrix (experimental and analytical) are reported here, complete.

As above, all FRF comparison plots of the apparent mass matrix (experimental and analytical) are shown here.

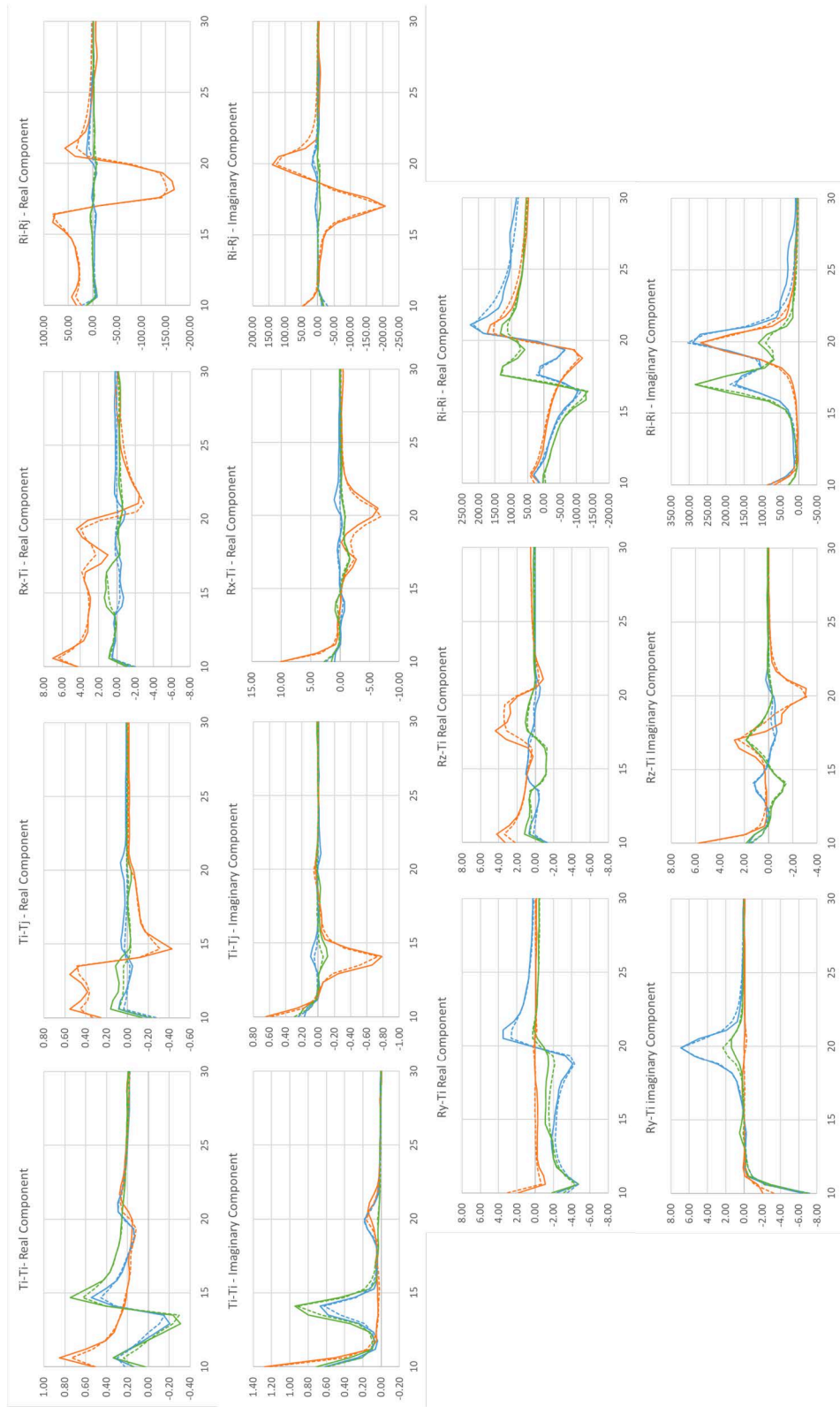


Figure 66: Optimization results on the Inertance Matrix's FRFs - - - - Represent simulated data; — represent measured data.

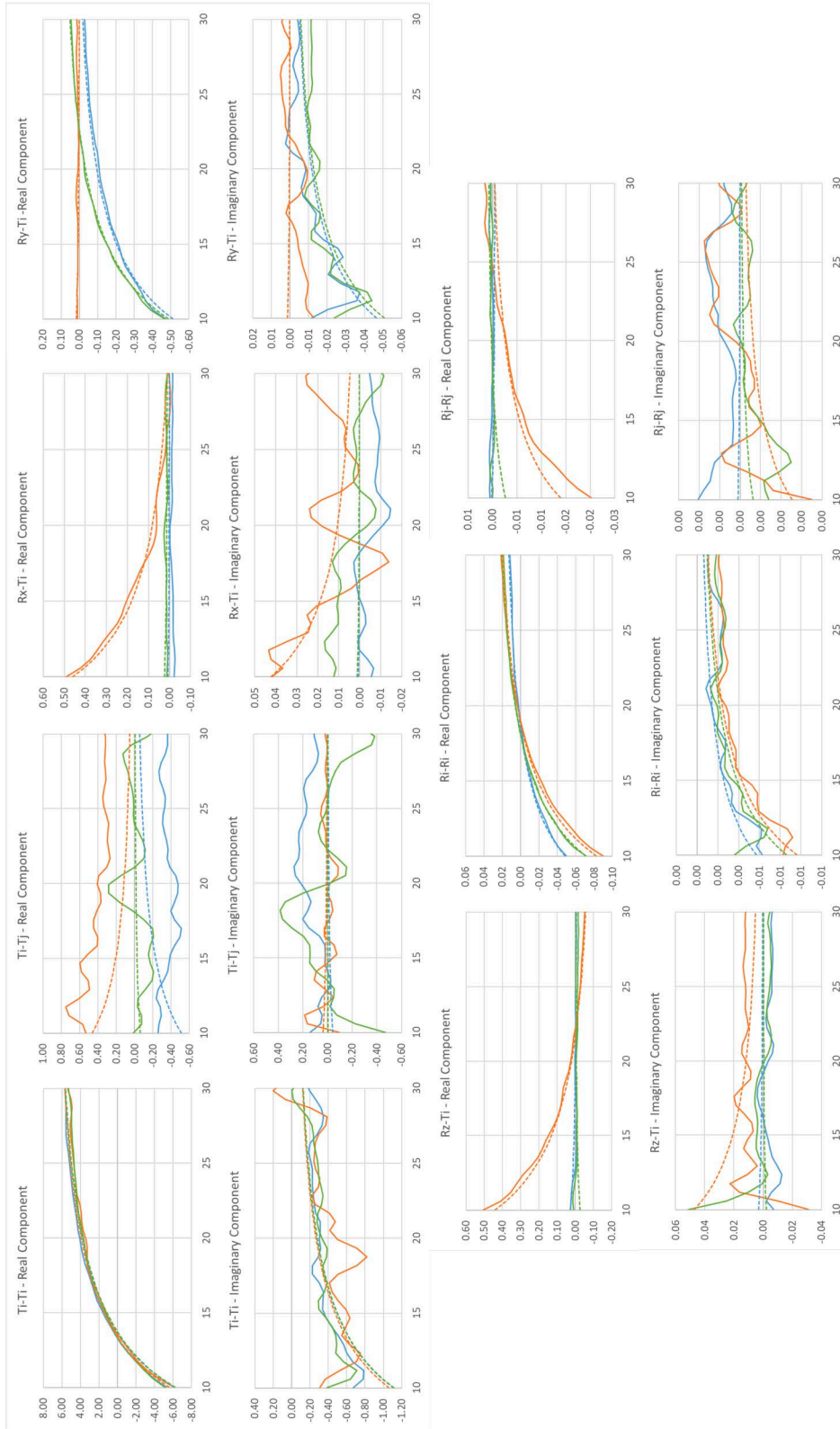


Figure 67: Optimization results on the Apparent Mass Matrix's FRFs - - - - Represent simulated data; — represent measured data

List of Figures

1	Interaction model of noise and vibration refinement in vehicle integration [copyright RMIT University, 2008, Wang, X. [3]]	4
2	V Model vehicle life cycle - typical approach for the vehicle development	5
3	Perception of noise and vibration as function of frequency (figure taken from [9] - description translated into English)	8
4	Systematic correlation between internal forces, chassis sensitivity function and sound pressure level within the vehicle	10
5	Representation of a generic beam with its coordinate system. Point E identifies the elastic center from [43].	16
6	Loads applied in the elastic center E [43]: a - An applied linear force produces a pure displacement. b - an applied moment produces a pure rotation.	18
7	Schematic representation of the structure borne noise paths - Reciprocity measurements	19
8	Generalization of the TPA approach	20
9	TPA scheme for measuring the Blocked forces on a purpose test bench	22
10	Vehicle SPL variability within a group of 5 nominally identical vehicles	25
11	Graphical representation of the procedure followed for the characterization of the powertrain mounts and optimization of the SPL	27
12	Test bench representation. The engine is shown as mounted with the front axle carrier. The accelerometers for the identification of the powertrain displacements are placed using specific holders. These last ones are highlighted in different colors: EnM (Engine Mount) - GeM (Gearbox Mount) - TSM (Torque Strut Mount).	29
13	Load cells mounting scheme - In the picture the naming and the locations of the different load cells utilized is represented. For each sensor an orientation is also defined.	31
14	Geometrical consistency for the accelerometers placed on the three main mounts: —EnM —GeM —TSM (measured values) - - -EnM - - -GeM - - -TSM (geometric consistency)	36
15	Positioning of the virtual points in the powertrain mounts. a - Engine Mount b - Gearbox Mount c - Torque Strut Mount	38
16	VP - acceleration synthesis. Comparison of values measured outside the mount and synthesized at the virtual point. —EnM, —GeM, —TSM: accelerations synthetised in the VP - - -EnM, - - -GeM, - - -TSM: acceleration measured in the mounts proximity	39
17	Measurement procedure for obtaining transfer matrices between VPs and force sensors	40

List of Figures

18	Frequency transmission ratio for individual degrees of freedom measured at the EnM.	41
19	Dynamic TSM stiffness - Magnitude $[\frac{N}{mm}]$	42
20	Dynamic Stiffness magnitude in $[\frac{N}{mm}]$ - Dependence of the individual considered parameters.	42
21	Dynamic TSM stiffness - Phase Angle $[\circ]$	43
22	Dynamic stiffness phase angle in $[\circ]$ - dependence of the individual considered parameters.	43
23	Dynamic Stiffness of the EnM.	45
24	Dynamic Stiffness of the GeM.	45
25	Dynamic Stiffness of the TSM.	46
26	Multiple inflection points in a typical static force - dynamic stiffness diagram. The inflection points are highlighted with red markers. The domain is divided into two halves, identifying a static preload value as the splitting point. In the vicinity of such a point the two generated models are overlapped admitting a 2% superposition.	47
27	Dynamic Stiffness of the EnM	49
28	Dynamic Stiffness of the GeM	49
29	Dynamic Stiffness of the TSM.	50
30	Dynamic Forces of the EnM.	51
31	Dynamic Forces of the GeM.	51
32	Dynamic Forces of the TSM.	52
33	Dynamic Stiffness of the EnM.	53
34	Dynamic Stiffness of the GeM.	53
35	Dynamic Stiffness of the TSM.	54
36	Comparison of the measured and synthesised SPL - A-Weighted —measured SPL ---synthetized SPL	56
37	Comparison of the measured and synthesised SPL - synthesis error —measured SPL ---synthetized SPL	57
38	Comparison of the SPL - A-Weighted —SPL synthetized utilizing the blocked forces transferred in the VPs ----SPL synthetized utilizing the dynamic forces extracted from RS models	58
39	Virtual Design Creation Scheme - Surface mount responses generated are combined to create a new virtual design	59
40	Comparison of the SPL - A-Weighted ---SPL synthetized utilizing the blocked forces from the PMS design used as reference ----SPL synthetized utilizing the dynamic forces extracted from RS models used to generate a virtual design	60
41	Comparison of the SPL obtained using, NTFs measured by the reciprocal method, and that obtained from instrumented hammer impacts measurements. —NTF obtained via reciprocal measurements ----NTF obtained via hammer impact measurements.	61

42	Comparison of the SPL obtained using, NTFs measured by the reciprocal method (—) , and that obtained from instrumented hammer impacts measurements (----). —EnM - Contribution in X; —GeM - Contribution in X; —TSM - Contribution in X; —Wishbone Mounts (Du) - Contribution in X: —Sum of all contribution in Z. .	62
43	Modal Analysis of the complete TMB - 2 Series Touring. The modal analysis is performed using a reciprocal method (Loud Speaker excitation)	63
44	SPL correlation matrix of SPLs for the 3 groups of vehicles.	66
45	SPL correlation matrix for U06 vehicles.	67
46	Optimization process scheme.	69
47	Result of optimization for each vehicle of the group studied in detail. —Baseline SPL value. The same baseline mounting configuration is used for all vehicles ---Optimized SPL. The same optimized mounts are used for all vehicles.	70
48	Results of sensitivity analysis for the five vehicles considered for optimization.	71
49	General representation of a scroll compressor[70]: a - The compression mechanism is formed by two identical scrolls. One is inverted and rotated 180° to intermesh with the opposite scroll b - The compression process is continuous, at any given time the scroll vanes contain pockets of low-, medium-, and high pressure refrigerant gas.	73
50	Representation of the system. The refrigerant compressor is highlighted in red. It is attached to the front chassis side utilizing a prototypal subframe. The mounting strategy is based on a single level of decoupling.	74
51	The compressor is excited with an instrumented hammer at the indicated points and directions. Accelerometers located on the compressor are also visible. At the center of the compressor, highlighted in red, the VP is defined, which coincides, in this case, with the compressor's center of mass.	76
52	Rigid body motion of the compressor under sweep operating conditions synthetized in the compressor VP.	77
53	Inertance Matrix for the electric compressor measured in-situ for the 6DoF of the virtual point-VP. The squares in the figure represent the response of each individual degree of freedom, to a unit excitation in each of them	82
54	Dynamic stiffness and damping gain factors - analitically defined. . .	84
55	Comparison of compressor eigenvectors, obtained analytically and experimentally.	89
56	Condition number of the inertance matrix as function of frequency. .	90

List of Figures

57	Comparison of the simulated (----) and experimentally determined FRFs (—), both in the inertance and apparent mass FRF Matrix Rx-Rx —; Ry-Ry —; Rz-Rz —	91
58	Comparison of the simulated (----) and experimentally determined FRFs (—), both in the inertance and apparent mass FRF Matrix Tx-Tx —; Ty-Ty —; Tz-Tz —	92
59	Comparison of the simulated (----) and experimentally determined FRFs (—), both in the inertance and apparent mass FRF Matrix Tx-Ty —; Tx-Tz —; Ty-Tz —	93
60	Configurations in which compressor characteristics can be identified.	94
61	Evaluation based on experimental data of compressor characteristics. Measurement made without hoses mounted on the compressor.	95
62	Evaluation based on experimental data of compressor characteristics. Measurement made without hoses mounted on the compressor.	96
63	Dynamic stiffness modeling	98
64	Measurement campaign for the acquisition of the noise transfer functions from the compressor holder to the driver's ears.	98
65	Comparison of the synthesized and simulated driver-perceived SPL without considering the flexible hoses influence —Measured SPL —Synthetized SPL	99
66	Comparison of the synthesized and simulated driver-perceived SPL considering the flexible hoses influence —Measured SPL including the flexible hoses' contribution SPL —Synthetized SPL not including the flexible hoses' contribution to SPL	100
67	Optimization results on the Inertance Matrix's FRFs - - - -Represent simulated data; —represent measured data.	
68	Optimization results on the Apparent Mass Matrix's FRFs - - - -Represent simulated data; —represent measured data	

References

- [1] Kistler, “Triaxial force sensors.” [Online]. Available: <https://www.kistler.com/files/document/003-525e.pdf>
 - [2] F. Penne, “Shaping the sound of the next-generation bmw,” in *Proceeding of ISMA 2004*, K. Leuven, Ed. Katholieke Universiteit Leuven, 2004.
 - [3] X. Wang, *Vehicle noise and vibration refinement*. Woodhead Publishing Limited, 2010.
 - [4] D.-H. Lee, W.-S. Hwang, and M.-E. Kim, “Booming noise analysis in a passenger car using a hybrid-integrated approach,” in *SAE 2000 World Congress*, ser. SAE Technical Paper, 2000.
 - [5] M. V. der Seijs, “Experimental dynamic substructuring: Analysis and design strategies for vehicles development,” Ph.D. dissertation, Delft University of Technology, 2016.
 - [6] S. Bennouna, T. Matharan, and O. Cheriaux, “Automotive hvac noise reduction,” *SAE Technical Paper*, 2018.
 - [7] S. T. Lim, K. H. Joo, H. N. Ahn, Y. D. Park, and Y. J. Kang, “Transfer characteristics of vehicle air conditioners’ booming noise,” *Journal of Mechanical Science and Technology*, vol. 28, no. 6, pp. 2025–2032, 2014.
 - [8] M. Festa, F. Stalter, A. Tavornmas, and F. Gauterin, “Human response to vehicle vibrations and acoustics during transient road excitations,” *Vibrations*, pp. 357–368, 2021.
 - [9] K. Hieronimus, “Anforderungen an schwingungs- und akustikberechnungen aus sicht der fahrzeugentwicklung,” *VDI-Berichte*, vol. 816, pp. 705–734, 1990.
 - [10] K. Genuit and J. Poggenburg:, “Untersuchungen zum einfluß der körper-schallübertragungswege auf das kraftfahrzeug-innengeräusch,” ., 1995.
 - [11] G. C. Jay, “Sound/vibration quality engineering part 1 – introduction and the svq engineering process,” *Sound and Vibration*, 2007.
 - [12] G. Cerrato, “Automotive sound quality - powertrain, road and wind noise,” *Sound and Vibration*, vol. 43, no. 4, pp. 16–24, 2009.
 - [13] T. Shin, Y. S. Kim, K. An, and S. K. Lee, “Transfer path analysis of rumbling noise in a passenger car based on in-situ blocked force measurement,” *Applied Acoustics*, vol. 149, pp. 1–14, January 2019.
-

References

- [14] R. Rengarajan, S. Noll, and R. Singh, “Explanation for variability in lower frequency structure-borne noise and vibration: Roles of rear subframe dynamics and right-left spindle phasing,” *Int. J. Veh. Dyn., Stab., and NVH*, vol. 2, no. 1, pp. 27–39, 2018.
 - [15] V. A. J. Britto, S. Karmakar, M. Muthuveeraswamy, and B. Natarajasundaram, “High speed booming noise reduction in passenger car by application of cost optimized nvh solution,” in *SAE Technical Paper*, ser. Technical Papers. SAE Mobilius, 2016.
 - [16] X. Duan, X. Huang, B. Shen, X. Pan, Z. Huang, and L. He, “Application of nvh countermeasures for interior booming noise using elastomeric tuned mass damper,” *SAE Technical Paper*, 2009.
 - [17] X. Yang, G. Muthukrishnan, Y.-J. Seo, and S. Medepalli, “Powertrain mount loads prediction and sensitivity analyses,” *SAE Technical Paper*, 2004.
 - [18] R. Madjlesi, A. Khajepour, F. Ismail, and J. Mihalic, “Advanced noise path analysis, a robust engine mount optimization tool,” *SAE Powertrain and Fluid System Conference Automotive*, 2003.
 - [19] M. Sjöberg, “On dynamic properties of rubber isolators,” Ph.D. dissertation, Kungl Tekniska Högskolan, Teknikringen 8, Stockholm, 2002.
 - [20] J. Harris and A. Stevenson, “On the role of nonlinearity in the dynamic behavior of rubber components,” *Rubber Chemistry and Technology*, vol. 59, no. 5, pp. 740–764, 11 1986.
 - [21] J. A. Harris, “Dynamic testing under nonsinusoidal conditions and the consequences of nonlinearity for service performance,” *Rubber Chemistry and Technology*, vol. 60, no. 5, pp. 870–887, 11 1987.
 - [22] L. Kari, “On the dynamic stiffness of preloaded vibration isolators in the audible frequency range: Modeling and experiments,” *The Journal of the Acoustical Society of America*, vol. 113, no. 4, pp. 1909–1921, 2003.
 - [23] A.-S. Lectez, E. Verron, and B. Huneau, “Evaluating the influence of a multi-axial static preload on the dynamic properties of elastomers,” 09 2015.
 - [24] M. Sjöberg and L. Kari, “Other possible representations are amplitude and phase, or defining amplitude and loss factor.” *Vehicle System Dynamics*, vol. 37, no. 3, pp. 217–236, 2002.
 - [25] A. Alonso, N. Gil-Negrete, and J. G. JG, “Other possible representations are amplitude and phase, or defining amplitude and loss factor.” *Journal of Sound and Vibration*, vol. 332, pp. 3032–3048, 2013.
-

References

- [26] K. Horiuchi and S. Sakaguchi, “Rubber suspension bushing model identified by general design parameters for initial design phase,” *SAE Int. J. Veh. Dyn., Stab., and NVH*, vol. 2, no. 4, pp. 325–335, 2018.
 - [27] J. Bruns and J. Dreyer, “Dynamic analysis of a hydraulic body mount with amplitude and preload dependence,” *SAE International Journal of Vehicle Dynamics, Stability*, vol. 1, no. 2, pp. 480–487, 2017.
 - [28] M. Ueda, S. Ito, and D. Suzuki, “Application study of nonlinear viscoelastic constitutive model for dynamic behavior of suspension arm bushing,” *SAE Int. J. Passeng. Cars - Mech. Syst.*, vol. 9, no. 1, pp. 336–345, 2016.
 - [29] S. Li, X. Yang, B. Minaker, X. S. Lan, and M. Villaire, “Development of a nonlinear, hysteretic and frequency dependent bushing model,” *SAE Technical Paper*, 2015.
 - [30] M. Berg, “A model for rubber springs in the dynamic analysis of rail vehicles,” *Journal of Rail and Rapid Transit*, vol. 211, pp. 95–108, 1997.
 - [31] ———, “A non-linear rubber spring model for rail vehicle dynamics analysis,” *Vehicle System Dynamics*, vol. 30, pp. 197–212, 1998.
 - [32] X. Feng, P. Xu, and Y. Zhang, “Filled rubber isolator’s constitutive model and application to vehicle multi-body system simulation: A literature review,” *SAE Int. J. Veh. Dyn., Stab., and NVH*, vol. 2, no. 2, pp. 101–119, 2018.
 - [33] W.-B. Shangguan, “Engine mounts and powertrain mounting systems: a review,” *Int. J. Vehicle Noise and Vibration*, vol. 49, no. 4, pp. 237–258, 2009.
 - [34] Y. Yu, N. G. Naganathan, and R. V. Dukkipati, “A literature review of automotive vehicle engine mounting systems,” *Mechanism and Machine Theory*, vol. 36, pp. 123–142, 2001.
 - [35] J. Troge, R. Starobinski, M. Hofmann, B. Knofel, and M. Linke, “Acoustical simulation and evaluation of load-dependent hydraulic engine mounts using two-port description,” *Noise Control Engineering Journal*, vol. 62, no. 6, pp. 396–410, November 2014.
 - [36] M. Concelli, M. Li, J. Chen, R. Zhu, C. Duan, S. Wang, and X. Lu, “Dynamic stiffness and damping characteristics of a shaft damping ring: A combined hyperelastic and viscoelastic constitutive model,” *Shock and Vibration*, 2020.
 - [37] P. Wagne, F. Bianciardi, P. Corbeels, and A. Hülsmann, “High frequency source characterization of an e-motore usign component based tpa,” in *Proceedings of ISMA 2020 and USD 2020*, 2020.
-

References

- [38] M. Häussler, T. Müller, E. A. Pasma, J. Freund, O. Westphal, and T. Voehringer, “Component tpa: benefit of including rotational degrees of freedom and over-determination,” in *Proceedings of ISMA 2020 and USD 2020*, 2020.
 - [39] L. Peng, Z. Wang, Y. Su, X. Li, , and J. Zhang, “Robust optimization design of powertrain mounting system for vehicle nvh performance,” *SAE Technical Paper*, vol. 2017-01-0195, 2017.
 - [40] D. J. Kinchen, “Powertrain mounting robust evaluation methodology utilizing minimal hardware resources,” *SAE Technical Paper*, 2017.
 - [41] D. E. Whitney and J. M. Rourke, “Mechanical behavior and design equations for elastomer shear pad remote center compliances,” *Journal of Dynamic Systems, Measurement, and Control*, vol. 108, no. 223, September 1986.
 - [42] S. Joo, Hiroyuki, and F. Miyazaki, “On the mechanics of elastomer shear pads for remote center compliance (rcc),” in *Proceedings of the 1996 IEEE International Conference of Robotics and Automation*. IEEE, 1996.
 - [43] N. Ciblak and H. Lipkin, “Design and analysis of remote center of compliance structures,” *Jorunal of Robotic System*, vol. 20, no. 8, pp. 415–427, 2003.
 - [44] J. Plunt, “Finding and fixing vehicle nvh problems with transfer path analysis,” *Sound and Vibration*, pp. 12–16, 2005.
 - [45] A. C. Stan, H. Yenerer, P. Sendur, and I. Basdogan, “Experimental transfer path analysis for a heavy duty truck,” in *Proceedings of the ASME 2014 12th Biennial Conference on Engineering Systems Design and Analysis ESDA2014*, vol. ESD2014-20517, ASME. ASME, 2014.
 - [46] L. Wei, W. D. feng1 CHEN Shu-ming LI Yuan-bao andLI Shou-kui, and Z. Weijuan, “Transfer path analysis of powertrain vibration on driver’s noise,” in *2011 Seventh International Conference on Natural Computation*. IEEE, 2011, pp. 2353–2357.
 - [47] F. Bianciardi, J. O. Almirón, E. Risaliti, and P. Corbeels, “Road noise assessment using component-based tpa for a tire assembly,” in *SIA2018*, 2018.
 - [48] M. V. van der Seijs, D. de Klerk, and D. J. Rixen, “General framework for transfer path analysis: History, theory and classification of techniques,” *Mechanical Systems and Signal Processing*, vol. 68, pp. 217–244, 2015.
 - [49] F. Zhang, H. Zhou, and E. Wang, “Matrix inversion method for load identification in transfer paths analysis,” *Lecture Notes in Electrical Engineering*, vol. 141, pp. 517–524, 01 2012.
-

References

- [50] D. Lennström, M. Olsson, F. Wullens, and A. Nykänen, “Validation of the blocked force method for various boundary conditions for automotive source characterization,” *Applied Acoustics*, vol. 102, pp. 108–119, 2016.
 - [51] A. Moorhouse, A. Elliott, and T. Evans, “In situ measurement of the blocked force of structure-borne sound sources,” *Journal of Sound and Vibration*, vol. 35, pp. 679–685, April 2009.
 - [52] A. Moorhouse, A. S. Elliot, and Y. Heo, “Intrinsic characterisation of structure-borne sound sources and isolators from in- situ measurements.” *Proceedings of Meetings on Acoustics*, vol. 19, no. 1, 2013.
 - [53] M. Sturm, T. Alber, A. Moorhouse, D. Zabel, and Z. Wang, “The in-situ blocked force method for characterization of complex automotive structure-borne sound sources and its use for virtual acoustic prototyping,” in *Proceedings of ISMA 2016 and USD 2016*, 2016, pp. 3647–3662.
 - [54] T. Gras, O. Aubry, A. Menon, and J. Champain, “Blocked forces characterization of an air-conditioning compressor – application to the norm iso-21955,” in *MADRID - inter.noise 2019 - Noise Control for a better environment*, 2019.
 - [55] D. de Klerk de Klerk and D. J. Rixen, “Component transfer path analysis method with compensation for test bench dynamics,” *Mechanical System and Signal Processing*, vol. 24, pp. 1693–1710, January 2007.
 - [56] A. Cloix, H. Siwiak, P. Bouvet, F. Barillon, and P. Mordillat, “Characterisation of the booming noise variability in a vehicle,” *Proceeding of ISMA 2021-USD2012*, pp. 4513–4524, 2012.
 - [57] R. M. Shaver, K.-J. J. Liu, and M. G. Hardy, “Vehicle-to-vehicle nvh performance variance,” *SAE Technical Paper*, 2009.
 - [58] C. Lionnet and P. Lardeur, “A hierarchical approach to the assessment of the variability of interior noise levels measured in passenger cars,” *Noise Control Engineering Journal*, vol. 55, no. 1, Jan-Feb 2007.
 - [59] Q. Tian, “Modellreduktion der vorderachse zur abbildung der drehungleichförmigkeit des motors zwischen 20 und 100hz mit matlab,” Master’s thesis, Institut für Produktionstechnik, Karlsruher Institut für Technologie (KIT), Kaiserstrasse 12, 76131 Karlsruhe, 2017.
 - [60] M. Häussler, “Modular sound and vibration engineering by substructuring,” Ph.D. dissertation, Technische Universität München, 2021.
 - [61] J. Fragasso, L. Moro, L. M. Lye, and B. W. Quinton, “Characterization of resilient mounts for marine diesel engines: Prediction of t static response via
-

References

- nonlinear analysis and response surface methodology,” *Ocean Engineering*, vol. 171, pp. 14–24, October 2019.
- [62] R. J. Allemang, “The modal assurance criterion – twenty years of use and abuse,” *Journal of Sound and Vibration*, vol. 37, no. 8, pp. 14–21, 2003.
- [63] M. Brandstätter, “Tieffrequente geräusche in einem kraftfahrzeug bei unebenheitsanregung,” Ph.D. dissertation, Technischen Universität Berlin, 2013.
- [64] D. J. Ewins, *Modal Testing: Theory and Practice*, R. S. P. LTD., Ed. John WileySons Inc., 1984.
- [65] B. Peeters and H. V. der Auwaraer, “Polymax: a revolution in operational modal analysis,” *1st International Operational Modal Analysis Conference*, 01 2005.
- [66] M. Elkafafy, B. Peeters, and P. Guillaume, “Optimal modal parameters estimation from operational data using the iterative mlmm method,” *Conference: 7th International Operational Modal Analysis Conference At: Ingolstadt - Germany*, 2017.
- [67] E. D.Kostopoulos, G. C. Spyropoulos, and J. K. Kldellis, “Real-world study for the optimal charging of electric vehicles,” *Energy Reports*, vol. 6, pp. 418–426, November 2020.
- [68] J. Aurich and R. Baumgart, “Comparison and evaluation of different a/c compressor concepts for electric vehicles,” in *International Compressor Engineering Conference*, P. University, Ed., 2018.
- [69] N. Ishii, M. Fuhushima, K. Sano, and K. Sawai, “A study on dynamic behavior of a scroll compressor,” *International Compressor Engineering Conference*, 1986.
- [70] Carrier, “Scroll compressors - high efficiency compression for commercial and industrial applications,” October 2004.
- [71] P. Bin, V. Lemort, A. Legros, Z. Hongsheng, , and G. Haifeng, “Variable thickness scroll compressor performance analysis—part ii: Dynamic modeling and model validation,” *Journal of Process Mechanical Engineering*, vol. 0, no. 0, pp. 1–9, 2016.
- [72] P. Mas, P. Sas, and K. Wyckaert, “Indirect force identification based upon impedance matrix inversion: A study and deterministical accuracy,” *International Seminar On Modal Analysis*, 1994.
-

References

- [73] A. Fregolent and A. Sestieri, "Identification of rigid body inertia properties from experimental data," *Mechanical Systems and Signal Processing*, vol. 10, no. 6, pp. 697–709, 1996.
 - [74] O. Vahid, A. Khajepour, F. Ismail, and C. Urbaniak, "In situ identification of vehicle engine inertia properties," *Int. J. Vehicle Noise and Vibration*, vol. 3, no. 1, 2007.
 - [75] L. S. Lasdon, R. L. Fox, and M. W. Ratner, "Nonlinear optimization using the generalized reduced gradient method," *RAIRO - Operations Research - Recherche Opérationnelle*, vol. 8, no. V3, pp. 73–103, 1974. [Online]. Available: http://www.numdam.org/item/RO_1974__8_3_73_0/
 - [76] S. Sentpali, "Körperschallübertragung gerader und gebogener biegeschlaffer schlauchleitungen im fahrzeugbau," Ph.D. dissertation, Technischen Universität Kaiserslautern, 2008.
 - [77] D. N. Johnston, T. M. Way, and K. M. Cone, "Measured dynamic properties of flexible hoses," *Journal of Vibration and Acoustics*, vol. 132, 2021.
 - [78] J. Hölcke, "Frequency response of hydraulic hoses," Ph.D. dissertation, Royal Institute of Technology, KTH, 100 44 Stockholm, 2002.
 - [79] A. Ricci, F. Albertz, and L. Bregant, "Hoses' transmission forces identification for structural borne noise of automotive components," *12th International Styrian Noise, Vibration Harshness Congress: The European Automotive Noise Conference*, 2022.
-